

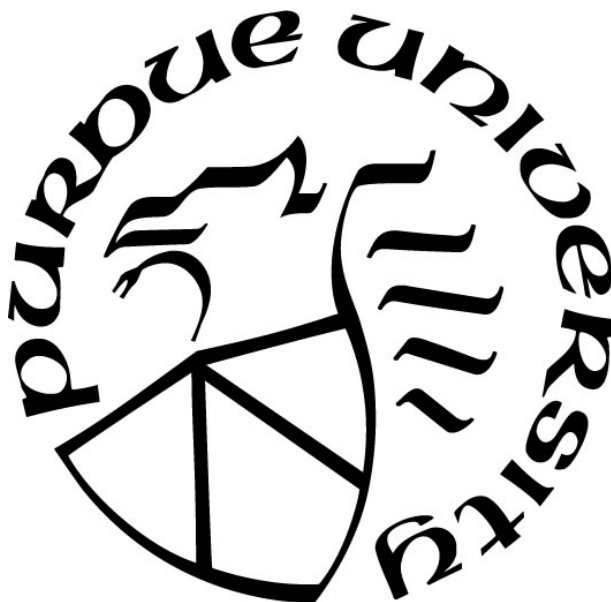
**SECOND HARMONIC GENERATION MICROSCOPY AND RAMAN
MICROSCOPY OF PHARMACEUTICAL MATERIALS**

by
Zhengtian Song

A Dissertation

*Submitted to the Faculty of Purdue University
In Partial Fulfillment of the Requirements for the degree of*

Doctor of Philosophy



Department of Chemistry
West Lafayette, Indiana
August 2019

THE PURDUE UNIVERSITY GRADUATE SCHOOL
STATEMENT OF COMMITTEE APPROVAL

Dr. Garth Simpson, Chair

Department of Chemistry

Dr. Mary Wirth

Department of Chemistry

Dr. Chittaranjan Das

Department of Chemistry

Dr. Peter Kissinger

Department of Chemistry

Approved by:

Dr. Christine Hrycyna

Head of the Graduate Program

To my families and friends

ACKNOWLEDGMENTS

First of all, I would like to express my gratitude to my PhD advisor, Prof. Garth Simpson. I was so lucky that I joined Simpson lab and. Your enthusiasm to scientific research and teaching 621 is very impressive. Your own experience, personality and optimistic inspiring me in many dimensions. I learned a lot from you, not only knowledge of science, but also dedication to my work and family. Thank you for helping me improve my research, collaboration, writing and presenting skills. I really appreciate all of your suggestions of my research, your guide for my career path, and all of your help during my PhD study.

I would also like to acknowledge my collaborators in different projects. I would like to acknowledge Andy and Gerry from AbbVie, who provided me an opportunity for internship and help me to get a better understanding of work in pharmaceutical industry. I also appreciate help from Dilshan, Dong, and Prof. Charles Bouman in Department of ECE. Thank you for bringing the machine learning idea to us. I really enjoyed interdisciplinary research with you.

I would like to thank all of my colleagues in Simpson lab: Emma, Justin, Shane, Azhad, Ximeng, Paul, Nikki, Shijie, Fengyuan, Janny, Sreya, Changqin, Casey, Scott, Hilary, Cody, James, Chen, Alex, Andreas, Youlin, Nita, Minghe, Ziyi, and Jiayue. It is a great experience to work with all of you and share our research ideas and daily lives. I would like to give a special thank you to Shijie and Fengyuan, who recommended me to join Simpson lab and help me a lot during my PhD study; and to Shijie, Azhad, Sreya, Scott, and Hilary for their help and company on our projects. I really enjoyed the working environment in Simpson lab and learned a lot from all of you. Just as Ximeng wrote on the white board, Simpson lab, best lab!

I would like to acknowledge some of my friends. Nan, my roommate for eight years, thank you for helping me to make the decision to come to Purdue and all your help in class and daily life. Yiyang, my best friend and best neighbor in Purdue, thank you for your company in last four years and your encouragement and guidance for job hunting. My old friends, Tao, Zheng, Tian, and Shu, thank you for encouraging me to study in chemistry and become a PhD. And I would like to give a thank you to Shijie, Fengyuan, Changqin, Chen, Aaron and Yun, as co-founders of CASHGA and Simpson-Wirth lunch group. I would also like to give a special thank you to my friends, Wuwei and Xiao, as co-founders of LRSGGG club for werewolf games. The memories with you in Purdue are enjoyable and fantastic.

I would also like to express my love and gratitude to my boyfriend, Xinye Zhang. You are not only an outstanding scientist/engineer for Purdue university, but also a wonderful partner for me. Thank you for always being with me when I am stressed and worried about my research and job hunting. Thank you for encouraging me to be confident and diligent when I complained about troubles in my life. Thank you for spending every day with me on our amazing experiences and unexpectable adventures.

Last but not least, I would like to thank my families. Mom and Dad, thank you for bringing me to the world. Thank you for always trusting me and supporting me for all of my decisions. I know both of you are always on my side, although there is Pacific Ocean between us. Grandpa and grandma, thank you for your understanding and encouragement. I was so surprised that you learned geography of US and watched weather forecast every day for me. Zhengxi, my excellent brother, although it was a pity that we did not grow up together, your support means a lot to me. Thank you for accompanying me and guiding me how to become an adult and a mature scientist with your kindness and intelligence.

TABLE OF CONTENTS

LIST OF TABLES	9
LIST OF FIGURES	10
LIST OF ABBREVIATIONS.....	12
ABSTRACT.....	14
CHAPTER 1. INTRODUCTION	16
1.1 Background and Motivation: Pharmaceutical Materials Analysis	16
1.1.1 Crystallinity in Amorphous Solid Dispersions.....	16
1.1.2 Polymorph Characterization of Active Pharmaceutical Ingredients	17
1.1.3 Conventional Pharmaceutical Characterization Techniques.....	17
1.2 Second Harmonic Generation Microscopy	18
1.3 Confocal Raman Microscopy	19
1.4 Dissertation Overview	20
1.5 References	22
CHAPTER 2. KINETIC MODELING OF ACCELERATED STABILITY TESTING BY SECOND HARMONIC GENERATION MICROSCOPY	28
2.1 Introduction	28
2.2 Methods	30
2.3 Theory.....	32
2.4 Results and Discussions	34
2.5 Conclusion.....	40
2.6 References	40
CHAPTER 3. SECOND HARMONIC GENERATION MICROSCOPY GUIDED RAMAN SPECTROSCOPY FOR PHARMACEUTICAL MATERIALS ANALYSIS.....	51
3.1 Introduction	51
3.2 Methods	53
3.2.1 Sample Preparation	53
3.2.2 Bright Field Image and SHG Image Acquisition.....	54
3.2.3 SHG Guide Raman Measurements	54
3.2.4 X-ray Diffraction Measurements	56

3.2.5	Image Segmentation and Registration Algorithm.....	56
3.3	Results and Discussions	57
3.3.1	SHG Microscopy for Polymorphic Discrimination	57
3.3.2	Raman Spectroscopy for Polymorphic Determination.....	58
3.3.3	X-ray diffraction for Polymorphic Determination	58
3.3.4	Discussions.....	59
3.4	Conclusion.....	62
3.5	References	62
CHAPTER 4. ACCELERATING CONFOCAL RAMAN MICROSCOPY BY DYNAMIC SPARSE SAMPLING		70
4.1	Introduction	70
4.2	Theory.....	73
4.2.1	Dynamic Sparse Sampling Algorithm.....	73
4.2.2	Stopping Condition of SLADS	74
4.2.3	Classification of Raman Spectra	75
4.3	Experimental Methods.....	76
4.3.1	Sample Preparation	76
4.3.2	Raman Spectrum Acquisition.....	76
4.3.3	Ground Truth Raman Image Acquisition.....	77
4.3.4	Classification of Raman Spectra	77
4.3.5	Stopping Condition of SLADS	79
4.3.6	Experimental Implementation of SLADS.....	79
4.4	Results and Discussions	79
4.4.1	Simulation Results for SLADS	79
4.4.2	Comparison with Random Sampling	80
4.4.3	Experimental Implementation of SLADS for Confocal Raman Imaging.....	81
4.4.4	Performance Analysis and Potential Application of SLADS.....	81
4.5	Conclusion.....	84
4.6	References	84
CHAPTER 5. IN SITU ACCELERATED STABILITY TESTING.....		94
5.1	Introduction	94

5.2	Experimental Methods.....	96
5.3	Results and Discussions	97
5.4	Conclusion	101
5.5	References	102
CHAPTER 6. CRYSTALLIZATION ON SURFACE VERSUS IN BURIED WITHIN AMORPHOUS SOLID DISPERSIONS		112
6.1	Introduction	112
6.2	Experimental Methods.....	113
6.2.1	Sample Preparation	113
6.2.2	Accelerated Stability Testing Experiments	114
6.3	Results and Discussions	115
6.4	Summary.....	117
6.5	Future Work.....	117
6.6	Reference	118
VITA.....		122
PUBLICATION.....		123

LIST OF TABLES

Table 2-1 Parameters in JMAK model	50
--	----

LIST OF FIGURES

Figure 1-1 Four classes of APIs based on solubility and permeability	26
Figure 1-2 Representation of second harmonic generation.....	27
Figure 2-1 SHG and bright field images for accelerated stability testing	44
Figure 2-2 Volume fraction of crystallinity in accelerated stability testing.	45
Figure 2-3 Crystal growth rate analysis	46
Figure 2-4 Nucleation kinetics analysis	47
Figure 2-5 Comparison of SHG and PLM images	48
Figure 2-6 Ritonavir crystal form characterization	49
Figure 3-1 Schematic diagram of the prototype instrument of SHG microscopy-guided Raman spectroscopy	65
Figure 3-2 Segmentation algorithm to perform classification of individual particles.	66
Figure 3-3 Integrated SHG intensity of clopidogrel bisulfate Form I and Form II.....	67
Figure 3-4 Polymorph determination of clopidogrel bisulfate by SHG-guided Raman analysis on a per-particle basis.....	68
Figure 3-5 Polymorph determination of clopidogrel bisulfate by SHG-guided synchrotron XRD measurement.....	69
Figure 4-1 Schematic of the random access confocal Raman microscope with the dynamic sampling Raman imaging workflow described in the flowchart.	87
Figure 4-2 Preprocessing of Raman spectrum to improve SNR	88
Figure 4-3 Classification of Raman spectra into three classes.....	89
Figure 4-4 Training images for sampling Raman imaging stopping conditions.....	90
Figure 4-5 Simulated dynamic sampling and random sampling image reconstruction with a ground truth image.....	91
Figure 4-6 Experimental results of confocal Raman imaging with implementation of SLADS. ..	93
Figure 5-1 CEiST design and temperature validation	105
Figure 5-2 Validation of CEiST by comparison with standard chamber	106
Figure 5-3 Time-dependent SHG images of 15% ritonavir ASDs stressed in CEiST.....	107
Figure 5-4 Temperature and humidity cycling effect on crystallization	108

Figure 5-5 Individual crystal growth distribution in ASDs.....	109
Figure 5-6 Nucleation rates for ASDs from individual FOVs	110
Figure 5-7 Comparison of signal to noise ratio of nucleation rate.....	111
Figure 6-1 Sample preparation device.....	120
Figure 6-2 Time-dependent SHG images of seeded crystals in bulk and on surface of ASD films	121

LIST OF ABBREVIATIONS

API	active pharmaceutical ingredient
ASD	amorphous solid dispersion
BCS	biopharmaceutics classification system
BF	bright field
CARS	coherent anti-Stokes Raman scattering
CEiST	controlled environment for <i>in situ</i> stability testing
CCD	charge coupled device
CSD	Cambridge Structural Database
DAC	digital to analog converter
DL	drug loading
DSC	differential scanning calorimetry
FDA	Food and Drug Administration
FOV	field of view
HIV	human immunodeficiency virus
HME	hot melted extrusion
IR	infrared
LCTF	liquid crystal tunable filter
LDA	linear discriminant analysis
LOD	limit of detection
NA	numerical aperture
NCC	normalized cross correlation
NDA	new drug application
NLO	nonlinear optics
NOSE	nonlinear optical Stokes ellipsometric
PAT	process analytical technology
PD	photodiode
PLM	polarized light microscopy
PMT	photomultiplier
ppm	parts per million

PXRD	powder X-ray diffraction
QbD	quality by design
RH	relative humidity
RSD	relative standard deviation
SD	synchronized digitization
SDD	spray dried dispersion
SEM	scanning electron microscopy
SHG	second harmonic generation
SLAS	supervised learning approach to dynamic sampling
ssNMR	solid state nuclear magnetic resonance
SNR	signal to noise ratio
SRS	stimulated Raman scattering
SVM	support vector machine
TPE-UVF	two-photon excited ultraviolet fluorescence

ABSTRACT

Author: Song, Zhengtian. PhD

Institution: Purdue University

Degree Received: August 2019

Title: Second Harmonic Generation Microscopy and Raman Microscopy of Pharmaceutical Materials

Committee Chair: Garth Simpson

Second harmonic generation (SHG) microscopy and Raman microscopy were used for qualitative and quantitative analysis of pharmaceutical materials. Prototype instruments and algorithms for sampling strategies and data analyses were developed to achieve pharmaceutical materials analysis with low limits of detection and short measurement times.

Manufacturing an amorphous solid dispersion (ASD), in which an amorphous active pharmaceutical ingredient (API) within polymer matrix, is an effective approach to improve the solubility and bioavailability of a drug. However, since ASDs are generally metastable materials, they can often transform to produce crystalline API with higher thermodynamic stability. Analytical methods with low limits of detection for crystalline APIs were used to assess the stability of ASDs. With high selectivity to noncentrosymmetric crystals, SHG microscopy was demonstrated as an analytical tool, which exhibited a limit of detection of 10 ppm for ritonavir Form II crystals. SHG microscopy was employed for accelerated stability testing of ASDs, which provided a four-decade dynamic range of crystallinity for kinetic modeling. An established model was validated by investigating nucleation and crystal growth based on SHG images. To achieve *in situ* accelerated stability testing, controlled environment for *in situ* stability testing (CEiST) was designed and built to provide elevated temperature and humidity, which is compatible with a commercial SHG microscope based on our research prototype. The combination of CEiST and SHG microscopy enabled assessment of individual crystal growth rates by single-particle tracking and nucleation rates for individual fields of view with low Poisson noise. In addition, SHG microscopy coupled with CEiST enabled the study of heterogeneity of crystallization kinetics within pharmaceutical materials.

Polymorphism of APIs plays an important role in drug formulation development. Different polymorphs of identical APIs may exhibit different physiochemical properties, e.g., solubility, stability, and bioavailability, due to their crystal structures. Moreover, polymorph transitions may

take place during the manufacturing process and storage. Therefore, analytical methods with high speed for polymorph characterization, which can provide real-time feedback for the polymorphic transition, have broad applications in pharmaceutical materials characterization. Raman spectroscopy is able to determine the API polymorphism, but is hampered by the long measurement times. In this study, two analytical methods with high speed were developed to characterize API polymorphs. One is SHG microscopy-guided Raman spectroscopy, which achieved the speed of 10 ms/particle for clopidogrel bisulfate. Initial classification of two different polymorphs was based on SHG images, followed acquisition of Raman spectroscopy at the selected positions to determine the API crystal form. Another approach is implementing of dynamic sampling into confocal Raman microscopy to accelerate Raman image acquisition for 6-folds. Instead of raster scanning, dynamic sampling algorithm enabled acquiring Raman spectra at the most informative locations. The reconstructed Raman image of pharmaceutical materials has <0.5% loss of image quality with 15.8% sampling rate.

CHAPTER 1. INTRODUCTION

1.1 Background and Motivation: Pharmaceutical Materials Analysis

1.1.1 Crystallinity in Amorphous Solid Dispersions

An active pharmaceutical ingredient (API) with high aqueous solubility can be dissolved in patients' blood and/or gut. In addition, APIs are required to be permeable enough to pass through cell membranes.¹ Therefore, solubility and permeability are two of main properties that affect the bioavailability of APIs.² In the biopharmaceutics classification system (BCS), APIs and API candidates are classified into four categories based on their solubility and permeability, shown in Figure 1-1. Unfortunately, the majority of emerging APIs belong to either Class II or IV, which show low aqueous solubility. Previous studies estimated that nearly 40% of potential new API candidates are abandoned due to their low aqueous solubility.³

Different from crystalline APIs in class II or IV, amorphous APIs can effectively improve the bioavailability of poorly water-soluble drug. Scientists developed a strategy of formulation to render the API as amorphous state within a polymer matrix to form amorphous solid dispersions (ASDs).⁴ ASDs have been demonstrated as an effective approach to increase the aqueous dissolution kinetics.⁵ However, amorphous APIs are in a meta-stable state, which has relatively high potential energy.⁶ Although in ASDs, the polymer matrix reduces the potential for the conversion from amorphous state to the thermodynamically more stable crystalline form, such amorphous formulations are still in danger of crystallizing over time.⁷ Therefore, it is worthwhile to investigate the stability and ultimately therapeutic effect of ASDs by quantifying the crystalline API in ASDs. Additionally, during the study of ASDs manufacturing condition (e.g., temperature for hot melt extrusion⁸, solvent for spray drying⁹), the ASD products may include residual crystalline API.¹⁰ The residual crystallinity of API may significantly reduce the bioavailability and affect the dissolution kinetics of the formulation.¹¹ Thus, analytical methods, which are capable of sensitively and selectively detecting low levels of API crystallinity, are required in quantitative analysis of crystalline API in ASDs and characterizing the stability and efficacy of the formulation.

1.1.2 Polymorph Characterization of Active Pharmaceutical Ingredients

Polymorphism of an API plays a significant role in pharmaceutical formulation. Different polymorphs of an API have the same chemical component but the crystal structures are different due to the probability of different molecular orientations and crystal lattice.^{12, 13} Therefore, polymorphism can significantly affect the physical and chemical properties of APIs, including thermodynamic stability, aqueous solubility, and bioavailability, which may change the ultimate efficacy of the drug.¹⁴ A recent study demonstrated that more than 80% of APIs exhibit polymorphism.¹⁵ Therefore, it is necessary to characterize API polymorphs during the formulation development.

Based on Ostwald's rule of stages, in most cases, thermodynamically less stable polymorphs have a tendency to convert into the most stable form.¹⁶ Although a less stable polymorph may crystallize first due to the combination of thermodynamics and kinetics, the most stable polymorph will still be the dominant product under thermodynamic conditions with stable temperature and prolonged time for crystallization. Moreover, the metastable polymorphs of APIs are able to transform into the more stable crystal form via solid state phase transitions, which is problematic for the pharmaceutical formulation development. A well-known case for polymorphism trouble in pharmaceutical industry is ritonavir.¹⁷ Norvir®, which was a marketed final dosage form of ritonavir packaged as capsule, consisted of ritonavir Form I with high bioavailability and had been approved by the Food and Drug Administration (FDA). However, in 1998, the ritonavir drug had to be recalled, due to the discovery of ritonavir Form II with lower bioavailability and slower dissolution kinetics.¹⁷ During the storage time, the meta-stable ritonavir Form I transform into Form II spontaneously. The large-scale withdrawal of Norvir cost manufacturer's almost 250 million dollars. As a result of this case, the FDA now requires a thorough characterization of API polymorphism when pharmaceutical companies file a new drug application.¹⁸ Therefore, sensitive and selective analytical techniques are useful in not only characterization of API polymorphs, but also in real-time monitoring of the polymorph transitions during manufacturing process or storage.

1.1.3 Conventional Pharmaceutical Characterization Techniques

Several conventional analytical techniques are employed to quantify the crystallinity of APIs from the early stage of drug formulation development to the shelf life of a final product¹⁹,

including powder X-ray diffraction (PXRD), differential scanning calorimetry (DSC), solid state nuclear magnetic resonance spectroscopy (ssNMR), and Raman spectroscopy²⁰. Currently, PXRD is the gold standard for solid-state analysis of pharmaceutical materials. However, in most cases, detection of crystallinity lower than 1% is challenging for PXRD.²¹ DSC is capable of automated data acquisition and providing thermal process information of solid-solid transitions, but its limit of detection can only achieve 3% crystalline API in ASDs.²² Previous studies have shown that ssNMR were used to quantitatively analyze all components in ASDs with limits of detection at 0.4% for carbon.²³ All of the above methods suffered from the high limits of detection, which limit their applications in the early stages of crystallization. Furthermore, the existence of trace crystallinity within an initially amorphous formulation can significantly affect drug dissolution kinetics.²⁴ Additionally, several microscopy techniques, such as, polarized light microscopy (PLM), and scanning electron microscopy (SEM) can be utilized to detect crystallization in pharmaceutical formulations. However, PLM can only deal with optical transparent sample,²⁵ and SEM requires complicated sample preparation and provides no chemical information.²⁶ Therefore, quantitative analytical methods with low limits of detection have broad applications in pharmaceutical materials analysis.

Similar analytical tools can also be used for polymorph characterization of APIs. PXRD is widely used for polymorph determination as well.¹⁷ However, it suffers from its limit of detection and analysis speed, which cannot be compatible with high throughput analysis and monitor the polymorph transition in real-time. Some techniques for polymorph characterization are listed in Chapter 3.1. It is necessary to develop analytical tools with high speed that are capable of real-time characterizing of API polymorphs.

1.2 Second Harmonic Generation Microscopy

Peter A. Franken first demonstrated the phenomenon of nonlinear optics (NLO) in 1961²⁷ after the invention of the ruby laser²⁸. Second harmonic generation (SHG) is a second order nonlinear optical process with the presence of an intense optical-electric field (e.g., at the focus of laser). A schematic of second harmonic generation is shown in Figure 1-2. The induced molecular polarization anharmonicity arises from the intense optical-electric field.²⁹ The distorted sinusoidal oscillation (purple line) observed in the time domain is a combination of the sinusoidal wave at the fundamental frequency (red line) with the second harmonic (green line). Therefore, the net

induced polarization for isotropic or centrosymmetric samples is zero at second harmonic frequency. As a result, the bulk selection rule for SHG requires noncentrosymmetric crystals.³⁰ Unordered materials, such as liquid, gas, and amorphous solid generate no coherent SHG signal.

SHG microscopy has been demonstrated as a powerful tool for detection and quantification of noncentrosymmetric crystals.³¹ Recent studies have shown the applications of SHG microscopy for high-throughput protein crystallization screening³², detection of organic nanocrystals³³, and crystallization kinetics studies³³. Especially, SHG microscopy has broad applications in pharmaceutical materials analysis, including low-crystallinity API crystal detection (in ppm regime)³⁴, quantification of APIs and excipients in powder matrix³⁵, and rapid discrimination of API polymorphs³⁶. However, SHG microscopy alone cannot provide chemical information, which limits its applications in chemical identification of pharmaceutical materials.³⁷ Thus, integration of SHG microscopy with other orthogonal analytical techniques that can provide rich chemical information has the potential to enable rapid characterization of pharmaceutical materials.

1.3 Confocal Raman Microscopy

The Raman effect was first observed in 1928 by Indian scientist Sir C. V. Raman.³⁸ The Raman effect correlated with the polarizability of electrons in a molecule. After the molecule is excited to a virtual energy state, the scattered photon shifts to a different frequency with a Stokes/anti-Stokes shift. Raman spectroscopy is known as a highly specific and chemical information rich technique, which is widely used to acquire qualitative and quantitative chemical information.³⁹ In order to collect both spatial and spectral information, confocal Raman microscope was developed.

Confocal Raman microscopy has proven to be a powerful molecular imaging technique for the analysis of diverse pharmaceutical products.⁴⁰ Raman offers the advantage of non-destructive analysis with minimal or no sample pretreatment or preparation. Additionally, it is an analytical method that can be widely adopted for Process Analytical Technology (PAT) as the guideline proposed by FDA since 2004.⁴¹ In a conventional point-scanning confocal Raman microscope, a laser point-focus under a microscope is raster scanned across the specimen in two dimensions and a full spectrum is recorded at each x, y position. This point-to-point mapping affords the ultimate sensitivity, spatial resolution, image quality, and large spectral range capability. Due to the weak nature of Raman scattering of molecules, typical image acquisition times can be on the order of 1

s per pixel or longer and thus total imaging times can be significant.⁴² This drawback limits the use of confocal Raman microscopy for pharmaceutical materials analysis. Therefore, methods to effectively accelerate point-scanning confocal Raman imaging are beneficial for chemical identification.

1.4 Dissertation Overview

This dissertation focuses on using SHG microscopy and Raman microscopy for qualitative and quantitative analysis of pharmaceutical materials. In order to obtain analytical methods with low limit of detection and high speed, this dissertation includes not only the development of prototype device and instrument, but also the implementation of an advanced algorithm for sampling strategy and data analysis. For quantitative analysis, the main target is to detect the crystalline API in ASDs during accelerated stability testing with low limit of detection by using SHG microscopy. A kinetic model was built to illustrate the time-dependent crystalline fraction, nucleation, and crystal growth process of APIs in ASDs. Moreover, the *in situ* accelerated stability testing enables the investigation of individual single-crystal, which leads to the study of heterogeneity of crystallization kinetics within ASDs. For qualitative analysis, this dissertation focuses on API polymorph identification with high speed. Both of SHG-guided Raman spectroscopy and confocal Raman microscopy coupled with a dynamic sampling algorithm can significantly reduce the measurement time.

Chapter 2 describes kinetic modeling of accelerated stability testing enabled by SHG microscopy coupled with particle counting algorithms. This chapter focuses on the study of accelerated stability testing on ritonavir, a human immunodeficiency virus (HIV) protease inhibitor. Under the condition for accelerated stability testing at 50°C/75%RH and 40°C/75%RH, ritonavir crystallization kinetics from ASDs were monitored by SHG microscopy. This analytical method yielded limits of detection for ritonavir crystals as low as 10 ppm (v/v), which is two orders of magnitude lower than other methods currently available for crystallinity detection in ASDs. Extensive stability testing is typically performed for ASD characterization, the time-frame for which is often dictated by the earliest detectable onset of crystal formation. The four-decade dynamic range enabled quantitative modeling with the JMAK kinetic model.

Chapter 3 introduces a prototype SHG-guided Raman instrument, which integrated SHG microscopy for high speed screening and Raman spectroscopy for obtaining chemical information.

This chapter mainly focuses on polymorph identification of clopidogrel bisulfate Form I and Form II. Image registry algorithms enable automated identification of particles by bright field images, followed by classification using SHG images. SHG microscopy enabled polymorph discrimination with the speed of ~10 ms per particle. Complementary identification by Raman and synchrotron XRD are in excellent agreement with the classifications made by SHG. Coupling these capabilities with at-line monitoring may enable real-time feedback of polymorph characterization during the pharmaceuticals manufacturing process.

Chapter 4 introduces the implementation of an advanced sparse sampling algorithm into confocal Raman microscopy. The total number of data points required for image generation in Raman microscopy was greatly reduced using the supervised learning approach to dynamic sampling (SLADS), in which the preceding set of measurements informed the next most information-rich sampling location. Using this approach, chemical images of pharmaceutical materials were obtained with >99% accuracy from 15.8% sampling, representing a ~6-fold reduction in measurement time relative to full field of view rastering with comparable image quality. SLADS has the distinct advantage of being directly compatible with standard confocal Raman instrumentation. Furthermore, SLADS is not limited to Raman imaging, potentially providing time-savings in image reconstruction whenever the single-pixel measurement time is the limiting factor in image generation.

Chapter 5 illustrates how to achieve *in situ* accelerated stability testing of ASDs by a compatible temperature and humidity control device with SHG microscopy. Single-particle tracking of crystal growth performed *in situ* enables substantial improvements in the signal to noise ratio (SNR) for recovered crystal nucleation and growth rates by SHG microscopy. Moreover, reduction in the Poisson noise associated with the finite number of particles present in a given field of view through continuous monitoring during stability testing was achieved. These capabilities provide significant improvements in the signal to noise for nucleation and crystal growth measurements, with automated image acquisition and less requirements of samples.

Chapter 6 investigates growth rates for ritonavir crystallites seeded at the surface and embedded in the bulk of supersaturated amorphous solid dispersions by *in situ* SHG microscopy. In this study, “sandwich” materials were prepared, in which sparsely prepared seeds of ritonavir single crystals were pressed between two identical ASD slabs to assess bulk crystallization rates. These sandwich materials were compared and contrasted with analogously prepared “open-faced”

samples without the capping film to assess surface crystallization rates. Single particle analysis by SHG microscopy time-series during *in situ* crystallization were employed to calculate average growth rates.

1.5 References

1. Byrn, S. R.; Pfeiffer, R. R.; Stephenson, G.; Grant, D. J. W.; Gleason, W. B., Solid-State Pharmaceutical Chemistry. *Chem Mater* **1994**, *6* (8), 1148-1158.
2. Pouton, C. W., Formulation of poorly water-soluble drugs for oral administration: Physicochemical and physiological issues and the lipid formulation classification system. *Eur J Pharm Sci* **2006**, *29* (3-4), 278-287.
3. Ghadi, R.; Dand, N., BCS class IV drugs: Highly notorious candidates for formulation development. *J Control Release* **2017**, *248*, 71-95.
4. Vasconcelos, T.; Sarmiento, B.; Costa, P., Solid dispersions as strategy to improve oral bioavailability of poor water soluble drugs. *Drug Discov Today* **2007**, *12* (23-24), 1068-1075.
5. Newman, A.; Knipp, G.; Zografi, G., Assessing the performance of amorphous solid dispersions. *J Pharm Sci-US* **2012**, *101* (4), 1355-1377.
6. Yang, J.; Grey, K.; Doney, J., An improved kinetics approach to describe the physical stability of amorphous solid dispersions. *Int J Pharmaceut* **2010**, *384* (1-2), 24-31.
7. Bhugra, C.; Pikal, M. J., Role of thermodynamic, molecular, and kinetic factors in crystallization from the amorphous state. *J Pharm Sci-US* **2008**, *97* (4), 1329-1349.
8. Lalkshman, J. P.; Cao, Y.; Kowalski, J.; Serajuddin, A. T. M., Application of Melt Extrusion in the Development of a Physically and Chemically Stable High-Energy Amorphous Solid Dispersion of a Poorly Water-Soluble Drug. *Mol Pharmaceut* **2008**, *5* (6), 994-1002.
9. Singh, A.; Van den Mooter, G., Spray drying formulation of amorphous solid dispersions. *Adv Drug Deliver Rev* **2016**, *100*, 27-50.
10. Chen, J.; Sarma, B.; Evans, J. M. B.; Myerson, A. S., Pharmaceutical Crystallization. *Cryst Growth Des* **2011**, *11* (4), 887-895.
11. Abu Bakar, M. R.; Nagy, Z. K.; Saleemi, A. N.; Rielly, C. D., The Impact of Direct Nucleation Control on Crystal Size Distribution in Pharmaceutical Crystallization Processes. *Cryst Growth Des* **2009**, *9* (3), 1378-1384.
12. Vippagunta, S. R.; Brittain, H. G.; Grant, D. J. W., Crystalline solids. *Adv Drug Deliver Rev* **2001**, *48* (1), 3-26.

13. Aaltonen, J.; Alleso, M.; Mirza, S.; Koradia, V.; Gordon, K. C.; Rantanen, J., Solid form screening - A review. *Eur J Pharm Biopharm* **2009**, *71* (1), 23-37.
14. Snider, D. A.; Addicks, W.; Owens, W., Polymorphism in generic drug product development. *Adv Drug Deliver Rev* **2004**, *56* (3), 391-395.
15. Chieng, N.; Rades, T.; Aaltonen, J., An overview of recent studies on the analysis of pharmaceutical polymorphs. *J Pharmaceut Biomed* **2011**, *55* (4), 618-644.
16. Hall, V. J.; Simpson, G. J., Direct Observation of Transient Ostwald Crystallization Ordering from Racemic Serine Solutions. *J Am Chem Soc* **2010**, *132* (39), 13598-13599.
17. Bauer, J.; Spanton, S.; Henry, R.; Quick, J.; Dziki, W.; Porter, W.; Morris, J., Ritonavir: An extraordinary example of conformational polymorphism. *Pharmaceut Res* **2001**, *18* (6), 859-866.
18. Ciociola, A. A.; Cohen, L. B.; Kulkarni, P.; Gastroenterology, A. C., How Drugs are Developed and Approved by the FDA: Current Process and Future Directions. *Am J Gastroenterol* **2014**, *109* (5), 620-623.
19. Shah, B.; Kakumanu, V. K.; Bansal, A. K., Analytical techniques for quantification of amorphous/crystalline phases in pharmaceutical solids. *J Pharm Sci-Us* **2006**, *95* (8), 1641-1665.
20. Strachan, C. J.; Taday, P. F.; Newnham, D. A.; Gordon, K. C.; Zeitler, J. A.; Pepper, M.; Rades, T., Using terahertz pulsed spectroscopy to quantify pharmaceutical polymorphism and crystallinity. *J Pharm Sci-Us* **2005**, *94* (4), 837-846.
21. Ghebremeskel, A. N.; Vemavarapu, C.; Lodaya, M., Use of surfactants as plasticizers in preparing solid dispersions of poorly soluble API: Stability testing of selected solid dispersions. *Pharmaceut Res* **2006**, *23* (8), 1928-1936.
22. Yoshihashi, Y.; Iijima, H.; Yonemochi, E.; Terada, K., Estimation of physical stability of amorphous solid dispersion using differential scanning calorimetry. *J Therm Anal Calorim* **2006**, *85* (3), 689-692.
23. Berendt, R. T.; Sperger, D. M.; Isbester, P. K.; Munson, E. J., Solid-state NMR spectroscopy in pharmaceutical research and analysis. *Trac-Trend Anal Chem* **2006**, *25* (10), 977-984.
24. Elkhazab, A.; Sarkar, S.; Dinh, J. K.; Simpson, G. J.; Taylor, L. S., Variation in Supersaturation and Phase Behavior of Ezetimibe Amorphous Solid Dispersions upon Dissolution in Different Biorelevant Media. *Mol Pharmaceut* **2018**, *15* (1), 193-206.
25. Carlton, R. A., Polarized Light Microscopy. *Pharmaceutical Microscopy* **2011**, 7-64.

26. Sievens-Figueroa, L.; Bhakay, A.; Jerez-Rozo, J. I.; Pandya, N.; Romanach, R. J.; Michniak-Kohn, B.; Iqbal, Z.; Bilgili, E.; Dave, R. N., Preparation and characterization of hydroxypropyl methyl cellulose films containing stable BCS Class II drug nanoparticles for pharmaceutical applications. *Int J Pharmaceut* **2012**, *423* (2), 496-508.
27. Franken, P. A.; Weinreich, G.; Peters, C. W.; Hill, A. E., Generation of Optical Harmonics. *Phys Rev Lett* **1961**, *7* (4), 118-&.
28. Maiman, T. H., Optical and Microwave-Optical Experiments in Ruby. *Phys Rev Lett* **1960**, *4* (11), 564-566.
29. Eisenthal, K. B., Equilibrium and Dynamic Processes at Interfaces by 2nd Harmonic and Sum Frequency Generation. *Annu Rev Phys Chem* **1992**, *43*, 627-661.
30. Kestur, U. S.; Wanapun, D.; Toth, S. J.; Wegiel, L. A.; Simpson, G. J.; Taylor, L. S., Nonlinear optical imaging for sensitive detection of crystals in bulk amorphous powders. *J Pharm Sci-Us* **2012**, *101* (11), 4201-4213.
31. Kissick, D. J.; Wanapun, D.; Simpson, G. J., Second-Order Nonlinear Optical Imaging of Chiral Crystals. *Annu Rev Anal Chem* **2011**, *4*, 419-437.
32. Wampler, R. D.; Kissick, D. J.; Dehen, C. J.; Gualtieri, E. J.; Grey, J. L.; Wang, H. F.; Thompson, D. H.; Cheng, J. X.; Simpson, G. J., Selective Detection of Protein Crystals by Second Harmonic Microscopy. *J Am Chem Soc* **2008**, *130* (43), 14076-+.
33. Wanapun, D.; Kestur, U. S.; Kissick, D. J.; Simpson, G. J.; Taylor, L. S., Selective Detection and Quantitation of Organic Molecule Crystallization by Second Harmonic Generation Microscopy. *Anal Chem* **2010**, *82* (13), 5425-5432.
34. Newman, J. A.; Schmitt, P. D.; Toth, S. J.; Deng, F. Y.; Zhang, S. J.; Simpson, G. J., Parts per Million Powder X-ray Diffraction. *Anal Chem* **2015**, *87* (21), 10950-10955.
35. Toth, S. J.; Madden, J. T.; Taylor, L. S.; Marsac, P.; Simpson, G. J., Selective Imaging of Active Pharmaceutical Ingredients in Powdered Blends with Common Excipients Utilizing Two-Photon Excited Ultraviolet-Fluorescence and Ultraviolet-Second Order Nonlinear Optical Imaging of Chiral Crystals. *Anal Chem* **2012**, *84* (14), 5869-5875.
36. Schmitt, P. D.; DeWalt, E. L.; Dow, X. Y.; Simpson, G. J., Rapid Discrimination of Polymorphic Crystal Forms by Nonlinear Optical Stokes Ellipsometric Microscopy. *Anal Chem* **2016**, *88* (11), 5760-5768.
37. Chowdhury, A. U.; Ye, D. H.; Song, Z. T.; Zhang, S. J.; Hedderich, H. G.; Mallick, B.; Thirunahari, S.; Ramakrishnan, S.; Sengupta, A.; Gualtieri, E. J.; Bouman, C. A.; Simpson, G. J., Second Harmonic Generation Guided Raman Spectroscopy for Sensitive Detection of Polymorph Transitions. *Anal Chem* **2017**, *89* (11), 5959-5966.
38. Raman, C. V., A change of wave-length in light scattering. *Nature* **1928**, *121*, 619-619.

39. Colthup, N., *Introduction to infrared and Raman spectroscopy*. Elsevier: 2012.
40. Dieing, T.; Hollricher, O.; Toporski, J., *Confocal raman microscopy*. Springer: 2011; Vol. 158.
41. Park, S. C.; Kim, M.; Noh, J.; Chung, H.; Woo, Y.; Lee, J.; Kemper, M. S., Reliable and fast quantitative analysis of active ingredient in pharmaceutical suspension using Raman spectroscopy. *Anal Chim Acta* **2007**, *593* (1), 46-53.
42. Kong, L. B.; Zhang, P. F.; Setlow, P.; Li, Y. Q., Multifocus confocal Raman microspectroscopy for rapid single-particle analysis. *J Biomed Opt* **2011**, *16* (12).

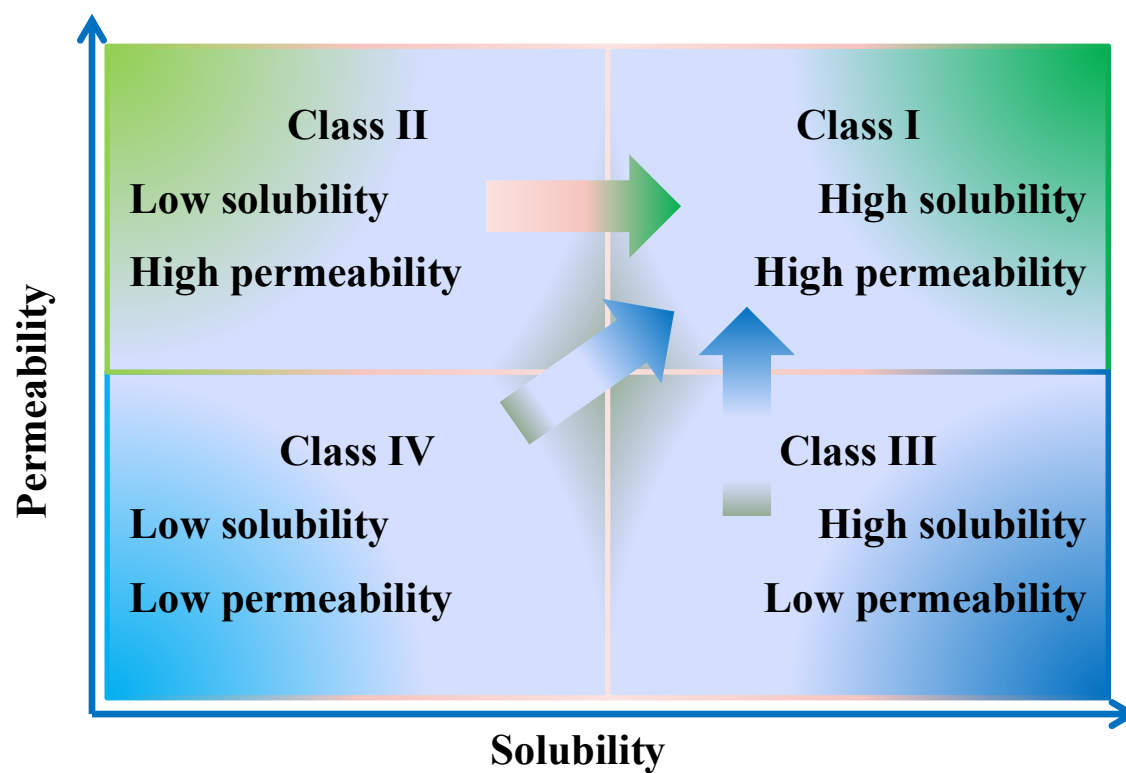


Figure 1-1 Four classes of APIs based on solubility and permeability

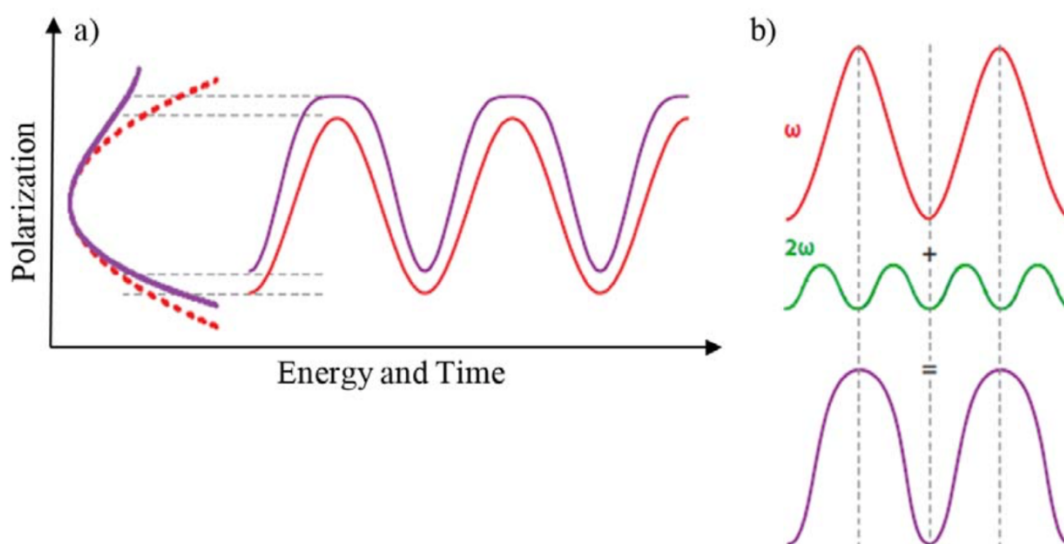


Figure 1-2 Representation of second harmonic generation

a) Distortions of induced molecular polarization in time domain; b) the distorted oscillation (purple line) can be recovered by the fundamental frequency (red line) and second harmonic frequency (green line).

CHAPTER 2. KINETIC MODELING OF ACCELERATED STABILITY TESTING BY SECOND HARMONIC GENERATION MICROSCOPY

Adapted with permission from Song, Z., Sarkar S., Vogt A. D., Danzer G. D., Smith C. J., Gualtieri E. J., Simpson G. J. "Kinetic modeling of accelerated stability testing enabled by second harmonic generation microscopy", *Anal. Chem.*, **2018**, 90(7), 4406-4413. Copyright 2018 American Chemical Society.

2.1 Introduction

Many emerging drug candidates exhibit low aqueous solubility, which can directly impact bioavailability and ultimately efficacy. In such cases, the bioavailability of an active pharmaceutical ingredient (API) is routinely improved by rendering the API amorphous within a polymer matrix to form an amorphous solid dispersion (ASD).¹⁻² However, ASDs are generally metastable systems; spontaneous crystallization of the API during storage at elevated relative humidity, for example, or processing can negatively impact the bioavailability of the API. The effective dose of a formulation may be lower than the intended dose. Furthermore, residual crystals present upon dissolution may serve as nuclei for re-crystallization following dissolution under conditions of supersaturation.³ To mitigate these complications, extensive accelerated stability testing methods are currently performed to quantify trace crystallinity present in ASDs under stressed conditions, as stability testing under ambient conditions is prohibitively time-consuming.⁴⁻

5

In principle, kinetic modeling at elevated temperatures and humidity can be used to predict stability under ambient conditions, which is ultimately the defining property of interest.⁶⁻⁷ Two key kinetic processes are most directly relevant: molecular diffusion, and crystal nucleation/growth. Parameterized models for nucleation and growth allow prediction of time-dependent crystallization under ambient conditions. Given the exponential dependence of the crystallinity on many of the recovered parameters, experimental uncertainties can have large impacts on the predicted behaviors. Confident determination of reliable kinetic parameters is most directly obtained through acquisition over a large range of concentrations, suggesting the need for sensitive methods capable of quantification at the early stages of crystallization. Kinetic modeling is arguably simplest to interpret from measurements acquired in the low crystallinity regime, in which local depletion and concentration gradients are negligible. The relatively low drug loading

present in many ASDs further exacerbates the challenges in acquisition of kinetic data over a large dynamic range.

The most common benchtop methods for characterizing crystallinity *in situ* for kinetic modeling routinely exhibit limits of detection within an order of magnitude of the total drug loading, greatly reducing the accessible dynamic range for quantifying crystallinity. A suite of methods is typically brought to bear to inform stability assessments of ASDs, including polarized light microscopy (PLM)⁹, differential scanning calorimetry (DSC)¹⁰⁻¹¹, X-ray powder diffraction (XRPD),¹² and solid-state NMR spectroscopy (ssNMR)¹³⁻¹⁴. PLM is arguably the most common method currently used to detect crystallinity in ASDs during stability testing. However, it only provides qualitative information of optically transparent samples for Boolean assessments and routinely exhibits interferences by occlusions, contaminants, and other crystalline excipients.⁹ DSC can provide information about thermal processes such as solid-solid transition, but lacks the sensitivity to allow trace detection.¹⁵ XRPD, the current gold-standard method for crystallinity, detection also suffers from a relatively high detection limit.¹⁶ Detection of crystallinity below 1% is challenging for the above analytical techniques.¹⁵ Solid-state NMR has been used to quantitatively determine all components in ASDs¹³ with detection limits as low as 0.4% for carbon¹⁴. However, ssNMR is costly and requires a relatively long sample analysis time.

Nonlinear optical imaging has recently emerged as a successful method in the pharmaceutical field for the sensitive detection of trace crystallization in amorphous systems.¹⁷⁻¹⁹ Second harmonic generation (SHG), in particular, is a scattering process, in which the incoming light is converted to light of twice the frequency.²⁰ The particular symmetry properties of SHG only permit this second-order process in non-centrosymmetric systems such as chiral crystals, whereas amorphous systems do not generate coherent SHG signal and negligible background.²¹⁻²³ SHG microscopy has been demonstrated as a powerful method for the detection of non-centrosymmetric crystals with low detection limits, which shows high potential for accelerated stability testing of ASDs.¹⁷

Ritonavir is an active ingredient in many successful anti-HIV formulations with extensively studied crystallization kinetics.²⁴⁻²⁵ Given the rich phase behavior of ritonavir, a substantial body of literature has accumulated for modeling crystallization of amorphous ritonavir, both as a pure compound and as an amorphous formulation. In a recent study centered on crystallization of ritonavir and formulations containing amorphous ritonavir, Zhu *et al.*²⁶

performed a series of stability experiments to develop predictive models for ritonavir crystallization behaviors, as a case study. The kinetic modeling was performed based on determination of the induction time, corresponding to the minimum time required to detect onset of crystallization.

In this work, we seek to significantly expand upon the results of the preceding studies with ritonavir to interrogate the early stage ($\ll 1\%$) crystalline regime by SHG microscopy. Accelerated stability testing has been carried out on a model ritonavir-ASD to determine the detection of limit of SHG microscopy and assess the utility of the approach for informing kinetic modeling of crystal nucleation and growth. Specifically, the primary objective of the present work is the development of parameterized models for early-stage crystal nucleation and growth kinetics that can be used for quantitatively assessing the anticipated stability under ambient conditions.

2.2 Methods

Amorphous ritonavir extrudate with 15% (w/w) ritonavir (manufactured by AbbVie), copovidone (BASF), plasticizer/surfactant and silicon dioxide was prepared by hot melt extrusion, as previously described²⁷⁻²⁸ and then milled to a powder. The dry glass transition temperature of the milled extrudate was 56 °C, as measured by DSC. For the studies described herein, samples were prepared by placing powdered extrudates on the glass slides as a thin layer ($\sim 300\ \mu\text{m}$) over a sample area of $\sim 1\ \text{cm}^2$. For accelerated stability testing, samples were stressed at 50°C/75% relative humidity (RH) or 40°C/75% RH. SHG microscopy was used to observe the crystallization of stressed amorphous ritonavir at early times (0hrs. – 24hrs.). At this RH, the extrudates exhibited low turbidity, suggestive of temperatures above the glass transition temperature. High RH is known to suppress the glass transition temperature of copovidone²⁹.

SHG images were acquired by using a commercial SONICC (second-order nonlinear optical imaging of chiral crystals) microscope (Formulatrix, Inc.), modified in-house for compatibility with powder analysis. Specifically, the instrument was redesigned to allow epi-detection of SHG (details shown in supporting information). The system was powered by a Fianium FemtoPower laser (1060 nm, 170 fs, 50 MHz). A resonant mirror (8 kHz) and a galvanometer mirror are used for beam scanning to generate SHG images. The Formulatrix SONICC instrument was modified from its original configuration to be able to detect SHG signal in the epi direction while maintaining its capacity to perform epi-detected two photon excited UV

fluorescence (TPE-UVF) and transmission-detected SHG. This was accomplished by replacing the existing pre-objective dichroic mirror with a thin film 45degree polarizer (Advanced Thin Films, PO1045-DY). This polarizer passes *p*-polarized 532 nm light and reflects the orthogonal polarization. This enabled the transmission of the incident light in TPE-UVF measurements and reflection of a large fraction of the doubled frequency light in SHG measurements (1064 nm incident). Additionally, a replacement dichroic mirror (1" round long pass dichroic, cutoff wavelength at ~410 nm) capable of reflecting TPE-UVF (red shifted from 266 nm) was spatially collocated with the thin film polarizer. Because the instrument lacked sufficient space to immediately image the signal onto an additional PMT, a liquid light guide was used to direct the light to a PMT positioned in empty space in the back of the mechanical loading system. The existing epi PMT was also moved from its original location and placed at the exit of the liquid light guide. The original pre-objective dichroic mirror was used to separate SHG and TPE-UVF wavelengths to these respective PMTs (post-liquid light guide). The added PMT was a Hamamatsu E990-501 with appropriate band pass filters for SHG. An external power supply was used to power the added PMT.

In this study, all of the SHG images were acquired with 350 mW excitation laser power at the sample and each field of view was ~2.0 mm × 2.0 mm. This power level is significantly higher than typically used in NLO microscopy measurements of tissue samples. However, the power density at the sample was relatively low, as all measurements were acquired with a low numerical aperture objective (NA = 0.3) over a large field of view (>4 mm²). Furthermore, the use of a fast-scan (8 kHz) resonant mirror with the beam blocked at the turning points reduced the single-pass exposure for each pixel to ~50 ns (or approx. 2-3 laser pulses) per scan, then allowed for 1/30 s of thermal relaxation prior to subsequent sampling. For unstressed samples, the SHG signal was collected in the epi direction (*i.e.*, back through the same objective used to deliver the infrared beam), as powders typically generate little signal in transmission due to optical scattering. For the ritonavir milled extrudate samples stressed at either 50°C or 40°C with 75%RH, SHG signal was collected in transmission. Two replicates of each sample were prepared, and three different positions of each sample were observed for a total of six fields of view obtained for each time-point. ImageJ was used to analyze the SHG images based on particle counting analysis as described previously.¹⁹

2.3 Theory

Crystal growth rates can be independently and self-consistently modeled in terms of nucleation and diffusion-limited growth. Parameterized models for nucleation and fundamental models for growth allow prediction of time-dependent crystallization. The overall crystallization kinetics under isothermal conditions can be described by JMAK (Johnson, Mehl, Avrami and Kolmogorov) theory in terms of volume fraction of the new phase under the assumption that nucleation and growth rates are constant throughout the transformation.³⁰ In this theory, the volume fraction of the new phase, α is proposed by Equation 2-1, in which t represents time, t_0 is the induction time and is defined as the earliest detection of an SHG signal, I is the nucleation rate, and U is the crystal growth rate.

$$\alpha(t - t_0) = 1 - \exp \left\{ -g \int_{t_0}^t I(t') \left[\int_{t'}^t U(t'') dt'' \right]^3 dt' \right\} \quad (2-1)$$

For spherical crystals, the shape-factor g is $4\pi/3$. For steady-state homogeneous nucleation, nucleation and growth rates are considered to be constant; therefore, Equation 2-1 can be rewritten as Equation 2-2.

$$\alpha(t - t_0) = 1 - \exp \left[-\frac{gIU^3(t - t_0)^4}{4} \right] \quad (2-2)$$

The assumption of constant nucleation and growth rates are only expected to rigorously hold at the early stages of crystallization ($\ll 1\%$), for which the concentration of amorphous API is not significantly affected by the crystalline fraction. The assumption of approximately spherical particles may initially appear to be questionable given that pristine single crystals exhibit diverse habits. For high aspect ratio needle-like crystals, this assumption will no longer be valid. However, the ritonavir particles studies in the present case exhibit aspect ratios of less than 3, which is common in many pharmaceutically desirable materials given the challenges of manufacturing associated with needle-like crystals. In this range, the error introduced by assumption of approximately spheroidal particles is insignificant relative to the Poisson uncertainty introduced by the finite number of discrete crystals sampled.

The volume fraction of the transformed material can be recovered by simplification of the more general form of the JMAK equation as shown in Equation 2-3 by grouping constants and generalizing the exponential to an adjustable parameter.³⁰

$$\alpha(t - t_0) = 1 - \exp(-K(t - t_0)^n) \quad (2-3)$$

The parameter n is the Avrami coefficient and depends on both nucleation and crystal growth rates and thus from the formulas $N \propto (t-t_0)^k$ and $r \propto (t-t_0)^m$, which describe the variation in crystal number (N) and crystal size (r) with time.³⁰ The Avrami coefficient can be given by the following Equation 2-4.

$$n = k + 3m \quad (2-4)$$

The preceding expressions hold at a particular temperature, but stability testing is most commonly performed at as function of temperature in order to induce phase transformations in practical timescales. Connecting these accelerated stability test results back to room temperature behavior can be performed by considering the temperature dependence of diffusion and crystal growth. The growth rate of an individual crystal U (described by m in Equation 2-4) can be parameterized and related back to diffusion and the Gibbs free energy of crystallization through Equation 2-5.³⁰ In that equation, ΔG_V is the thermodynamic Gibbs free energy per unit volume of crystal, a is an average (effective) size parameter of the molecules building the crystalline phase, k_B is Boltzman's constant and f is a dimensionless parameter describing the different growth modes. For the continuous growth mechanism, which is assumed that the interface between the growing crystal and the surrounding medium displays a sufficiently high concentration of growth sites, $f=1$. U is the crystal growth rate, which is the slope from a plot of the mean crystal radius with time.

$$U = f \frac{D}{4a} \left[1 - \exp\left(-\frac{1}{2} \frac{\Delta G_V a^3}{k_B T}\right) \right] \quad (2-5)$$

In practice, the expression in Equation 2-5 can often be simplified if either diffusion limits the growth rate (in which case D dictates the overall kinetics) or if the Gibbs free energy term in the exponential represented by ΔG_V dictates the crystallization rate. Since the supersaturation decreases with increasing temperature, growth rates would be expected to decrease at elevated temperatures for crystallization under thermodynamic control. Under diffusion-limited growth conditions, the kinetics obey standard Arrhenius behaviors for diffusion $D = D_0 e^{-E_a/k_B T}$ at intermediate and lower temperatures.

The expression in Equation 2-5 allows prediction of the growth rates at temperatures other than those measured. Extrapolation from elevated temperature behavior to ambient conditions can provide a means for evaluating potential stability of ASDs, provided that no additional phase

transformations arise over temperatures not interrogated experimentally. The JMAK theory was implemented into kinetic model of ASD accelerated stability testing.

2.4 Results and Discussions

Under the condition for accelerated stability testing at both 50°C/75% RH and 40°C/75% RH, crystal growth kinetics from the 15% w/w amorphous ritonavir milled extrudate was recorded by collecting SHG images on a scheduled basis. Ten representative SHG images and corresponding bright field images are shown in Figure 2-1. All of the images are shown with the same brightness scale for comparative purposes. The SHG micrographs even at the earliest stages shown in the figure yield signals well above the noise floor of the instrument (i.e., particles with > 3 contiguous pixels exhibiting counts > 3 counts). The time-zero samples showed no detectable SHG, with the onset of detectable SHG at five hours for samples stressed at 50°C/75% RH and 40°C/75% RH. Compared with SHG-active particles shown in Figure 2-1B, the number and the average size of SHG-active particles are larger as shown in Figure 2-1A, which form the basis of more detailed kinetic analysis (see below).

The 15% drug loading (DL) ritonavir milled extrudate samples contained only amorphous ritonavir and copovidone. Neither of the components is SHG-active. Ritonavir crystals are non-centrosymmetric and SHG active.^{22, 32} For SHG images in Figure 2-1, the SHG-active areas represent ritonavir crystals. Based on the comparison of Figure 2-1A and Figure 2-1B, after the same stressed time, the milled extrudate stressed at 50°C/75% RH developed more ritonavir crystals with larger size than did the sample stressed at 40°C/75% RH.

A particle counting approach was used to quantify crystallinity at levels from ppm regime to 10%, which corrected particle-particle overlap. In brief, the volume of each individual crystallite was estimated based on the cross-sectional area of the particle. This approach removes noise associated with variance in the SHG intensity from differences in crystal orientation. Bias introduced from particle overlap for crystallinities >1% was removed using a size-distribution dependent correction algorithm detailed elsewhere.³² Although the algorithm as described is formally derived assuming spherical particles, the aspect ratio of the ritonavir particles (~3:1) is sufficiently low to allow reliable application of the method in the present study. A minimum crystal cross-sectional area of 45 μm^2 (corresponding to three contiguous pixels) was implemented in the algorithm to ensure statistical confidence in crystal identification by image analysis. Based on the

volume sampled as set by the depth of field and the field of view, this algorithm places a practical lower limit of ~ 0.5 ppm for detection of crystallinity. This limit is substantially higher than has been reported previously based on the minimum detectable radius of 100 nm. However, Poisson statistics associated with the stochastic nature of crystallization were found to be the dominant noise source in the analysis, which were minimized by maximizing both the depth of field and field of view. Despite the high limit of detection (LOD) imposed by the particle-counting algorithm relative to previous work, SHG still produced LOD which is several orders of magnitude lower than practically achievable by alternative routine benchtop methods.

Figure 2-2 shows the volume fraction of crystallinity from 15% amorphous ritonavir milled extrudate stressed at 50°C/75% RH (red) or 40°C/75% RH (blue) and corresponding fits to Equation 2-3. The crystallization rates were clearly not linear with each condition, exhibiting a significant induction time, which is tentatively attributed to the stochastic nature of nucleation coupled with the need to generate particles large enough to generate significant SHG ($> \sim 100$ nm) for detection.¹⁵ In this study, the induction time t_0 was approximately five hours for both samples stressed at 50°C/75% RH and 40°C/75% RH, which was the earliest time point at which the SHG was detected with statistical confidence (i.e., with a signal greater than 3-fold higher than the standard deviation of the blank).

The limits of detection based on SHG microscopy are defined to be the concentration corresponding to a signal three-fold higher than the standard deviation of the initially prepared samples. In Figure 2-2, the lower-limit for the SHG response is also shown on a log-scale in the inset figure, consistent with the form in Equation 2-3, calculated with the measured induction times. Both sets of fits (linear and log scaling) are shown with identical parameters in each case, given in Table 2-1. From the 40°C fits, SHG microscopy exhibited a lower detection limit of 10 ppm (v/v) for crystalline ritonavir in a milled extrudate powder, which is approximately two to three orders of magnitude lower than commonly used methods (DSC, XRPD, near IR). Given the similarities in the densities of copovidone and ritonavir, the volume ratio and the mass fraction are essentially identical.

With knowledge of the induction time, additional insights into the crystallization behavior can be recovered from particle-counting analysis of the SHG images, shown in Figure 2-3. The top part of the figure contains the histogram of particle sizes, indicating an increase in both the number of crystals and the distribution of crystal sizes with time. To assess the crystal growth rate,

the mean crystal radii were calculated by using the mean crystal size from the distribution. The time-dependent evolutions of the mean crystal radius were given by the bottom two plots. A log-log plot of mean crystal radius versus time in Figure 2-3C was used to extract the exponential scaling parameter m , assuming that the particle size scales as $r \propto (t-t_0)^m$. This scaling is consistent with expectations for the derivation of Equation 2-4. An estimate of the steady-state growth rate was generated from the latest five time points under each of the two stressed conditions as shown in Figure 2-3D.

Particle counting approaches also allow determination of both the number of particles, and the rate of new particle production (i.e., nucleation rate). The total crystalline volume fraction is a function of the combined rates of nucleation and growth through Equations 2-3 and 2-4. In Figure 2-4A, log-log plots of the nucleation rate recover the exponential parameter k in Equation 2-4 from the slope, based on the relationship $N \propto (t-t_0)^k$. In contrast to the crystal growth rate, the nucleation rates (N versus t) were similar for both temperatures tested as shown in Figure 2-4B. It is worth noting that the nucleation rate was evaluated from data points appearing after the induction time, corresponding to the steady-state rate at which particles have both nucleated and subsequently grown to a size commensurate with reliable detection by SHG. As such, the nucleation rate is unbiased by the presence of a finite induction time.

Independent determination of the crystal nucleation and growth kinetics from particle counting of the SHG-active domains allows evaluation of the exponential parameters describing the overall crystallinity in Equation 2-4. For crystallization reliably described by the JMAK model, the relationship $n \cong k + 3m$ is expected together with the total crystallinity scaling linearly with the average nucleation rate and cubically with the growth rate in the average particle radius. The slope results shown in Table 2-1 were fit via Equation 2-4 and show good internal consistency with these expectations, suggesting general validity for use of the JMAK model.

While the nucleation kinetics were largely insensitive to the difference in temperature over the regime investigated as shown in Figure 2-4, the crystal growth kinetics in Figure 2-3 exhibited a steep temperature-dependence. A temperature-insensitive nucleation rate is consistent with a system in which both thermodynamics and kinetics play significant roles in driving nucleation. As the temperature is decreased, thermodynamics suggests a higher supersaturation and a corresponding increase in nucleation rate (according to classical nucleation theory³⁰). In contrast, diffusion models suggest higher nucleation rates with increasing temperature for mass-transport

limited processes. These two effects are described by ΔG_V and D in Equation 2-5, respectively. A weak temperature dependence for nucleation, as observed for the current study, suggests that both effects are significant, such that the decrease in nucleation rates from thermodynamics as supersaturation decreases is largely offset by an increase in nucleation rates from diffusion at elevated temperature.

The increase in crystal growth rates with increased temperature is consistent with diffusion-limited kinetics over the temperatures investigated. In this case, simplification of Equation 2-5 to the diffusion-only expression enables Arrhenius descriptions of diffusion. In order to extract the Arrhenius parameters for predicting the temperature-dependence of diffusion (and in turn, crystal growth rate), an estimate of the steady-state growth rate was generated from the latest five time points under each of the two stressed conditions explored, shown in Figure 2-3D. These points contained the least number of crystallites smaller than the lower limits of detection of the instrument. In this regime, the growth rates based on crystal size changes was most confidently recorded with minimal bias from nucleation. In this temperature range, the crystal growth rate was mainly dominated by diffusion. Based on the temperature-dependent crystal growth rate, the calculated activation energy of diffusion is 68.8 ± 4.3 kJ/mol, which is generally consistent with previously reported values for polymers.³³⁻³⁴

It is worth comparing the results of the kinetic modeling of the SHG data to analogous modeling performed using conventional methods for crystallinity determination. The low limits of detection by SHG significantly reduce the induction time required to first observe onset of detectable crystallinity for integration into kinetic modeling. In the case of API crystallization in amorphous solid dispersion, limits of detection on the order of 0.5% crystallinity are enabled by XRPD with a synchrotron source.¹⁶ From inspection of Figure 2-2, this limit of detection would correspond to four data points in the 50°C/75%RH crystallization trial and two data points in the 40°C/75%RH trial over the same time frame of the experiment. With so few data points available, it would be challenging at best to assess the validity of any particular model for predicting crystallization kinetics by XRPD alone. In principle, longer times could be devoted to monitoring crystallization (*e.g.*, several days or longer). However, the modeling becomes more challenging as the concentration of solubilized drug and the corresponding degree of supersaturation changes significantly at higher crystallinity. In addition, the present study was performed under conditions leading to relatively rapid crystal formation. For stability testing performed approximating ambient

conditions, the timeframes required for observation of crystallinity to inform modeling by conventional benchtop methods can become prohibitive for routine optimization of formulations.

The importance of quantitative modeling for predictive behavior is particularly relevant to pharmaceutical analysis given the regulatory shifts toward quality by design (QbD) concepts for pharmaceutical characterization. QbD approaches rely on quantitative understanding of key aspects of the formulation for predicting performance and bioavailability. For ASDs, stability is arguably one of the most critical factors to evaluate. The results summarized in Figure 2-2 demonstrate a dynamic range of detection by SHG spanning more than four decades (100 ppm to several %), the collective results of which can be integrated into a single unified kinetic model capable of predicting both the overall number and size distribution of API crystals under diverse storage conditions. In contrast, the dynamic range of many alternative benchtop methods routinely span single order of magnitude or less. Also, it can provide little direct information on the size distribution. Consequently, the predictive capability of SHG microscopy measurements for QbD assessments is significantly improved relative to alternative established methods for samples amenable to SHG analyses. By using parameterized models, the measurements also allow prediction of anticipated trends under alternative conditions (*e.g.*, ambient). This predictive ability can benefit long-term stability assessments for which the direct measurements are prohibitively time-consuming during formulation optimization.

While the use of SHG for analysis of amorphous solid dispersions has been demonstrated previously¹⁵, the present study is unique in the use of image analysis for determination of not only the percent crystallinity, but recovery of the particle size distribution at each time-point. This additional information enabled independent determination of the nucleation and crystal growth rates, both of which combine to provide a complete description of crystallization kinetics in amorphous solid dispersions. Dissolution kinetics, and correspondingly bioavailability is profoundly impacted by the particle size distribution, with dissolution arising more rapidly from a large number of small crystals as opposed to a small number of large crystals.³⁵

The SHG image analysis approach demonstrated in this work also has distinct practical advantages over established methods such as PLM. PLM can exhibit limits of detection well below 1% under favorable conditions. However, the image contrast for crystals is reduced by the presence of false-positive contributions from surface/edge effects in the sample, occlusions, scattering, etc. Representative SHG and PLM images are provided in Figure 2-5. The high background and false-

positives within the PLM images effectively render most automated particle counting image analysis approaches inapplicable, such that images are often interpreted manually. In contrast, SHG exhibits little detectable background from occlusions and the polymer matrix, such that the resulting images are directly compatible with well-established and relatively simple automated image analysis algorithms. Compatibility with automated operation is clearly an attractive property for widespread adoption within the pharmaceutical community.

The particle counting approach described herein has the distinct advantage of being applicable irrespective of the crystal form of the SHG-active moiety or the need for calibration with a pure substance. Crystallinity is assessed entirely based on the calculated volume from individual particles. This capability is particularly advantageous in studies of pharmaceutical materials, as APIs often exhibit rich phase behavior with several crystal forms and/or polymorphs potentially accessible for crystal formation. Ritonavir is a particularly well-studied example of crystal polymorphism, in which the Form II polymorph exhibits significantly lower bioavailability in oral formulations relative to the metastable Form I. Confocal Raman and near infrared spectra acquired from later stages in the crystallization were consistent with the more stable Form II produced in the present study, which are shown in Figure 2-6. Such combined measurements highlight the advantages of coupling quantitative analysis approaches such as SHG with qualitatively rich spectroscopic characterization methods.

While the focus of the present study is centered on characterization of extruded feedstock materials, it is worthwhile to consider the challenges associated with accelerated stability assessments in final dosage forms. For oral dosage forms comprised of compressed powders, additional crystalline excipients may be present in addition to the ASDs. Several strategies have been pursued for enabling quantitative analysis by SHG in these more complex matrices. UV-SHG has been shown to exhibit enhanced selectivity for aromatic APIs, enabling selective detection of crystalline API in the presence of crystalline sugars (e.g., lactose and mannitol).¹⁸ In addition, SHG-active particles can be targeted for subsequent Raman microscopy measurements for definitive determination of composition on a per-particle basis.²¹ Alternatively, synchrotron XRD can inform structural composition of individual microscopic particles identified for analysis by SHG.³² These strategies are generally compatible with the kinetic modeling approach described herein, although with the caveat that the lower limits of detection and temporal resolution may be compromised in complex multi-component mixtures containing additional SHG-active excipients.

Final dosage forms with amorphous excipients can generally be expected to be directly compatible with SHG analysis for quantification of crystallinity¹⁹.

2.5 Conclusion

In this study, SHG microscopy was used to develop analytical models for predicting the crystallization behavior of ritonavir in a model ASD formulation. The low (10 ppm v/v) limit of detection of SHG microscopy extended the range of data to incorporate into the model by ~2 orders of magnitude lower compared to other routine benchtop methods (*e.g.*, DSC, XRPD) for ritonavir crystallinity detection in ASDs. Most significantly, SHG extends the measurement into the low crystallinity regime, in which the analytical modeling is simplified by the assumption of a constant average concentration in the polymer. Image analysis of the SHG micrographs allowed separate evaluation of contributions from both nucleation and growth in dictating the overall net kinetics of crystallization. The values of crystallinity were demonstrated to be consistent with the JMAK kinetic model. This information allows prediction of both the anticipated crystalline fraction as well as the crystalline number density and size distribution. The temperature-dependent changes in the SHG microscopy images allowed for determination of a diffusional activation energy, which in turn allowed for modeling to predict the anticipated kinetics under unique experimental conditions. Since these results build off measurements acquired primarily for crystalline fractions much lower than 0.5%, the overall timeframe for optimization of a particular ASD formulation has the potential to be substantially reduced through integration of SHG imaging. Consequently, full kinetic modeling with predictive capability can be performed with a collective set of measurements obtained at crystallinities below those typically required for simple pass/fail Boolean assessments in formulation optimization. Finally, mathematical understanding of the kinetics of crystallization facilitates quality by design approaches in the development of formulations.

2.6 References

1. Serajuddin, A. T. M., Solid dispersion of poorly water-soluble drugs: Early promises, subsequent problems, and recent breakthroughs. *J Pharm Sci* 1999, 88 (10), 1058-1066.
2. Kennedy, M.; Hu, J.; Gao, P.; Li, L.; Ali-Reynolds, A.; Chal, B.; Gupta, V.; Ma, C.; Mahajan, N.; Akrami, A.; Surapaneni, S., Enhanced Bioavailability of a Poorly Soluble

- VR1 Antagonist Using an Amorphous Solid Dispersion Approach: A Case Study. *Mol Pharmaceut* 2008, 5 (6), 981-993.
3. Guo, Y. S.; Shalaev, E.; Smith, S., Physical stability of pharmaceutical formulations: solid-state characterization of amorphous dispersions. *Trac-Trend Anal Chem* 2013, 49, 137-144.
 4. Kommanaboyina, B.; Rhodes, C. T., Trends in stability testing, with emphasis on stability during distribution and storage. *Drug Dev Ind Pharm* 1999, 25 (7), 857-868.
 5. Waterman, K. C.; Adami, R. C., Accelerated aging: Prediction of chemical stability of pharmaceuticals. *Int J Pharm* 2005, 293 (1-2), 101-125.
 6. Yang, J.; Grey, K.; Doney, J., An improved kinetics approach to describe the physical stability of amorphous solid dispersions. *Int J Pharm* 2010, 384 (1-2), 24-31.
 7. Sinclair, W.; Leane, M.; Clarke, G.; Dennis, A.; Tobyn, M.; Timmins, P., Physical Stability and Recrystallization Kinetics of Amorphous Ibipinabant Drug Product by Fourier Transform Raman Spectroscopy. *J Pharm Sci* 2011, 100 (11), 4687-4699.
 8. Schmelzer, J. W. P.; Boltachev, G. S.; Baidakov, V. G., Classical and generalized Gibbs' approaches and the work of critical cluster formation in nucleation theory. *J Chem Phys* 2006, 124 (19), 194503.
 9. Carlton, R. A., Polarized Light Microscopy. In *Pharmaceutical Microscopy*, Springer: New York, NY, 2011; pp 7-64.
 10. Yoshihashi, Y.; Iijima, H.; Yonemochi, E.; Terada, K., Estimation of physical stability of amorphous solid dispersion using differential scanning calorimetry. *J Therm Anal Calorim* 2006, 85 (3), 689-692.
 11. Baird, J. A.; Taylor, L. S., Evaluation of amorphous solid dispersion properties using thermal analysis techniques. *Adv Drug Deliver Rev* 2012, 64 (5), 396-421.
 12. Ghebremeskel, A. N.; Vemavarapu, C.; Lodaya, M., Use of surfactants as plasticizers in preparing solid dispersions of poorly soluble API: Stability testing of selected solid dispersions. *Pharm Res-Dordr* 2006, 23 (8), 1928-1936.
 13. Berendt, R. T.; Sperger, D. M.; Isbester, P. K.; Munson, E. J., Solid-state NMR spectroscopy in pharmaceutical research and analysis. *Trac-Trend Anal Chem* 2006, 25 (10), 977-984.
 14. Lubach, J. W.; Padden, B. E.; Winslow, S. L.; Salsbury, J. S.; Masters, D. B.; Topp, E. M.; Munson, E. J., Solid-state NMR studies of pharmaceutical solids in polymer matrices. *Anal Bioanal Chem* 2004, 378 (6), 1504-1510.

15. Wanapun, D.; Kestur, U. S.; Kissick, D. J.; Simpson, G. J.; Taylor, L. S., Selective Detection and Quantitation of Organic Molecule Crystallization by Second Harmonic Generation Microscopy. *Anal Chem* 2010, 82 (13), 5425-5432.
16. Thakral, S.; Terban, M. W.; Thakral, N. K.; Suryanarayanan, R., Recent advances in the characterization of amorphous pharmaceuticals by X-ray diffractometry. *Adv Drug Deliver Rev* 2016, 100, 183-193.
17. Kissick, D. J.; Wanapun, D.; Simpson, G. J., Second-Order Nonlinear Optical Imaging of Chiral Crystals. *Annu Rev Anal Chem* 2011, 4, 419-437.
18. Toth, S. J.; Madden, J. T.; Taylor, L. S.; Marsac, P.; Simpson, G. J., Selective Imaging of Active Pharmaceutical Ingredients in Powdered Blends with Common Excipients Utilizing Two-Photon Excited Ultraviolet-Fluorescence and Ultraviolet-Second Order Nonlinear Optical Imaging of Chiral Crystals. *Anal Chem* 2012, 84 (14), 5869-5875.
19. Schmitt, P. D.; Trasi, N. S.; Taylor, L. S.; Simpson, G. J., Finding the Needle in the Haystack: Characterization of Trace Crystallinity in a Commercial Formulation of Paclitaxel Protein-Bound Particles by Raman Spectroscopy Enabled by Second Harmonic Generation Microscopy. *Mol Pharmaceut* 2015, 12 (7), 2378-2383.
20. Chowdhury, A. U.; Zhang, S. J.; Simpson, G. J., Powders Analysis by Second Harmonic Generation Microscopy. *Anal Chem* 2016, 88 (7), 3853-3863.
21. Chowdhury, A. U.; Ye, D. H.; Song, Z. T.; Zhang, S. J.; Hedderich, H. G.; Mallick, B.; Thirunahari, S.; Ramakrishnan, S.; Sengupta, A.; Gualtieri, E. J.; Bouman, C. A.; Simpson, G. J., Second Harmonic Generation Guided Raman Spectroscopy for Sensitive Detection of Polymorph Transitions. *Anal Chem* 2017, 89 (11), 5959-5966.
22. Toth, S. J.; Schmitt, P. D.; Snyder, G. R.; Trasi, N. S.; Sullivan, S. Z.; George, I. A.; Taylor, L. S.; Simpson, G. J., Ab Initio Prediction of the Diversity of Second Harmonic Generation from Pharmaceutically Relevant Materials. *Cryst Growth Des* 2015, 15 (2), 581-586.
23. Schmitt, P. D.; DeWalt, E. L.; Dow, X. Y.; Simpson, G. J., Rapid Discrimination of Polymorphic Crystal Forms by Nonlinear Optical Stokes Ellipsometric Microscopy. *Anal Chem* 2016, 88 (11), 5760-5768.
24. Danner, S. A.; Carr, A.; Leonard, J. M.; Lehman, L. M.; Gudiol, F.; Gonzales, J.; Raventos, A.; Rubio, R.; Bouza, E.; Pintado, V.; Aguado, A. G.; Delomas, J. G.; Delgado, R.; Borleffs, J. C. C.; Hsu, A.; Valdes, J. M.; Boucher, C. A. B.; Cooper, D. A.; Gimeno, C.; Clotet, B.; Tor, J.; Ferrer, E.; Martinez, P. L.; Moreno, S.; Zancada, G.; Alcami, J.; Noriega, A. R.; Pulido, F.; Glassman, H. N., A Short-Term Study of the Safety, Pharmacokinetics, and Efficacy of Ritonavir, an Inhibitor of Hiv-1 Protease. *New Engl J Med* 1995, 333 (23), 1528-1533.

25. Bauer, J.; Spanton, S.; Henry, R.; Quick, J.; Dziki, W.; Porter, W.; Morris, J., Ritonavir: An extraordinary example of conformational polymorphism. *Pharm Res-Dordr* 2001, *18* (6), 859-866.
26. Zhu, D. H.; Zografi, G.; Gao, P.; Gong, Y. C.; Zhang, G. G. Z., Modeling Physical Stability of Amorphous Solids Based on Temperature and Moisture Stresses. *J Pharm Sci* 2016, *105* (9), 2932-2939.
27. Breitenbach, J., Melt extrusion: from process to drug delivery technology. *Eur J Pharm Biopharm* 2002, *54* (2), 107-117.
28. Tho, I.; Liepold, B.; Rosenberg, J.; Maegerlein, M.; Brandl, M.; Fricker, G., Formation of nano/micro-dispersions with improved dissolution properties upon dispersion of ritonavir melt extrudate in aqueous media. *Eur J Pharm Sci* 2010, *40* (1), 25-32.
29. Oksanen, C. A.; Zografi, G., The Relationship between the Glass-Transition Temperature and Water-Vapor Absorption by Poly(Vinylpyrrolidone). *Pharm Res-Dordr* 1990, *7* (6), 654-657.
30. Schmelzer, J. W., *Nucleation theory and applications*. WILEY-VCH: Weinheim, 2005.
31. Gutzow, I.; Schmelzer, J., *The vitreous state: thermodynamics, structure, rheology and crystallization*. Springer: Berlin et al., 1995.
32. Newman, J. A.; Schmitt, P. D.; Toth, S. J.; Deng, F. Y.; Zhang, S. J.; Simpson, G. J., Parts per Million Powder X-ray Diffraction. *Anal Chem* 2015, *87* (21), 10950-10955.
33. Schmitt, E. A.; Law, D.; Zhang, G. G. Z., Nucleation and crystallization kinetics of hydrated amorphous lactose above the glass transition temperature. *J Pharm Sci* 1999, *88* (3), 291-296.
34. Vrentas, J. S.; Vrentas, C. M., Diffusion in glassy polymers. *J Polym Sci Pol Phys* 2003, *41* (8), 785-788.
35. Amidon, G. L.; Lennernas, H.; Shah, V. P.; Crison, J. R., A Theoretical Basis for a Biopharmaceutic Drug Classification - the Correlation of in-Vitro Drug Product Dissolution and in-Vivo Bioavailability. *Pharm Res-Dordr* 1995, *12* (3), 413-420.

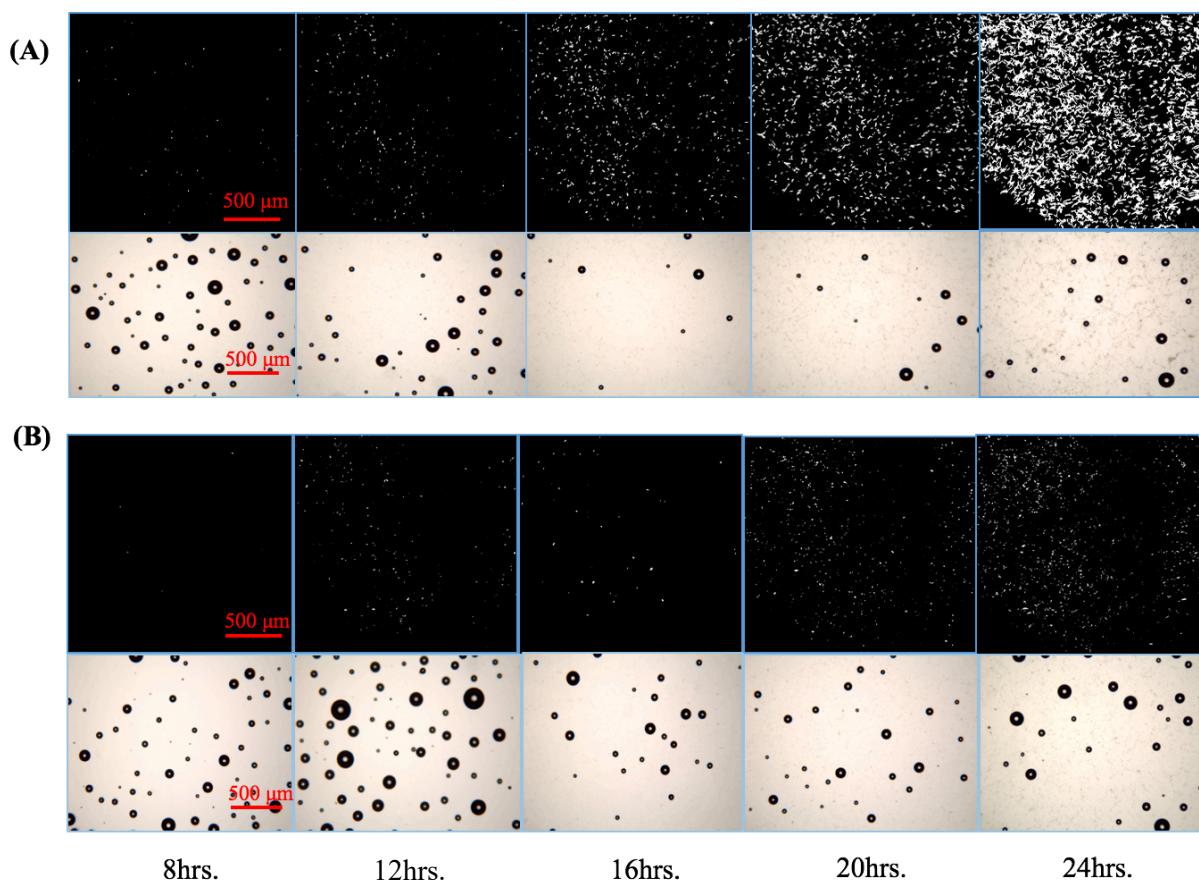


Figure 2-1 SHG and bright field images for accelerated stability testing 15% ritonavir milled extrudate stressed in (A) 50°C/75% RH and (B) 40°C/75% RH standard chambers. Top: SHG images; Bottom: bright field images. The spherical occlusions in the bright field images correspond to air pockets within the partially melted copovidone matrix. After ~16 hours, crystals can be observed by bright field imaging with low contrast.

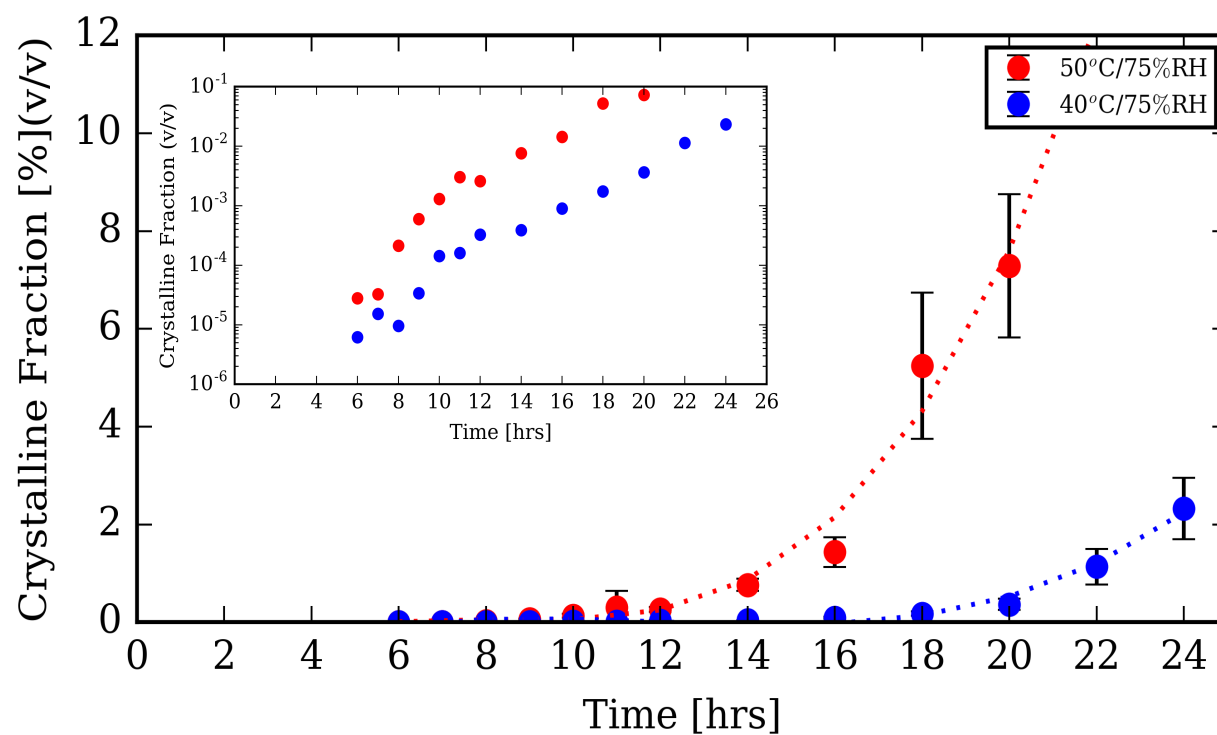


Figure 2-2 Volume fraction of crystallinity in accelerated stability testing. 15% DL amorphous ritonavir milled extrudate (ASDs) under different stress conditions, which show the formation and evolution of crystals with time. Limit of detection is as low as 10 ppm (0.001%) of the total drug load. The inset plot is in log-scale to highlight the limit of detection at 10 ppm.

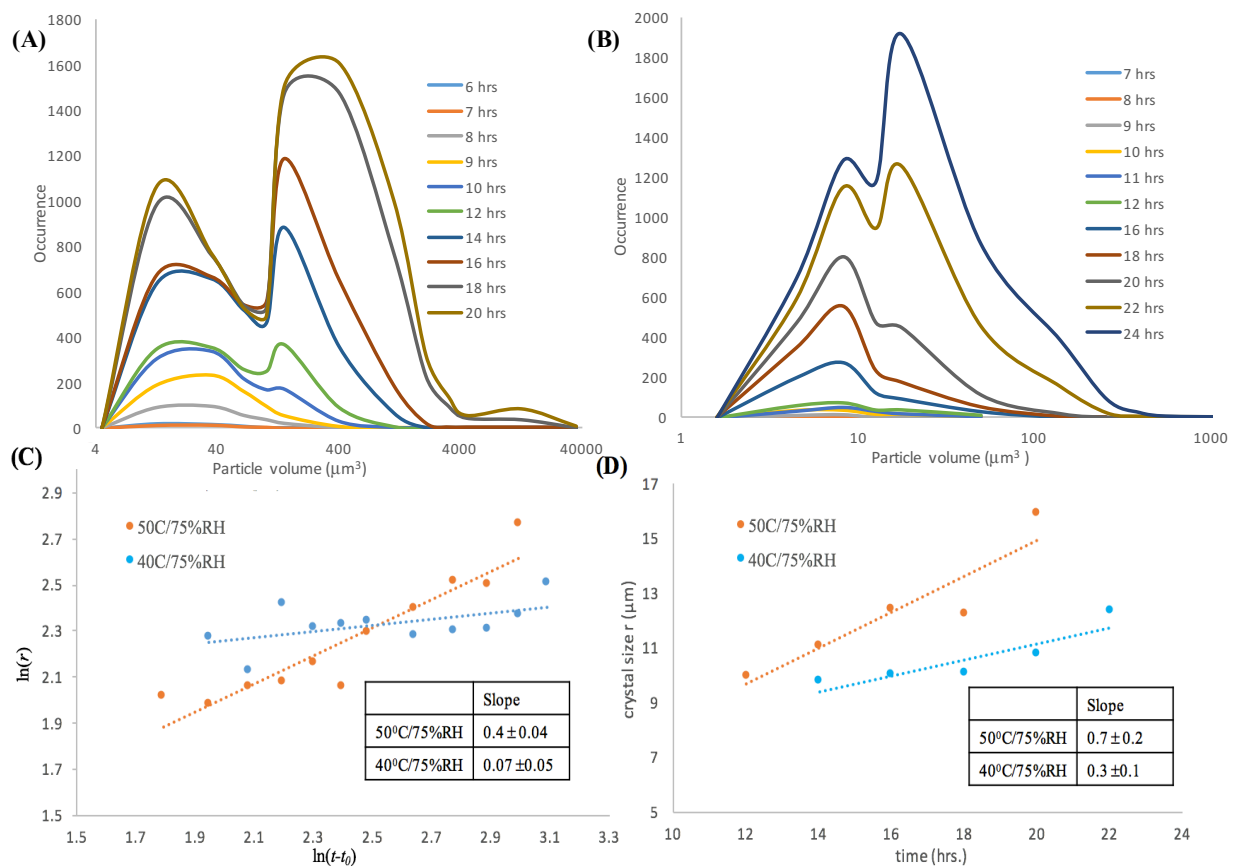


Figure 2-3 Crystal growth rate analysis

Time-dependent ritonavir crystal particle size distribution at **(A)** 50°C/75%RH and **(B)** 40°C/75%RH; **(C)** crystal growth rate depicted by $\ln(r)$ vs. $\ln(t-t_0)$ plot; **(D)** crystal growth rate for the latest five time points

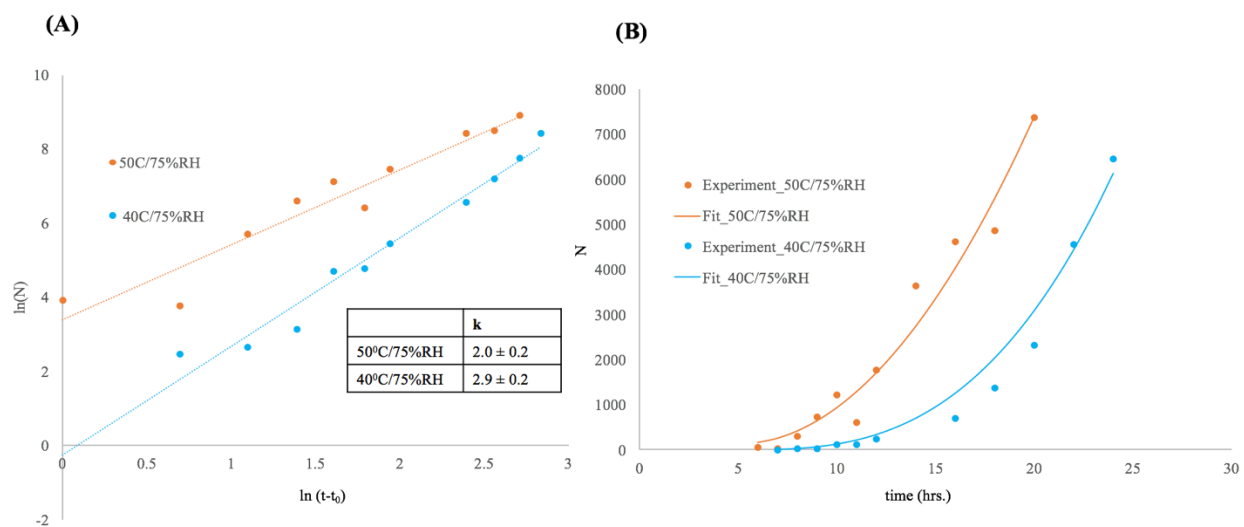


Figure 2-4 Nucleation kinetics analysis

Time-dependent the number of crystals (N) plotted logarithmically (A) and linearly (B) to determine the exponential order parameter k in Equation 2-4 and determine the nucleation rate respectively.

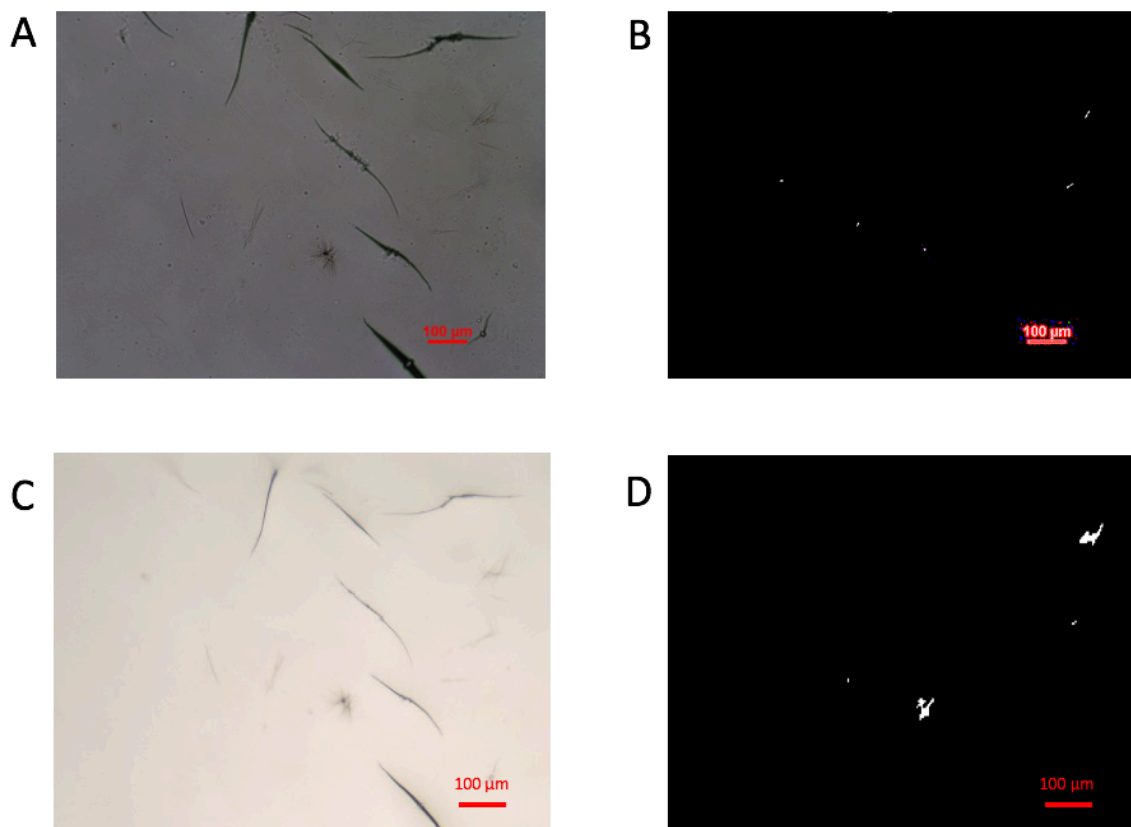


Figure 2-5 Comparison of SHG and PLM images

Ritonavir milled extrudate diluted to 5% DL stressed at 50°C/75% RH for 15h A) bright field image by PLM, B) cross polarized image by PLM, C) bright field image by SONICC, D) trans-SHG image by SONICC

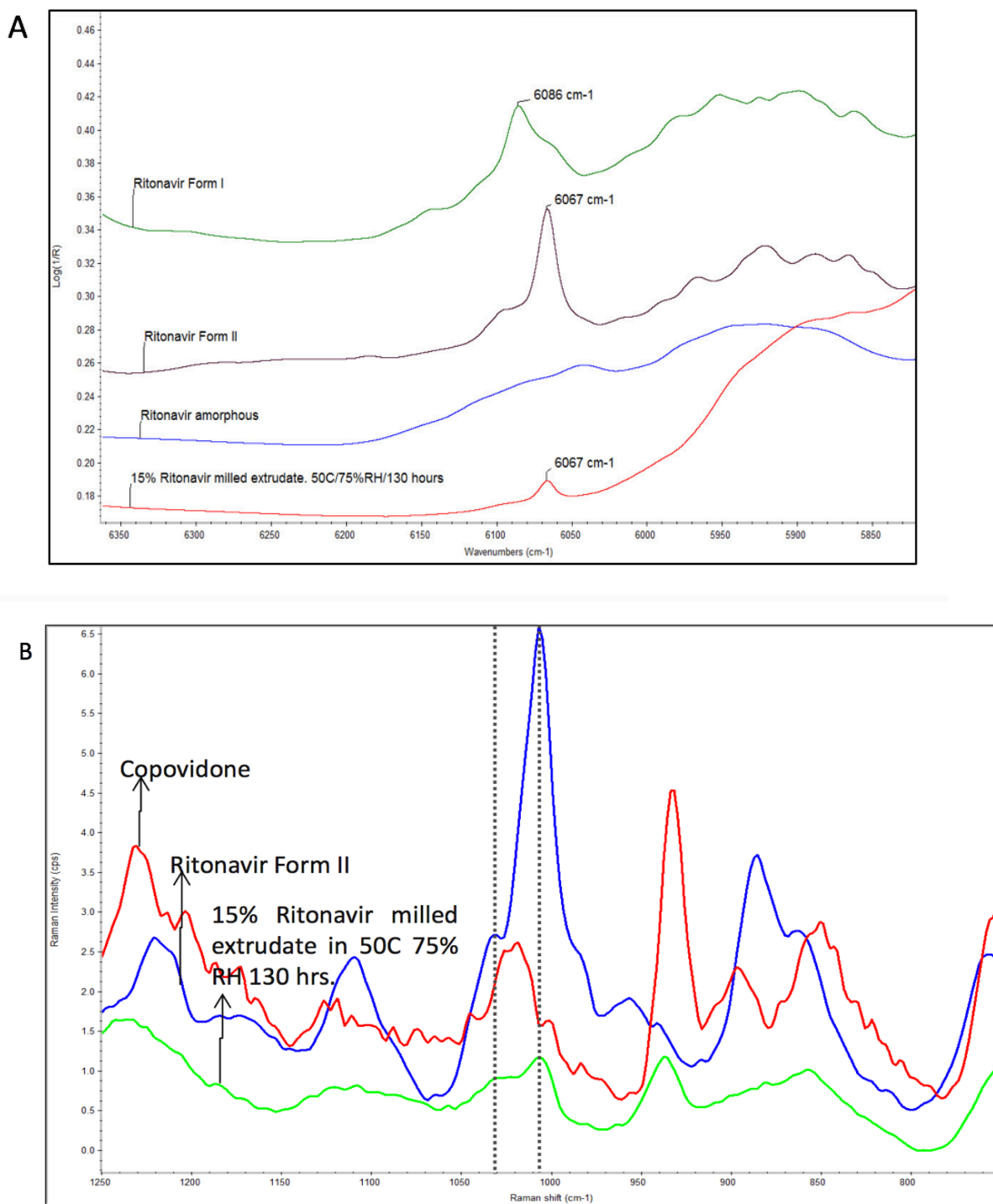


Figure 2-6 Ritonavir crystal form characterization

(A) Near IR spectra (B) Raman spectra of 15%DL ritonavir milled extrudate in 50°C/75% RH after 130 h: Both near-IR spectra and Raman spectra indicate the presence of ritonavir crystals in Form II.

Table 2-1 Parameters in JMAK model

Parameter in model	50°C/75%RH	40°C/75%RH
k	2.0 ± 0.2	2.9 ± 0.2
m	0.40 ± 0.04	0.07 ± 0.05
k + 3m	3.2 ± 0.3	3.1 ± 0.4
n	3.1 ± 0.2	2.9 ± 0.3
ln(K)	-11.6 ± 0.4	-13.4 ± 0.6

CHAPTER 3. SECOND HARMONIC GENERATION MICROSCOPY GUIDED RAMAN SPECTROSCOPY FOR PHARMACEUTICAL MATERIALS ANALYSIS

3.1 Introduction

Polymorphism, which refers to the existence of multiple crystalline solid forms of identical composition, is one of major concerns in drug formulation development. The disparity of crystal lattice structure results in different physicochemical characteristics, for example, dissolution kinetics, thermodynamic stability, etc.¹⁻⁴ Different crystal forms of API can show significantly difference on bioavailability and stability. During the research and development process of a drug product, it is important to do polymorph screening to select the polymorph with high bioavailability and stability. However, during the manufacturing process and storage of the drug, the spontaneous polymorphic transition may happen. The API will spontaneously transform into a more stable crystal form. A classic example is the case of ritonavir. In 1998, Norvir®, which is a marketed final dosage form of ritonavir, had to be recalled, due to the discovery of ritonavir form II with lower bioavailability and slower dissolution kinetics.⁵ After this case, the Food and Drug Administration (FDA) and other government agencies require thorough characterization of API polymorphism during filing for a new drug applications (NDAs) and abbreviated new drug applications (ANDAs).

A recent study estimated that more than 80% API and promising API candidates have multiple polymorphs.⁶ Clopidogrel bisulfate is a particularly intriguing case, which has seven identified crystal forms.⁷⁻⁹ Nowadays, only Form I and Form II are used for the drug formulation. Clopidogrel bisulfate is an API that falls into thienopyridine class. It inhibits platelet aggregation and is used to treat patients with acute coronary syndrome. Only the dextrorotatory enantiomer exhibits anti-platelet aggregation where the levorotatory enantiomer remains inactive.¹⁰ Therefore, the final dosage form is typically a pure enantiomeric form preparation. The clopidogrel bisulfate Form I exhibits higher bioavailability, while Form II is more thermodynamically stable.⁸ One of the most common techniques for the production of clopidogrel bisulfate is solvent mediated crystallization. In this manufacturing process, clopidogrel bisulfate will crystalize as Form I at first due to the kinetical preference. However, the metastable Form I will spontaneously transform into Form II, if the reaction is allowed to progress longer.^{9,11} Moreover, even a small fraction of

clopidogrel bisulfate Form II would have negative impact on the dissolution kinetics and overall bioavailability of final product.¹² In the manufacturing and production of clopidogrel bisulfate, it requires reliable methods to identify the early stage of Form I to Form II polymorphic transition.

Several common analytical methods have been explored for clopidogrel bisulfate polymorph characterization and quantitative analysis, including powder X-ray diffraction (PXRD), X-ray microtomography, vibrational spectroscopic technique combined with chemometrics, and solid state stress degradation studies.^{13,14} By using PXRD, Uvarov and Popov¹⁵ developed qualitative and quantitative analysis for the mixture of clopidogrel bisulfate Form I and Form II. They used both classical direct method and X-ray powder pattern decomposition to quantify the content of these two polymorphs. The limit of detection (LOD) was determined to be 1.0-1.5 wt.% in both methods. In a recent study, a synchrotron radiation X-ray computed microtomography (SR μ CT) was developed for the detection of clopidogrel bisulphate polymorphs with high selectivity and sensitivity. This technique combined a microscopic approach with image analysis to extract detailed information of morphology for quantification of trace amount of different polymorphs. In this study, the limit of detection (LOD) was also found to be 1%.¹⁷ This microscopic tool is capable of high throughput analysis for polymorph determination, which provided a fast measurement speed for a large area (2048 x 2048 pixels in 2 sec., with a pixel size of 3.7 μ m). However, since it requires synchrotron radiation source for the measurement, it is not available for online monitoring polymorphic transitions during manufacturing process. Some recent studies also developed spectroscopic methods for clopidogrel bisulfate polymorph characterization. Nemet *et al.* combined IR and Raman spectroscopy with chemometrics and quantified 2% of clopidogrel bisulfate Form II in Form I. And the limit of detection was reported as 1%.⁹ Although, the limit of detection for these reported techniques are down to ~1% LOD, none of these techniques can reach LOD into the parts per million (ppm) regime, which is relevant to kinetic modeling of stability and dissolution kinetics.

Nowadays, nonlinear optical imaging has recently emerged as a successful method in the pharmaceutical field for the sensitive detection of crystalline pharmaceutical materials.¹⁸⁻²⁸ Particularly, second harmonic generation (SHG), is a second order nonlinear optical process, in which the incoming light is converted to light of twice the frequency. The particular symmetry properties of SHG only permit this second order nonlinear optical process in non-centrosymmetric systems such as chiral crystals. SHG microscopy has been demonstrated as a powerful imaging

method for the detection and quantification of non-centrosymmetric crystals with low limit of detection (LOD). In recent years, there are a number of studies applying SHG and other nonlinear optical approach for pharmaceutical materials analysis, especially for API polymorph discrimination. Toth *et al.*¹⁹ demonstrated selective imaging of API in powder blends with common excipients by using ultraviolet SHG and two-photon excited UV fluorescence microscopy. Schmitt, *et al.*²³ developed nonlinear optical Stokes ellipsometric (NOSE) microscopy for rapid discrimination of two polymorphic forms of the small molecule d-mannitol. On the other hand, Toth, *et al.*²⁰ predicted the SHG activity of pharmaceutical relevant materials by using Ab initio model. This model was based on combining time-dependent Hartree-Fock calculations of the molecular building block with analytical theory for the predicted intensity from the lattice. Such calculations can help inform the potential appropriateness of SHG-guided analysis prior to experimental studies, and to obtain an initial estimate of the anticipated difference in SHG activity for different polymorphic forms. However, although SHG microscopy can discriminate different polymorphic forms in video rate, it cannot provide the chemical information of samples, which limits its applications in pharmaceutical materials analysis. So orthogonal techniques with rich chemical information are integrated with SHG microscopy for chemical identification.

In this study, we designed and built a SHG microscopy-guided Raman spectroscopy and a SHG microscopy-guided synchrotron powder X-ray diffraction to characterize clopidogrel bisulfate polymorphs. The system was capable of polymorphic determination of individual ~100 ng particles of clopidogrel bisulfate with the speed of ~10 ms per particle. Specifically, the combination of aligned bright field image and SHG image was used to find candidates of clopidogrel bisulfate Form II particles, which fully utilized the capability of SHG for crystal form discrimination. Then Raman spectroscopy and synchrotron X-ray diffraction were used to identify and confirm the crystal form of the candidates.

3.2 Methods

3.2.1 Sample Preparation

Pure clopidogrel bisulfate Form I and Form II were produced by Dr. Reddy's Laboratory. Both Form I and Form II were generated as white spherical particles. The average diameter of clopidogrel bisulfate spherical particles is ~25 μm , which was determined by calibrated bright field

image analysis. Samples was prepared as powdered mixture of 90% clopidogrel bisulfate Form I and 10% Form II by mass. Both of the images and spectra acquisitions were taken for powders compacted between two glass microscope slides.

3.2.2 Bright Field Image and SHG Image Acquisition

Both of the bright field image and SHG image were obtained by using a commercial SONICC (second-order nonlinear optical imaging of chiral crystals) microscope system (Formulatrix, Inc). Bright field images were acquired by a white-light source and a camera in SONICC system. An image segmentation and registration algorithm was used to identify particle locations, which will be described in detail in a subsequent section. SHG images were acquired by SONICC with the modification in-house for compatibility with powder analysis. For SHG imaging, a Fianium femtosecond laser was used as the incident source (170 fs, 1.3 W, 1060 nm, 50 MHz repetition rate). A resonant mirror (8 kHz) and a coupled galvanometer mirror are used for beam scanning to generate SHG images. SHG images were produced through a 10x objective with a 1.925 mm × 1.925 mm field of view. In this study, all of the SHG images were acquired with 150 mW laser power measured at the sample and 1s image acquisition time.

3.2.3 SHG Guide Raman Measurements

A prototype SHG-guided Raman instruments was designed and built in Purdue University, which integrated a SHG microscope and a Raman spectrometer. This SHG-guided Raman instrument is capable of acquiring Raman spectra follow the guidance of SHG image in each field of view. The schematic of the instrument is shown in Figure 3-1. There are two modalities in this instrument. One is SHG mode to collect bright field images and SHG images by using 1064 nm laser. The other is Raman mode to collect bright field images and Raman spectra by using 785 nm laser.

In SHG mode, a mode-locked fiber laser (Fianium Femtopower) operating at 50 MHz with a pulse duration of ~160 fs is used as the excitation source. The central wavelength of the laser was 1064 nm. And the average power at the sample during data acquisition was ~40 mW. Synchronized digitization (SD) approach was used for precise timing control. Laser transmittance bright field signal was detected by a photodiode (Thorlabs, PDA 10CF). SHG signal was detected by a photomultiplier tube (Hamamatsu E2924-05) and digitized synchronously with the laser using

PCIe digitizer cards (ATS-9440, AlazarTech, Pointe-Claire, QC, Canada) with the 50 MHz signal from the laser as the master clock. A 10 MHz TTL signal was generated from the digitizer cards to communicate with a resonant mirror (EOPC, SC-30). Beam scanning was achieved by use of the 4 kHz resonant scanning mirror moving along the horizontal (x) axis and a galvanometer stepping mirror (Cambridge Technology, RSX-1) moving along the vertical (y) axis to generate images with 512*512 pixels.

In Raman mode, a continuous wave laser (Toptica photonics, XTRA high power single-mode laser, 785 nm) was used as the excitation source and collected by an optical fiber of a custom-made Raman probe (InPhotonics, RPS785/24), shown in Figure 1, and re-collimated by a ½” fused silica lens. Collimated light then was taken through a pair of galvanometer mirrors (Thorlabs, GVS002-TSH25835-X) followed by two other fused silica 1” lenses in a 4f configuration to focus on the sample using a 10x objective. The average power at the sample was ~20 mW during the Raman spectrum acquisition. Raman signal from the sample was collected in epi, following the same beam path back through the same Raman probe and directed into a Raman spectrometer (Acton Research, SpectraPro-300i). There was a built-in notch filter in the probe to reject the laser line at 785 nm. In the Raman spectrometer, there was a 100 pixel x 1340 pixel CCD array for Raman signal detection, which was controlled by a vendor software (Winspec32).

Laser transmittance bright field signal in Raman mode was detected by the same photodiode in SHG mode and digitized synchronously with the laser using PCIe digitizer cards (ATS-9440, AlazarTech, Pointe-Claire, QC, Canada) with the internal clock. A digital to analog converter (DAC, National Instruments, NI 9263) coupled with a programmable USB interface (National Instruments, NI USB-9162), which was controlled by a built-in-house software programmed in MATLAB R2014a (MathWorks, Inc.), was used to drive the two galvanometer mirrors and send the trigger signal to the digitizer cards. The National Instruments (NI) box could send the continuous voltage signals to drive the two galvanometer mirrors. To achieve the beam scanning, the fast scanning mirror would take the role of resonant mirror and be driven by a ramp function at 100 Hz along the x axis. On the other hand, the NI box sent a voltage signal to drive the two mirrors to take the laser beam to the position of interest, which allowed point mapping and random access for Raman spectrum acquisition.

3.2.4 X-ray Diffraction Measurements

X-ray diffraction (XRD) measurements were conducted by using a multi-modal nonlinear optical imaging microscope integrated with synchrotron X-ray beam (GM/CA@ APS beamline 23-ID-B) at the Advanced Photon Source in Argonne National Laboratory. The details of the instrument set up were demonstrated in previous publications.^{29,30} Briefly, an ultrafast fiber laser (Fianium FemtoPower 1060nm, 50 MHz, ~160 fs pulses) was used as excitation light source for the multi-modal nonlinear microscope. The incident beam was raster scanned across the sample through a 10× objective with a numerical aperture (NA) of 0.3 (Optem, 28-21-10) with a resonant fast scanning mirror (Cambridge Technology, 1-003- 3002509) and a galvanometer slow scanning mirror (Cambridge Technology, 6210 H). Both bright field images and SHG images were collected in transmission direction. In this case, SHG images provided rapid crystal localization and centering, which can benefit subsequent X-ray diffraction measurements. An unattenuated photon flux with a photon energy of 12 keV, 5 μm diameter beam was used to generate X-ray scattering patterns from highly confined locations. XRD patterns of clopidogrel bisulfate sample were acquired with 2 s exposure time per location with another 2 s dead time between each exposure in a 4 × 4 grid.

3.2.5 Image Segmentation and Registration Algorithm

. An image segmentation algorithm was developed in MATLAB to align the bright field image and SHG image by registering between the sample spherical particles observed in bright field image and SHG image. This algorithm was based on a normalized cross correlation (NCC) template matching algorithm. The algorithm was trained by bright field and SHG images of a 1951 USAF resolution test grid. In the following step, Otsu's adaptive thresholding was applied to SHG images to create binary masks for SHG-active sample particles (shown in Figure 3-2d). Since in this case a bimodal intensity distribution was expected, Otsu's method was used to separate image into two classes, including, background and foreground. The algorithm started with an arbitrary threshold then searched for an optimal threshold that maximizes the inter-class variance.³¹ Another binary image was also created (shown in Figure 3-2c) by using the bright field image. In order to match the bright field image with SHG image dimensions, residual pixels were removed. Subtraction between the two binary masks followed by pruning the residual mask recovered the

particles that produced relatively low SHG signals (shown in Figure 3-2f). In this study, the spherical particles with low SHG activities were suspected as clopidogrel bisulfate Form II.

3.3 Results and Discussions

3.3.1 SHG Microscopy for Polymorphic Discrimination

SHG images of pure clopidogrel bisulfate Form I and Form II powders were shown in Figure 3-2. The SHG intensity was integrated over multiple z-planes with a depth of field ~ 120 μm . The integrated SHG intensity was divided by the estimated volume of an individual particle, and then multiplied with the total number of the particles in the field of view to get the averaged SHG activity per unit volume. All of the measured SHG intensity normalized to a point-source reference sample, 500 nm BaTiO₃ nanoparticles. Clopidogrel bisulfate Form I exhibits ~ 250 folds higher SHG intensity than that of Form II, shown in Figure 3-3. In the calculation, the averaged diameters of particles were recovered from the bright field image by using the image segmentation and registration algorithm. The combined mean and standard deviation in the SHG activities on per particle basis were 35 ± 9 counts/ μm^2 for clopidogrel bisulfate Form I and 0.095 ± 0.003 counts/ μm^2 for Form II. Theoretically, higher symmetry crystals may produce relatively weaker SHG activity,²⁸ which is consistent with the observed results for clopidogrel bisulfate. Clopidogrel bisulfate Form I has a monoclinic unit cell structure, which belongs to the P2₁ space group, while Form II owns an orthorhombic unit cell and belongs to P2₁2₁2₁ space group.¹⁵ Based on an assumption for normal distribution of uncertainty, individual particles can be assigned to either Form I or Form II with a statistical confidence of 99.995%, due to their significant differences in SHG activity.

In order to quantify clopidogrel bisulfate polymorphs in a mixture, bright field and SHG images were acquired for a mixture of 10% Form II and 90% Form I (w/w). The combination of bright-field and SHG micrographs was utilized to make initial classification of individual particles and assign them as candidates of either Form I or Form II. Figure 3-2 demonstrated the process of image analysis. Bright field images with high resolution and high signal to noise ratio (SNR) enabled the localization of individual particles. And then SHG images were used for initial classification based on the difference in SHG per unit volume (SHG/V) for Forms I and Form II. Since the bright field and SHG images were obtained using independent beam paths, image

segmentation and registration algorithm was employed to correct the disparities in the fields of view and align the two imaging modalities, as described in Section 3.2.5. In this algorithm, the clopidogrel bisulfate particles for both Form I and Form II were assumed as spheroidal particle morphologies with ~ 25 μm in diameter, which significantly reduced the complications resulted from particle overlapping in practical study.

3.3.2 Raman Spectroscopy for Polymorphic Determination

Raman spectroscopy was employed as one of the orthogonal analytical techniques for polymorphic identification of individual clopidogrel bisulfate particles. In this study, Raman spectroscopy made independent assessment of crystal form, following the guidance of SHG microscopy. The guidance provided by SHG microscopy was used to select particles of interest based on the SHG/V analysis. The results of SHG-guided Raman measurements are shown in Figure 3-4. Figure 3-4a) and 3-4b) correspond to the post-processed bright field image and SHG image, respectively. One of the representative Form II candidates, which are relatively dim in SHG image, is marked by a red circle, while a Form I candidate with high SHG activity is indicated by a blue circle. In order to obtain a Raman spectrum from the selected particle, a pair of galvanometer mirrors was controlled by calculated voltage to directly localize the excitation laser beam to the target position. Since spontaneous Raman scattering signal is relatively weak, each Raman spectrum was collected by integration of Raman signal for ~ 1 minute (2 seconds per frame for 30 frames) to reach high SNR. The Raman spectrum collected at the selected position (red solid line in Figure 3-4) was compared with the Form II reference spectrum (red dash line in Figure 3-4). The excellent agreement was observed, while the Form I showed the same consistency. It proves that the initial assignment made by SHG images is consistency with the determination of Raman spectroscopy. Therefore, for monitoring of clopidogrel bisulfate production, SHG microscopy enabled classification of crystal forms and selection of the Form II candidates with high speed. Then followed Raman spectroscopy at the selected location can be used to identify the existence of clopidogrel bisulfate Form II.

3.3.3 X-ray diffraction for Polymorphic Determination

In addition to the Raman spectra acquisition, SHG-guided synchrotron XRD technique also enabled for polymorph determination of clopidogrel bisulfate. It is another method to assess the

capabilities of single-particle polymorphic assessments by SHG. The experiments were conducted for the mixture of 90% clopidogrel bisulfate Form I and 10% Form II (w/w) at Argonne National Laboratory. The experimental results were shown in Figure 3-5. In Figure 3-5, Figure 3-5a) is a laser transmittance bright field image, while Figure 3-5b) and Figure 3-5c) are transmittance SHG images at the same field of view. Yellow circles marked the representative clopidogrel bisulfate particles. And the polymorphs of individual particles were classified by SHG signal measurements. To identify the polymorphs of these representative particles, a collimated X-ray beam with 5 μm in diameter, was employed for the raster scan on these particles. This 5 μm X-ray beam provided tight localization of X-ray measurements and reduction of corresponding background signals. By using narrow beam size of X-ray beam, there is a significant enhancement of the sensitivity and signal to noise ratio. Based on the assumption that it is a uniform distribution of particles orientations, integrated intensity along azimuthal angles were recovered from a set of anticipated X-ray diffraction pattern. The experimental results were compared to the theoretical predictions of monoclinic and orthorhombic unit cell from Cambridge Structural Database (CSD) for clopidogrel bisulfate Form I and Form II respectively. With the comparisons of X-ray diffraction pattern, the polymorphs of individual particles were confirmed.

3.3.4 Discussions

SHG microscopy has been demonstrated as a powerful tool for clopidogrel bisulfate polymorphic discrimination. As it showed in Figure 3-3, significant differences between Form I and Form II polymorphs are expected. In statistical analysis, SHG activity per particle basis of both forms were integrated, which suggests a discriminatory confidence of 99.995% based on SHG signal alone. However, there are several limitations of using SHG microscopy only for polymorphic discrimination. This method is only applicable to crystal forms with significant difference of crystal structures. Also, this statistical analysis assumes that the difference in SHG per unit volume is only dependent on the crystal structure. In practice, both the physical differences within the particles may affect the SHG intensity as well, including, crystal size distributions, orientation of the crystals, etc. Therefore, in this study, we coupled SHG microscopy with other orthogonal analytical methods, Raman spectroscopy and powder X-ray diffraction, to identify the polymorphism of clopidogrel bisulfate particles. With further confirmation of these orthogonal methods to provide physical, chemical and structure information, the overall rate of

misclassification can be significantly reduced. As we know, the misclassification probability of SHG microscopy is $\sim 0.005\%$, while the error from Raman spectroscopy is $\sim 0.1\%$. The misclassification probability will be 5×10^{-8} .

In the experimental results, all these three approaches, SHG microscopy, Raman spectroscopy and powder X-ray diffraction, can be employed for polymorph discrimination independently. Among these three techniques, SHG microscopy shows significant advantages compared to the other two methods. By using SHG microscopy, the discrimination of different polymorphs is based on a single scalar input, which is SHG intensity per unit volume. But Raman spectroscopy carries additional chemical and structural information from a 1D spectrum, while XRD acquires 2D diffraction patterns. Since the purpose of this study is polymorph discrimination, for Raman spectra and X-ray diffraction patterns, dimensional reduction to a single scalar value is necessary to eventually inform the crystal form. Thus, SHG microscopy is the simplest and most directed method for qualitative analysis of API polymorphs.

Another significant advantage of SHG microscopy is its measurement time. Since spontaneous Raman scattering is weak, which is $\sim 10^{-7}$ relative to Rayleigh scattering,³² spontaneous Raman spectrum acquisition requires longer integration time to obtain a spectrum with sufficient signal to noise ratio for polymorph discrimination. In this practical study, it took 60 s to acquire a Raman spectrum with sufficient signal to noise ratio. For a mixture sample with 1% clopidogrel bisulfate Form II in Form I, which consists of 900 particles, it would take ~ 15 hours for the spectral acquisitions and post processing of these Raman spectra. For synchrotron X-ray diffraction, the measurement time is much less compared to Raman spectroscopy. It takes 1 s for the integration time of individual particles. And 900 particles sample requires ~ 30 min for the data acquisition, including the dead time for data transferring and sample repositioning. However, synchrotron X-ray diffraction is difficult for routine access, due to the limited number of synchrotron facilities. Therefore, synchrotron X-ray diffraction cannot be treated as a routine technique for API polymorph determinations. On the other hand, SHG microscopy requires less than 1 second for collecting a SHG image within a 1 mm x 1 mm field of view, which includes ~ 200 clopidogrel bisulfate particles. For the mixture sample with 900 particles, it only takes a few seconds. To achieve a limit of detection (LoD) of 0.1%, it would require ~ 1 minute (40 frames with ~ 0.5 s dead time for sample repositioning between frames). And if we would like to access to a LoD of 100 ppm, it only requires ~ 10 minutes.

In each spherical particle of clopidogrel bisulfate, it consists of numerous small crystallites. Therefore, it shows relatively low variance in SHG intensity per particle. We calculated SHG activities of clopidogrel bisulfate from 100 particles in different fields of view. Form I yields 35 ± 9 counts/ μm^2 SHG signals, while Form II yields 0.095 ± 0.003 counts/ μm^2 . The relative standard deviation (RSD) of the SHG per unit volume determination for both Forms I and II was $\sim 15\%$. The SHG intensity for individual particle is the ensembled averaged SHG signal from multiple small crystallites in different orientations. For a polycrystalline conglomerate, a representative population of numerous small crystallites contributes to the overall SHG intensity observed, rather than a few relatively large sources. Since the average crystal size is much smaller than the focal volume, a statistical population of all sizes and orientations is sampled within each individual particle, which can significantly reduce the particle-to-particle variance in SHG intensity.

It is worthwhile to note that the discrimination and identification of clopidogrel bisulfate polymorphs are based on individual particles. In this case, we assume individual spherical particles can only be either pure Form I or pure Form II. One particle cannot consist of both Form I and Form II at the same time. This assumption is based on the knowledge that polymorphic transformation kinetics for intra-particle interactions are much faster than that for inter-particle interactions.^{33,34} Adjacent crystallites within single particle have intimate contact, which can result in rapid polymorphic transition throughout the particle, while inter-particle interactions are limited. Therefore, during the polymorphic transition process, after an initial nucleation of clopidogrel bisulfate Form II, there will be a fast transition to the entire particle. But it is this polymorphic transition is hard to propagate to adjacent particles. Our experimental results also showed that there is no mixture of polymorphs in individual particles, which is consistent with the assumption we made.

In this study, clopidogrel bisulfate Form II shows weak SHG activity, while amorphous clopidogrel bisulfate sample should be SHG inactive. It is challenging to discriminate Form II and amorphous materials by SHG microscopy alone, since the SHG signal of Form II is significantly weak. In this case, the integration of SHG microscopy with other orthogonal methods, like Raman spectroscopy, can be one of the best strategies for the polymorph determination.

In conclusion, SHG microscopy-guided Raman spectroscopy combines the advantages of both high speed of SHG microscopy and chemical specificity from Raman spectroscopy. This technique can be utilized for API polymorphism determination, especially for polymorphs with

large difference of SHG activities. In this study, we developed a method which is applicable to real-time monitor the existence or absence of clopidogrel bisulfate Form II in the manufacturing process. Finding Form II in a large amount of Form I seems like finding a needle in a haystack. We solved this problem by a two-step approach. First, find a needle candidate in a haystack by using techniques with short measurement time. In this case, we used SHG microscopy to find the candidates of Form II particles with low SHG activities. And then, we use a time-consuming but information-rich method, Raman spectroscopy, to confirm the candidate is a needle. Raman spectroscopy was implemented into the instrument to determine the structure of clopidogrel bisulfate Form II.

3.4 Conclusion

In this study, a prototype SHG-guided Raman instrument was developed and utilized for polymorphic determination of clopidogrel bisulfate particles. SHG guide synchrotron X-ray diffraction was also employed for this case study for measurement validations. In the first step, the combination of bright field image and SHG image was used to assign the candidate particles of clopidogrel bisulfate Form II in a large amount of Form I, since beam scanning SHG microscopy can access to the speed at ~10 ms per particle with high statistical confidence. Then the subsequent Raman spectra or X-ray diffraction patterns acquisitions are capable of identifying the polymorph of individual particle. As a result, quantification of polymorphic phase content becomes straight forward due to no requirements for a calibration curve. SHG-guided Raman spectroscopy and X-ray diffraction combines the time-saving nature of beam scanning microscopy with the information-rich features of Raman and X-ray measurements. This study is applicable to real-time monitor the existence/absence of clopidogrel bisulfate Form II and the polymorphic purity of Form I during synthesis and crystallization pipeline, which has potential to improve the overall yield of Form I.

3.5 References

1. Aaltonen, J.; Allesø, M.; Mirza, S.; Koradia, V.; Gordon, K. C.; Rantanen, J. *Eur J Pharm Biopharm* 2009, 71, 23-37.
2. Chieng, N.; Rades, T.; Aaltonen, J. *J Pharm Biomed Anal* 2011, 55, 618-644.

3. Singhal, D.; Curatolo, W. *Adv Drug Deliv Rev* 2004, 56, 335-347.
4. Snider, D. A.; Addicks, W.; Owens, W. *Adv Drug Deliv Rev* 2004, 56, 391-395.
5. Bauer, J.; Spanton, S.; Henry, R.; Quick, J.; Dziki, W.; Porter, W.; Morris, J. *Pharm Res* 2001, 18, 859--866.
6. Chieng, N.; Rades, T.; Aaltonen, J. *J Pharm Biomed Anal* 2011, 55, 618-644.
7. Bousquet, A.; Castro, B.; Saint-Germain, J.; US Patent 06429210, 2002.
8. Lu, J.; Wang, J.; Rohani, S. *Cryst Res Technol* 2012, 47, 505-510.
9. Nemet, Z.; Demeter, A.; Pokol, G. *J Pharm Biomed Anal* 2009, 49, 32-41.
10. Badorc, A.; Frehel, D.; EP Patent 281,459, 1988.
11. Koradia, V.; Chawla, G.; Bansal, A. K. *Acta pharmaceutica* 2004, 54, 193-204.
12. Fahr, A.; Liu, X. *Expert Opin Drug Delivery* 2007, 4, 403-416.
13. Raw, A. *Adv Drug Delivery Rev* 2004, 56, 235-236.
14. Raw, A. S.; Furness, M. S.; Gill, D. S.; Adams, R. C.; Holcombe, F. O., Jr.; Yu, L. X. *Adv Drug Deliv Rev* 2004, 56, 397-414.
15. Uvarov, V.; Popov, I. *J Pharm Biomed Anal* 2008, 46, 676-682.
16. Rajjada, D. K.; Prasad, B.; Paudel, A.; Shah, R. P.; Singh, S. *J Pharm Biomed Anal* 2010, 52, 332-344.
17. Yin, X. Z.; Xiao, T. Q.; Nangia, A.; Yang, S.; Lu, X. L.; Li, H. Y.; Shao, Q.; He, Y.; York, P.; Zhang, J. W. *Sci Rep* 2016, 6, 24763.
18. Wanapun, D.; Kestur, U. S.; Kissick, D. J.; Simpson, G. J.; Taylor, L. S. *Anal Chem* 2010, 82, 5425-5432.
19. Toth, S.; Madden, J.; Taylor, L.; Marsac, P.; Simpson, G. *Anal Chem* 2012, 84, 5869-5875.
20. Toth, S. J.; Schmitt, P. D.; Snyder, G. R.; Trasi, N. S.; Sullivan, S. Z.; George, I. A.; Taylor, L. S.; Simpson, G. J. *Cryst Growth Des* 2015, 15, 581-586.
21. Chowdhury, A. U.; Dettmar, C. M.; Sullivan, S. Z.; Zhang, S.; Jacobs, K. T.; Kissick, D. J.; Maltais, T.; Hedderich, H. G.; Bishop, P. A.; Simpson, G. J. *J Am Chem Soc* 2014, 136, 2404-2412.
22. Hall, V. J.; Simpson, G. J. *J Am Chem Soc* 2010, 132, 13598-13599.

23. Schmitt, P. D.; DeWalt, E. L.; Dow, X. Y.; Simpson, G. J. *Anal Chem* 2016, 88(11), 5760-5768.
24. Newman, J. A.; Schmitt, P. D.; Toth, S. J.; Deng, F.; Zhang, S.; Simpson, G. J. *Anal Chem* 2015, 87(21), 10950-10955.
25. Chowdhury, A. U.; Zhang, S.; Simpson, G. J. *Anal Chem* 2016, 88(7), 3853-3863.
26. Wu, L.; Vogt, F. G. *J Pharm Biomed Anal* 2012, 69, 133-147.
27. Simpson, G. J. *Nonlinear Optical Polarization Analysis in Chemistry and Biology*; Cambridge University Press, New York, 2017.
28. Hauptert, L. M.; DeWalt, E. L.; Simpson, G. J. *Acta Crystallogr, Sect D: Biol Crystallogr* 2012, 68, 1513-1521.
29. Madden, J. T.; Toth, S. J.; Dettmar, C. M.; Newman, J. A.; Oglesbee, R. A.; Hedderich, H. G.; Everly, R.; Becker, M.; Ronau, J. A.; Buchanan, S. K. *J Synchrotron Radiat* 2013, 20, 531-540.
30. Newman, J. A.; Zhang, S.; Sullivan, S. Z.; Dow, X. Y.; Becker, M.; Sheedlo, M. J.; Stepanov, S.; Carlsen, M. S.; Everly, R. M.; Das, C. *J Synchrotron Radiat* 2016, 23, 959-965.
31. Otsu, N. *Automatica* 1975, 11, 23-27.
32. Harris, D. C.; Bertolucci, M. D. *Symmetry and spectroscopy: an introduction to vibrational and electronic spectroscopy*; Courier Corporation, New York, 1978.
33. Cardew, P.; Davey, R. *Proc R Soc London A* 1985, 398, 415-428.
34. Parrinello, M.; Rahman, A. *J Appl Phys (Melville, NY, U. S.)* 1981, 52, 7182-7190.

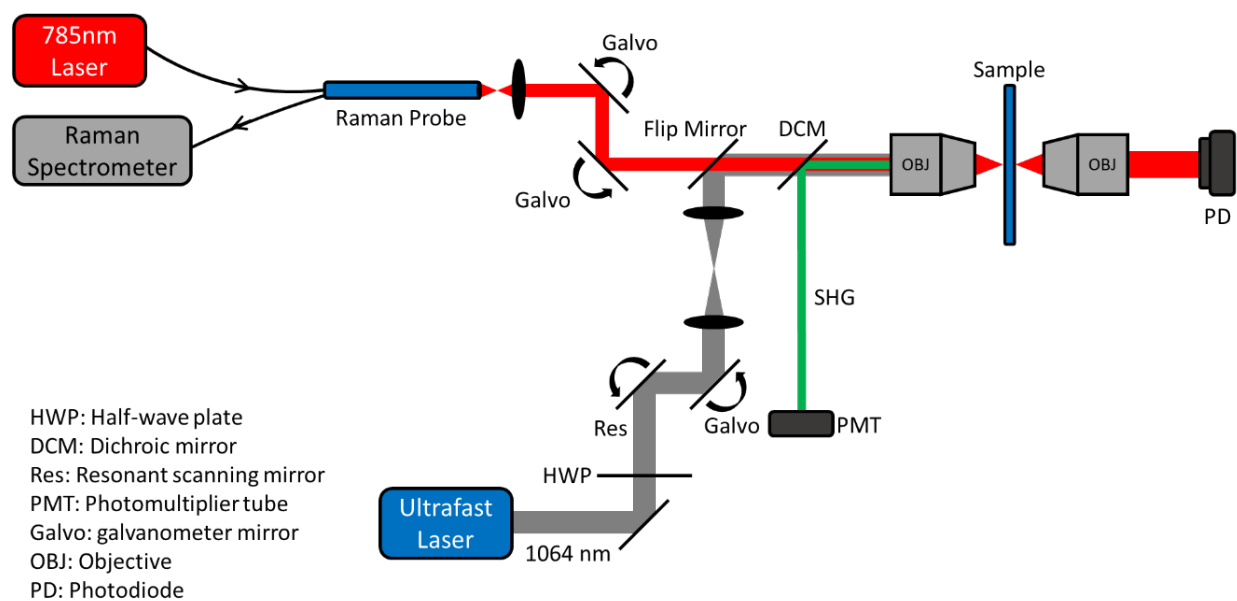


Figure 3-1 Schematic diagram of the prototype instrument of SHG microscopy-guided Raman spectroscopy

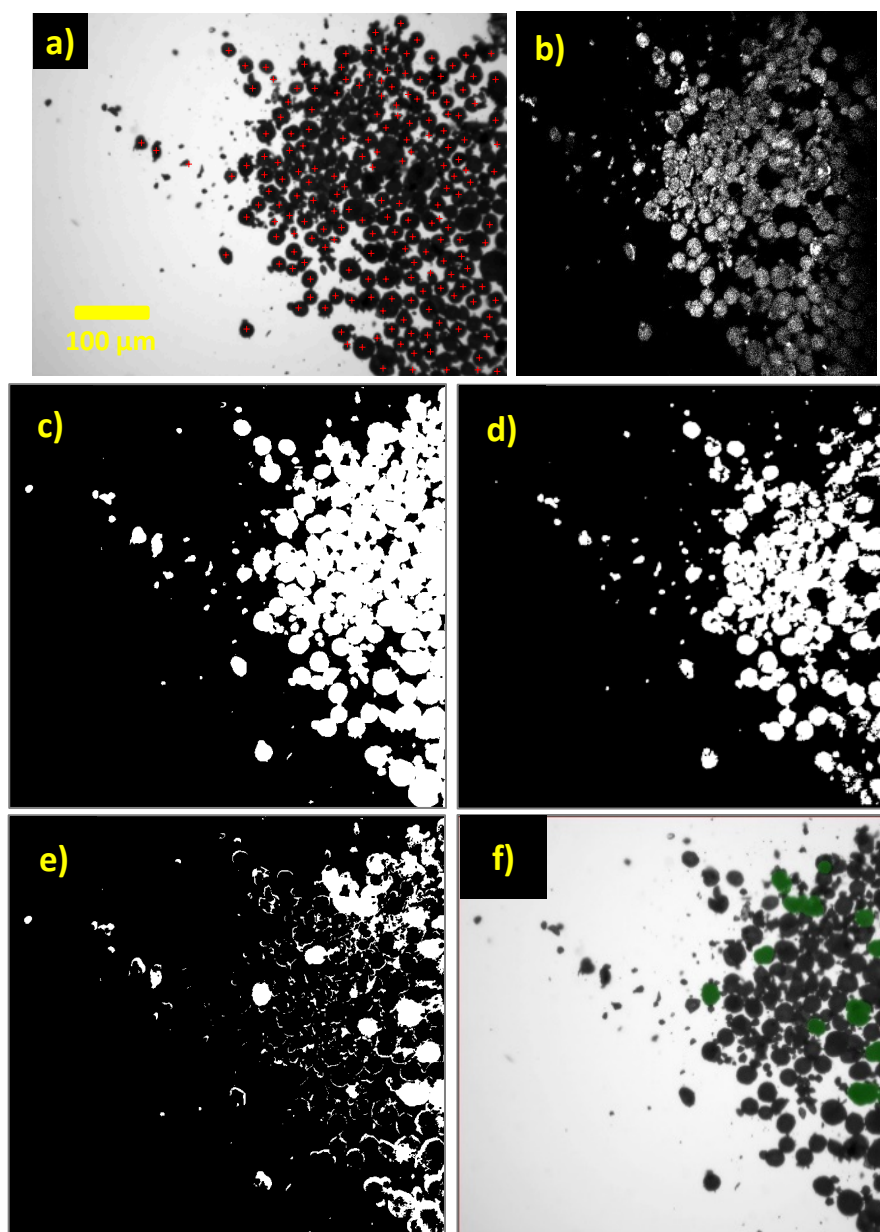


Figure 3-2 Segmentation algorithm to perform classification of individual particles. (a) Bright field image and (b) SHG image are shown for a mixture of clopidogrel bisulfate (10% Form II / 90% Form I). Red cross-hairs in the image indicate the representative candidates for the polymorphic form classification. The images in a) and b) were brought into registry and converted to binary images c) and d) respectively to identify the locations of all the particles, and the locations of the SHG-dim particles. The difference map shown in e) allows classification of the Form II particles, indicated by the green circles in Figure f).

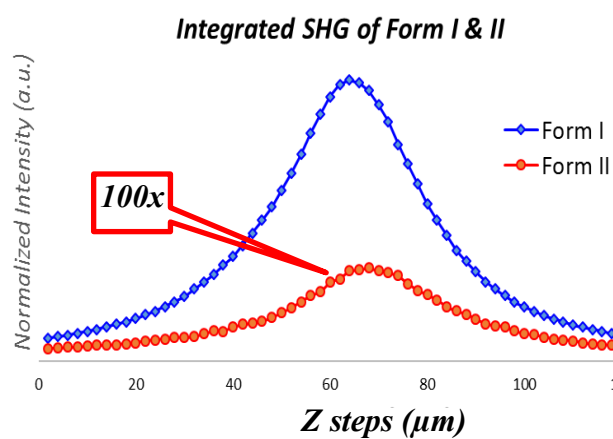


Figure 3-3 Integrated SHG intensity of clopidogrel bisulfate Form I and Form II. Measurement at focal plane was translated through powders of clopidogrel bisulfate Form I and Form II samples. The integrated SHG intensity from Form II was rescaled by 100-fold to aid in visualization. Outliers (bright SHG puncta in Form II) were excluded in this calculation.

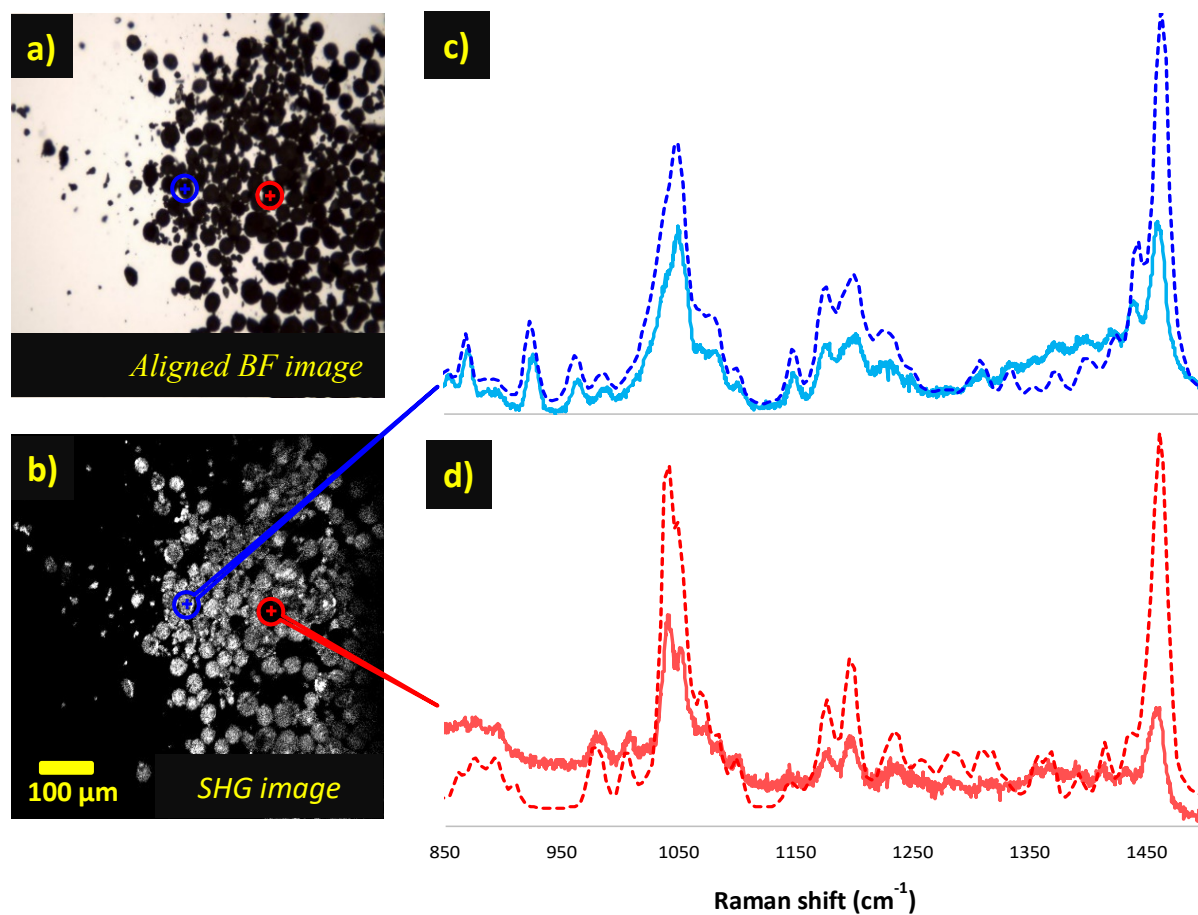


Figure 3-4 Polymorph determination of clopidogrel bisulfate by SHG-guided Raman analysis on a per-particle basis.

Figure a) and b) correspond to bright field and SHG images of a 10% mixture of Form II in Form I, respectively. Figure c) and d) correspond to single particle Raman spectrum (solid line) and FT-Raman spectrum (dash line) of Form I (blue) and Form II (red), respectively. FT-Raman spectra of both Forms are shifted few wavenumbers to the right to match the spectra feature collected from single particle measurements. In both cases Raman spectra support the preliminary classifications made by SHG microscopy.

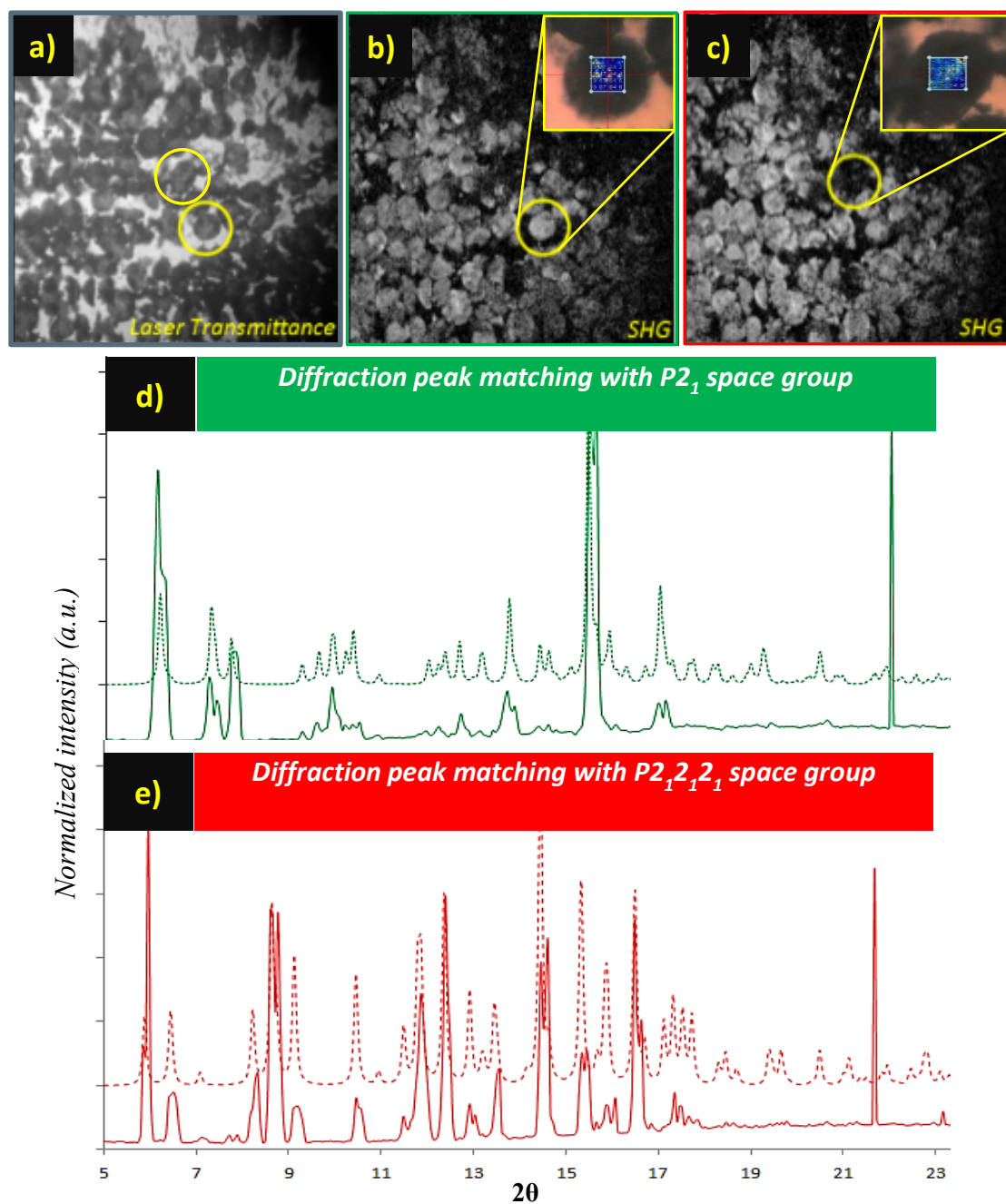


Figure 3-5 Polymorph determination of clopidogrel bisulfate by SHG-guided synchrotron XRD measurement.

Figure a) corresponds to the bright field image of the mixture, and Figure b) and c) corresponds to the SHG image of the same FOV. The yellow circles indicate SHG-bright and SHG-dim particles selected as candidates for the diffraction measurements. Experimental powder diffraction patterns (solid line) from those particles are compared to the theoretical prediction (dash line) for Form I (green) and Form II (red) in Figure d) and e) respectively.

CHAPTER 4. ACCELERATING CONFOCAL RAMAN MICROSCOPY BY DYNAMIC SPARSE SAMPLING

4.1 Introduction

Raman microscopy is a combination of Raman spectroscopy and optical imaging, which is a powerful technique to acquire detailed chemical information in multiple dimensions, including spatial domain and spectral domain¹. Raman microscopy also show great advantages of high chemical specificity and requirement for minimal sample preparation. Nowadays, Raman imaging has broad applications in both chemical and biological sample analysis, including the pharmaceutical materials characterization²⁻⁵, characterization of semiconductors^{6,7}, cancer diagnosis⁸⁻¹⁰, and forensic analysis^{11,12}.

Specifically, for polymorphic characterization of active pharmaceutical ingredients (APIs), spontaneous Raman spectroscopy and microscopy have been established as a standard method^{2,13} in both academia and industry. Different polymorphs show differences in crystal lattice structure, which can significantly impact their chemical and physical properties. Two polymorphs of an individual API might exhibit significant difference in bioavailability, stability, apparent solubility, and morphology. Previous studies show that more than 80% of APIs have multiple polymorphic forms¹⁴. Therefore, polymorphic characterization plays an important role in the development of pharmaceutical formulations, especially the high throughput screening of drug pre-formulation. There is an increasing demand for reliable analytical techniques with high speed for high-throughput API polymorphic characterization.

Although spontaneous Raman spectra provide rich chemical information, the spontaneous Raman cross section is weak (on the order of 10^{-30} cm²/sr)¹⁵. The weak spontaneous Raman signal results in a requirements of relatively long integration time to obtain sufficient signal to noise. The long measurement time limits the applications of spontaneous Raman spectroscopy and microscopy¹⁶, especially for the high throughput Raman imaging.

In previous study, several techniques have been explored to reduce the measurement time in Raman imaging. Stimulated Raman scattering (SRS)¹⁷ and coherent anti-stokes Raman scattering (CARS)¹⁸ are two great tools to significantly reduce the exposure time and improve the speed of Raman imaging. Both of these two techniques can reach up to video-rate frame rates. However, it is challenging to recover complete high-resolution spectra at each location by SRS

and CARS⁸. Moreover, the light sources of both SRS and CARS have to be ultrafast laser sources, which is expensive and hard for maintenance. The requirements of ultrafast laser and complicated instrument set-up limit the application of SRS and CARS.

On the other hand, there are several illumination strategies applied to improve the speed of spontaneous Raman imaging. The illumination strategies for Raman imaging can be mainly classified into three classes, including wide-field illumination, line illumination, and confocal point scanning¹⁹. For wide-field Raman microscopy, the entire field of view is illuminated, and the Raman spectrum is collected by serially scanning through discrete frequency. In previous study, several techniques, such as, acousto-optic tunable filters, liquid-crystal tunable filters (LCTFs), fiber array assemblies, and integrated light sheet illumination, were incorporated to wide-field Raman imaging. These approaches can improve the signal to noise ratio and the efficiency of spatial and spectral collections²⁰. Thus, wide-field Raman microscopy is capable of recovering spatial information with high efficiency. However, since it illuminates the entire field of view, the intensity of light source at each individual pixel is reduced, which inhibits the corresponding spontaneous Raman signal proportionally. For line-illumination Raman microscopy, a hemicylindrical lens and an array detector were employed to acquire full Raman spectra in one dimension and spatial information on the orthogonal axis. There are two scanning methods applied in line-illumination Raman microscopy: sweeping a line of illumination across the sample or translating the sample in one axis. In both cases, the Raman image is produced one line at one time.²¹ However, line-illumination Raman imaging has similar issues as wide-field strategies. Both of them suffer from low intensity at each individual pixel, which results in relatively longer measurement time.

Compared to wide-field and line-illumination, point scanning Raman imaging has the distinct advantage of confocal sectioning, which dramatically reduce background and interference from sample out of the focal plane. For conventional point scanning Raman imaging, raster scanning was used to sample all pixels in the field of view, which is able to collect all of the Raman information pixel by pixel. But raster scanning also results in a significant long Raman image acquisition time, which limits a lot of practical applications. In raster scanning, the next sample location is always the adjacent pixel. Since the adjacent pixels are spatially and spectrally correlated, the next pixel in raster scanning strategy is among the least informative pixels.

In order to accelerated point scanning Raman imaging, one strategy is selective sampling, which can efficiently reduce the numbers of sampling points. In previous study, several selective sampling algorithms have been employed to predict the optimal measurement locations and then reconstruct the Raman image. Rowlands *et al.*^{22,23} developed a sparse sampling algorithm to determine the next information-rich sampling location by assigning a score to each unmeasured pixel dynamically. By using two different interpolation algorithms: a cubic spline and a Kriging interpolation, the score was calculated as the difference between the interpolated values for a pixel. The pixel location where the reconstruction algorithms differed the most was treated as the most informative pixel and then measured. Due to the integration of interpolation algorithms, this method showed an improvement of efficiency compared with random sampling. However, from a fundamental perspective, it is not clear that the location where the difference is largest with two interpolation approaches corresponds to the most informative pixel. Utilizing information collected by another much faster orthogonal imaging tool is an effective approach for selective sampling as well. Chowdhury, *et al.*²⁴ integrated second harmonic generation (SHG) microscopy with spontaneous Raman spectroscopy to selectively decide the sample positions for Raman spectral acquisition. Due to the high speed of SHG microscopy, it significantly reduced the measurement time. However, SHG-guided Raman spectroscopy is only applicable for sample systems whose components are symmetry-allowed for SHG, which limits some practical applications. Kong, *et al.*²⁵ combine the confocal fluorescence microscopy with Raman microscopy for selective sampling and time reduction. But it added significant complexity to the instrument and also had specific requirements for the samples.

In this study, a supervised learning approach for dynamic sampling (SLADS) is demonstrated for accelerating confocal spontaneous Raman imaging, which allows rapid determination of optimal sampling locations in real-time during image acquisition. SLADS is the first time to use a machine learning approach that incorporates training data for sample selection, which is different from previous study for sparse sampling Raman imaging. The stopping condition was determined by training data to optimize the number of sampling points and the quality of reconstructed image.²⁶ By using this approach, chemical images of pharmaceutical materials can be acquired with >99.5% accuracy from 15.8% sampling, representing a ~6-fold reduction in measurement time compared to raster scanning Raman images.

4.2 Theory

4.2.1 Dynamic Sparse Sampling Algorithm

SLADS, as a supervised learning approach for dynamic sampling, has been demonstrated as a method to identify a sparse set of sampling locations to improve the efficiency of sparse sampling and reconstruction of the underlying object.^{26,28,29} The theoretical framework of SLADS is described in this section. Since SLADS is a supervised learning approach, it requires to measure 1% of sampling locations as initial inputs. Assuming the previously measured k locations, $S = \{s^{(1)}, s^{(2)}, \dots, s^{(k)}\}$, of some sample, $X \in \mathbb{R}^N$, the next location will be $s^{(k+1)}$ to measure. The measurements locations and results can be described by a matrix, shown in equation 4-1.

$$Y^{(k)} = \begin{pmatrix} s^{(1)}, X_{s^{(1)}} \\ \vdots \\ s^{(k)}, X_{s^{(k)}} \end{pmatrix}. \quad (4-1)$$

In sparse sampling method, image reconstruction was performed to obtain $\hat{X}^{(k)} \in \mathbb{R}^N$, by using the measurement results. The goal of SLADS is to find the most informative pixel location, which can maximize the expected reduction in distortion (ERD). Equation 4-2 shows how to find the next measurement location s by calculating ERD of the all unmeasured pixel locations.

$$s^{(k+1)} = \arg \max_{s \in \{\Omega \setminus S\}} \{E[R^{(k;s)}|Y^{(k)}]\}. \quad (4-2)$$

In Equation 4-2, Ω is the set of all pixel locations in X . The reduction in distortion R resulting from measuring pixel s is calculated by the following expression in Equation 4-3.

$$R^{(k;s)} = D(X, \hat{X}^{(k)}) - D(X, \hat{X}^{(k;s)}). \quad (4-3)$$

In Equation 4-3, $\hat{X}^{(k;s)}$ is the reconstruction made with $Y^{(k)}$ and X_s , and $D(A, B)$ is the distortion between two images A and B . In this implementation of SLADS, the distortion D between two images A and B is defined as,

$$D(A, B) = \sum_{i=1}^N I(A_i, B_i). \quad (4-4)$$

I is an indicator function demonstrated in Equation 4-5. A_i is the i^{th} element of the image A . However, for Raman microscopy, a spectrum is obtained from each pixel location. Thus, we have an l -dimensional vector at each pixel location. To implement SLADS to Raman microscopy, we used the classification method described in section 4.2.3 to label each spectrum.

$$I(A_i, B_i) = \begin{cases} 0 & \text{if } A_i = B_i \\ 1 & \text{if } A_i \neq B_i \end{cases} \quad (4-5)$$

In SLADS, since the ground truth is unknown, it is assumed that the expectation value for the reduction in distortion can be written as a function of Y . In Equation 4-6, the function $f_\theta^s(Y)$ is generated by using a supervised learning approach, where θ is a parameter vector.

$$E[R^{(k;s)}|Y^{(k)}] = f_\theta^s(Y). \quad (4-6)$$

4.2.2 Stopping Condition of SLADS

Since SLADS is a supervised learning approach, training set was used to help to identify the stopping condition of SLADS. The SLADS framework includes a stopping condition that allows us to stop sampling when the expected total distortion (ETD) is smaller than a threshold T ;

26

$$ETD_k = E \left[\frac{1}{|\Omega|} D(X, \hat{X}^{(k)}) \right] < T. \quad (4-7)$$

Since this quantity cannot be computed without foreknowledge of the ground truth image, another function $\epsilon^{(k)}$, is used in SLADS instead to identify the stopping condition.

$$\epsilon^{(k)} = (1 - \beta)\epsilon^{(k-1)} + \beta D(X_{s^{(k)}}, \hat{X}_{s^{(k)}}^{(k-1)}). \quad (4-8)$$

Here, $k > 1$, β is a user selected parameter that determines the amount of temporal smoothing, $X_{s^{(k)}}$ is the measured value of the pixel at step k , and $\hat{X}_{s^{(k)}}^{(k-1)}$ is the reconstructed value of the same pixel at step $k - 1$. The threshold to place on this function, $\tilde{T}(T)$, to stop sampling when ETD_k is below T , is computed as follows.

First, M training images are measured using the SLADS algorithm, and stopped when the total distortion, is below the desired threshold T .

$$TD_k = \frac{1}{|\Omega|} D(X, \hat{X}^{(k)}) < T \quad (4-9)$$

Then the value of $\epsilon^{(K_m)}$ for each experiment is recorded. Here $\epsilon^{(K_m)}$ is the value of $\epsilon^{(k)}$ when SLADS is stopped for the m^{th} image. Then the threshold to place on $\epsilon^{(k)}$ in the SLADS experiment is computed as,

$$\tilde{T}(T) = \sum_{m=1}^M \epsilon^{(K_m(T))}. \quad (4-10)$$

4.2.3 Classification of Raman Spectra

As it demonstrated in section 4.2.1, SLADS algorithm can be implemented to discrete valued images. Therefore, in this application, classification of acquired Raman spectra was employed to identify the chemical composition of the sample measured at specific locations. The Raman spectroscopic image was then converted to a discrete valued image, in which the value of each pixel is its corresponding class label, to inform the SLADS algorithm. In this study, classification of Raman spectrum was obtained by combining two supervised learning algorithms: linear discriminant analysis (LDA) and support vector machine (SVM). LDA was performed for initial dimensional reduction. LDA is a generalization of Fisher linear discriminant, which constructs the $N-1$ dimension space for N classes of data to maximize the resolution between classes. Since there are three classes in this case, the Raman spectrum with thousands of elements will be converted into a 2D space. After dimensional reduction, SVM was conducted for classification by constructing optimal hyperplanes in data space (2D space in this case) to separate different clusters of data points. SVM, as a machine learning algorithm, has broad applications for classification problems. Specifically, for linearly inseparable data, SVM is capable of drawing nonlinear decision boundaries by using pre-defined kernel function. It is a more computationally economical equivalent of projecting data into a higher dimensional space. However, SVM is inherently designed to draw the boundary between two classes and work with two-class problems. In this study, in order to classify Raman spectra into N classes with $N > 2$, a 1-vs-1 SVM approach was adopted: one decision boundary was made for each pair of classes, generating $\binom{n}{2}$ decision boundaries. Classification of individual Raman spectrum is achieved using the following procedure²⁷: all the $\binom{n}{2}$ decision boundaries were applied to the unseen data point, and each decision boundary returns one prediction for a class label. Then a polling procedure is conducted, in which the class that obtains the highest number of prediction votes is used as the classification result. If the polling results in a tie, a tie-breaking algorithm is implemented to make a final classification decision.

4.3 Experimental Methods

4.3.1 Sample Preparation

Pure clopidogrel bisulfate Form I and Form II were produced in-house at Dr. Reddy's Laboratories. Both the Form I and Form II particles were spherical with similar particle size distributions (diameter: $\sim 25 \mu\text{m}$). The sample prepared for Raman microscopy was a mixture of clopidogrel bisulfate Form I and Form II, which consisted of 50% Form I and 50% Form II by mass. The powder sample was placed on a fused quartz microscope slide to collect Raman spectrum.

4.3.2 Raman Spectrum Acquisition

Figure 4-1 is the schematic diagram of a confocal Raman microscope coupled with SLADS algorithm. A continuous wave diode laser (Toptica, 785nm wavelength) was utilized as excitation laser. The laser was coupled into a Raman probe (InPhotonics, RPS785/24), and then collimated by a $\frac{1}{2}$ inch fused silica lens. The collimated light was directed through a scan head, which is a pair of galvanometer scanning mirrors. Additionally, two 1-inch diameter fused silica lenses formed a $4f$ configuration to deliver a collimated beam to the back of a 10x objective (Nikon) and then to the sample. A photodiode was set on the transmitted direction to collect the laser transmittance signal for bright field imaging. The Raman signal from the sample was collected in epi direction and sent back through the same beam path into the Raman probe. There was a notch filter (785/24) built in the Raman probe to reject the excitation laser at 785 nm. Raman spectra were obtained by an Acton SP-300i spectrometer with a 100 x 1340 CCD array. The Raman spectra acquisitions were controlled by a vendor software, WinSpec32.

In order to instantly relocate the excitation laser beam, these two galvanometer scanning mirrors (one for x-axis position, the other for y-axis position) were controlled by a digital to analog converter (DAC, NI 9263, National Instruments) coupled with a programmable USB interface (NI USB-9162, National Instruments). MATLAB R2014a (MathWorks, Inc.) software written in-house was used to output analog voltages to the galvanometer mirrors and direct the laser beam to the desired locations. However, MATLAB R2014a requires to be run with operation system win 8 or higher, while the vendor software WinSpec 32 has to be run on an individual computer with win XP. Therefore, network communication programs based on WinSock application programming interface were designed (a client/server network) in house using Visual C++ 6.0

(Microsoft Corporation) in combination with MATLAB to allow remote control of the Raman spectrometer vendor computer (server computer) as well as data transfer between the two computers. This network communication programs realize the automation of Raman spectra collection and the implementation of SLADS into Raman microscopy. The communications between the client computer and server computer were shown in Figure 4-1. During the experimental process, the client computer used the SLADS algorithm (coded in MATLAB) to determine the next measurement location. Then the client computer calculated the corresponding voltages required for the galvanometer mirrors, and the DAC drove the pair of galvanometer mirrors to direct the laser to the measurement location. After these steps, the client computer sent a request to the server computer for Raman spectrum acquisition. The acquired Raman spectrum file from the server computer was then sent back to the client computer for identification this measurement point and continuous Raman spectrum acquisition at the selected measurement points by running SLADS algorithm.

4.3.3 Ground Truth Raman Image Acquisition

A 128 pixels \times 128 pixels ground truth Raman image were acquired by using a raster scan sampling pattern. Raman spectra of the 50%/50% (w/w) clopidogrel bisulfate Form I/Form II were collected at every pixel in the field of view. The laser power measured at the sample place was \sim 30 mW. The exposure time was 0.5 s per spectral frame. To achieve higher signal to noise ratio for high quality training data for classification, 30 consecutive frames were averaged for each pixel. The ground truth Raman spectral set were used as the training data of classification algorithms. Furthermore, the ground truth Raman image was used to simulate the process of dynamic sparse sampling Raman imaging and evaluate the performance of SLADS algorithm compared with other sparse sampling algorithm, such as, random sampling.

4.3.4 Classification of Raman Spectra

The classification algorithms were conducted to convert Raman spectra into a discrete value. The basic theory of using machine learning algorithms for Raman spectral was demonstrated in section 4.2.3. Before implementing LDA and SVM, a set of pre-processing steps for Raman spectra were performed, shown in Figure 4-2. First, a Savitzky-Golay filter was applied to smooth the spectra³⁰. And then a rolling ball filter was used to remove the

fluorescence background³¹. Finally, the spectra were normalized to their integrated intensities. The integrated intensity information of every spectrum was recorded, so that it can be retrieved when intensity information within each spectrum was required for subsequent analysis.

After the pretreatment of Raman spectra, LDA and SVM were employed subsequently. Since both of LDA and SVM are supervised learning algorithms, 500 Raman spectra was treated as training set, which were randomly picked up from the 16,384 Raman spectra in ground truth acquisition. These 500 Raman spectra were manually classified into clopidogrel bisulfate Form I, Form II, and background by human inspection, based on specific Raman peaks. If a random selected spectrum was ambiguous for manual classification, it was excluded from training set. For example, the Raman spectrum collected at the boundary between clopidogrel bisulfate Form I and Form II particles, may exhibit spectral features of both polymorphs. It is not appropriate to use ambiguous Raman spectra as training data. Then LDA was performed to reduce the dimension of Raman spectra in training set. The Raman spectrum with thousands of elements was projected onto a two-dimensional space formed by two LDA axes. After dimensional reduction, SVM algorithm with a Gaussian kernel was employed to define the decision boundaries for Raman spectra of three different classes. To optimize the parameters in SVM, a five-fold cross-validation was performed. This set of cross validations in training process improved the robustness of the classification method. The constructed decision boundaries in the two-dimensional space was shown in Figure 4-3(a), with all 500 training data points overlaid.

The constructed classifiers from training was able to applied to discriminate Raman spectra of clopidogrel bisulfate Form I, Form II, and background. Since the 1-vs-1 SVM polling process was used for the classification, a tie in votes may happen, especially for the Raman spectra collected at the location of a mixture. Specifically, in this study, there are 30 spectra out of 16,384 achieving a tie in votes. A simplified tie-breaking algorithm was implemented that all voting ties are labeled as clopidogrel bisulfate Form I. Figure 4-3(b) shows all 16,384 data points overlaid in the two-dimensional space by using the constructed decision boundaries. Color-shaded regions labeled the corresponding classified areas. With the established classifier, the confocal Raman spectral image was converted into a discrete valued image with 128 x 128 pixels. Each pixel was classified and valued as 1, 2, and 3, which correspond to clopidogrel bisulfate Form I, Form II and background, respectively. The discrete valued ground truth image is shown in Figure 4-5(g).

4.3.5 Stopping Condition of SLADS

As it mentioned in section 4.2.5, a set of training images was for stopping conditions of SLADS. In this study, training data were prepared by processing bright field images and SHG images in combination with bright field images acquired with confocal Raman microscope. As demonstrated in previous work,²⁴ SHG provides an independent method of determining particle polymorphism with high confidence.

Training images were constructed by the following steps. First, individual particles of clopidogrel bisulfate polymorphs Form I (bright in SHG image) and Form II (relatively dim in SHG image) were manually identified and marked. Correlation of the fields of view (FOVs) for both BF and SHG was accomplished by cropping and resizing the BF images. Next, the resized BF images were converted into binary images by thresholding to differentiate clopidogrel bisulfate particles from the background. Then, using the knowledge obtained from the first step, within these binary images, Form I and Form II particles were manually classified (indicated in red and blue, respectively). Eventually, five discrete-valued images with a resolution of 128 px × 128 px were finalized and used as training data for the dynamic sampling Raman, shown in **Figure 4-4**.

4.3.6 Experimental Implementation of SLADS

Dynamic sampling Raman imaging was conducted by using the confocal Raman microscope described in section 4.3.2, coupled with SLADS algorithm and Raman classifiers trained for clopidogrel bisulfate samples. Another replicate of clopidogrel bisulfate sample was prepared for Raman imaging, with 50% Form I and 50% Form II by mass. The SLADS stopping condition was set such that experimental measurements automatically ended when the estimated image reconstruction error was less than 1%. More measurements (to 35% of all pixels sampled) were conducted after the SLADS stopping condition to evaluate and validate the trained stopping condition.

4.4 Results and Discussions

4.4.1 Simulation Results for SLADS

Before implementing SLADS to Raman image acquisition, the ground truth results were used to simulate the process of SLADS. The discrete valued ground truth Raman image is shown

in Figure 4-5(g), which was used to simulate SLADS algorithm in Raman spectra acquisition. Previously recorded integrated intensity of each spectrum was used to rescale the discrete valued Raman image in order to reconstruct a grayscale Raman spectroscopic image with classification information, shown as Figure 4-5(h). The simulation results show that the dead time between each Raman spectrum collection was 71.5 μs on average, including the time for Raman spectrum classification and for the time for SLADS to determine the next measurement location. Moreover, the SLADS algorithm provided reconstructed Raman image in real time. Figure 4-5(a) and Figure 4-5(b) show the measured pixel location and the reconstructed image with 15% sampling rate, respectively. The errors in image reconstruction by using SLADS was 0.23%, based on the difference of reconstructed image with 15% sampling rate and ground truth image, which was shown in Figure 4-5(c). With 35% of all 16,384 pixels measured, the reconstructed image was identical to the ground truth image.

4.4.2 Comparison with Random Sampling

Simulated random sampling experiments were performed to compare the performance and efficiency of SLADS to other alternative sparse sampling methods. Similar as the SLADS simulation, Figure 4-5(g) was employed for the random sampling Raman spectra acquisition. The image reconstruction algorithm was the same as that in SLADS algorithm. The measured pixel locations, reconstructed image, and errors in image reconstruction corresponding to measurements of 15% of all 16,384 pixels are shown in Figure 4-5(d)-(f), respectively. The image reconstruction error with random sampling was 4.65% with 15% sampling rate, which is 20 times higher than the error with SLADS. In Figure 4-5(f), most of the errors by using random sampling were located at the boundaries of the sample particles in different classes. It is reasonable that the boundaries between different species have high spatial frequency information compared to other positions in the image, which means the boundaries are the most ambiguous and informative positions for the measurements. Random sampling does not adjust its measurement density according to the different spatial frequency at different positions, which significantly reduce its efficiency. On the other hand, dynamic sampling adjusted the measurement density and selectively measure more pixels with higher spatial frequency information. Therefore, reconstructed image via SLADS showed much lower error percentage than that via random sampling with the same sampling rate.

4.4.3 Experimental Implementation of SLADS for Confocal Raman Imaging

By using the theory in Section 4.2.2 and the experimental methods in Section 4.3.5, the stopping condition for SLADS of <1% expected distortion was achieved for sampling rate at 15.8%. Figure 4-6(a) and Figure 4-6(b) show the measured pixel location and the reconstructed image respectively. In order to assess SLADS algorithm at this stopping condition (15.8% sampling rate), additional subsequent measurements were made for up to 35% of all pixels sampled, shown in Figure 4-6(c). In this case, there is no additional change showing in the reconstructed images after 29% of all pixels were sampled. By comparing the reconstructed image with 15.8% sampling rate to that with 35% sampling rate, 67 pixels of the chemical identification results were different, which were 0.41% of all 16,384 pixels in the image. The experimental results are consistent with the assessment of the simulation results. The SLADS approach preferentially sampled at the boundaries of different species. The SLADS algorithm enabled to collect Raman spectra at informative locations, which provide high edge resolution in the classification.

4.4.4 Performance Analysis and Potential Application of SLADS

Point scanning confocal Raman microscopy is a technique, where the Raman spectrum acquisition time for each pixel is relatively long, due to the low spontaneous Raman signal. Especially, the data acquisition time for each measurement is over 10 times longer than the time required for the dead time of SLADS, including laser beam relocation, data transfer, spectra analysis, and SLADS computation. Therefore, implementing SLADS into confocal Raman microscopy show significant advantages in measurement time reduction. It is reasonable to expect SLADS applications in other imaging system, which single-pixel measurement time is much longer than the random access and SLADS computation time. For example, energy dispersive spectroscopy³², photoacoustic imaging^{33,34}, and infrared hyperspectral imaging³⁵, might be beneficial in measurement acceleration by using SLADS.

Scarborough *et al.* demonstrated using SLADS to reduce the measurement time and X-ray dose for synchrotron X-ray diffraction image.³⁶ In the application of dynamic sampling in synchrotron X-ray diffraction for crystal positioning, the reduced number of measurement points significantly reduced the X-ray dosage used for crystal identification, and avoided excessive X-ray damage. In that study, they suggest that the benefits of SLADS increase significantly with the increase of the number of pixels in the image. In SLADS simulations based on X-ray diffraction

imaging, an 80-fold increase in resolution (from 40×80 to 512×512 pixels) yielded a 6-fold reduction in the fraction of pixels sampled for similar distortions. Based on this evidence, for the application of SLADS in Raman imaging, the sampling rate at stopping condition could be even lower with the higher resolution of sampling, but at the expense of increased overall measurement time.

It is worthwhile to compare SLADS with the previously described sampling strategy by Rowlands *et al.*²³. They developed the sampling strategy by comparing between spline and Kriging interpolations. Unfortunately, the previous work lacked the assessment of the reliability of the algorithm, with no model calculation with ground truth results. Thus, it is hard to compare these two methods quantitatively. In the reconstructed image of Rowlands *et al.* publication, the boundaries between species were significantly blurred, which could result in the misclassification rate along the boundaries and in the whole image is anticipated to be relatively large. One possible reason for this effect is that the difference between spline and Kriging interpolations of a pixel is not proportional to the information that the pixel. The Rowlands *et al.* algorithm preferred to collect Raman spectra at the location with the greatest differences of two interpolations, rather than the locations that will optimize reconstruction. Furthermore, the Rowlands *et al.* algorithm operated on continuously valued images, and then utilized the difference between pixel values directly to select the next measurement. However, the difference between continuously valued pixels is a different question than posed in the present reconstruction, which focused on properly classifying composition. The algorithm proposed by Rowlands *et al.* cannot readily be extended to discrete valued images due to the discrete nature of the classification. All pixels in labeled interpolations would either be identical using the two methods or differ by a score of one, which is not capable of conducting selective sparse sampling.

In this case, the confocal Raman imaging was used to investigate the mixture of clopidogrel bisulfate Form I/Form II and background. Both of clopidogrel bisulfate Form I and Form II are spherical particles. However, practically, the discrete classification boundaries identified by SLADS are not representative of the smoothly varying changes in composition expected for realistic three-dimensional objects (in this case, spheroidal particles). Although the present study was primarily focused on quantitatively and accurately classifying composition, it is worthwhile to discuss the methods to obtain the intensity information. In order to recover the intrinsic gradient in intensities of each spheroidal particles, there are two strategies could be considered. One strategy

was demonstrated in Figure 4-5(h), in which the original classified images were subsequently weighted by the ground-truth vector magnitudes of the filtered spectra. Another potential strategy is using continuous-SLADS, which has been demonstrated in previous study.²⁹ Continuous-SLADS is capable of dealing with continuously valued images, in which different regions have either hard boundaries or soft gradient edges²⁹. Since gradients in continuously valued images are smoother, SLADS will sample along this smoother more spread out boundary. Therefore, if calculated with only one label allowed per pixel, the misclassification rate of the image reconstruction by using continuous-SLADS, will decrease much slower than the discrete valued SLADS algorithm. But if the RMSE was computed as the error metric, continuous-SLADS will decrease the error faster, because it is trained to find the pixel that reduces the RMSE the most. However, as the method proposed by Rowland *et al.*, continuous-SLADS suffers from the inaccuracy of using the difference between continuously valued pixels to quantify the difference of each pixel.

Although the central focus of the present work is the reduction in measurement time, the SLADS algorithm has an additional benefit of reducing the total optical dose to the sample. Phototoxicity is routinely observed in Raman imaging, especially for live cells, in which local heating and/or photochemical reactions significantly perturb the system under investigation during the process of data acquisition^{37,38}. Furthermore, in pharmaceutical materials analysis, significant laser-induced local heating could potentially result in phase transformation between different crystal forms of pharmaceutical materials³⁹. Therefore, the implementation of SLADS into Raman imaging results in broader applications in biological and pharmaceutical materials analysis with the reduction of optical dose. Moreover, other imaging techniques, where sample overheating or damage caused by extended exposure to light source is a major concern, such as four-wave mixing microscopy for living cell imaging, using dynamic sampling to reduce the number of sampling points can be potentially beneficial.

Another significant advantage of SLADS approach is that it can be directly compatible with broad classes of point scanning confocal Raman microscope. Although in this study, all of the Raman images were acquired by the prototype instrument shown in Figure 4-1, commercial confocal Raman systems should be available for the implementation of SLADS. The compatibility of SLADS is able to be assessed by comparisons between the Raman spectrum collection time for single pixel and the random access time for the commercial Raman microscope. In many practical

commercially available confocal Raman systems supporting imaging applications, the single-pixel measurement time dictates the overall frame rate, such that SLADS is expected to be beneficial for Raman image acquisitions.

4.5 Conclusion

A supervised learning approach for dynamic sampling (SLADS) was integrated into a confocal Raman imaging microscopy system to greatly reduce imaging time. Due to its high chemical specificity and requirement for minimal sample preparation, Raman imaging has found broad application in both chemical and biological sample analysis. With weak spontaneous Raman scattering, conventional Raman imaging typically requires a relatively long integration time to obtain a high signal to noise ratio, which limits the applications. By analyzing the preceding set of measurements, the SLADS algorithm identified the next most information-rich sampling location, which resulted in a significant reduction of total number of data points required for image generation in Raman microscopy. Integration of SLADS into the feedback for beam positioning enabled fully autonomous control over the selection of location and data acquisition. By using this approach, reliable chemical images of pharmaceutical materials were obtained with ~15.8% sampling, representing a ~6-fold reduction in measurement time relative to full field of view sampling with negligible loss (< 0.5%) in image quality. SLADS has the distinct advantage of being directly compatible with standard confocal Raman instrumentation. Furthermore, SLADS is not limited to Raman imaging, providing an improvement of point-scanning imaging speed whenever the single-pixel measurement time dictates the time frame for image generation. The flexibility of the sampling architecture enables compatibility with a variety of applications, providing benefits including increased imaging speed and reduced sample damage.

4.6 References

1. Stewart, S.; Priore, R. J.; Nelson, M. P.; Treado, P. J. *Annu Rev Anal Chem* **2012**, *5*, 337-360.
2. Edinger, M.; Bar-Shalom, D.; Rantanen, J.; Genina, N. *Pharm Res-Dordr* **2017**, *34*, 1023-1036.
3. Vajna, B.; Patyi, G.; Nagy, Z.; Bodis, A.; Farkas, A.; Marosi, G. *J Raman Spectrosc* **2011**, *42*, 1977-1986.

4. Hartshorn, C. M.; Lee, Y. J.; Camp, C. H.; Liu, Z.; Heddleston, J.; Canfield, N.; Rhodes, T. A.; Walker, A. R. H.; Marsac, P. J.; Cicerone, M. T. *Anal Chem* **2013**, *85*, 8102-8111.
5. Lawson, L. S.; Rodriguez, J. D. *Anal Chem* **2016**, *88*, 4706-4713.
6. Dieing, T.; Henrich, M.; Richter, E. *Spectroscopy-Us* **2012**, 29-29.
7. Kairdolf, B. A.; Qian, X. M.; Nie, S. M. *Anal Chem* **2017**, *89*, 1015-1031.
8. Kong, K.; Kendall, C.; Stone, N.; Notingher, I. *Adv Drug Deliver Rev* **2015**, *89*, 121-134.
9. Yosef, H. K.; Krauss, S. D.; Lehtonen, T.; Jutte, H.; Tannapfel, A.; Kafferlein, H. U.; Bruning, T.; Roghmann, F.; Noldus, J.; Mosig, A.; El-Mashtoly, S. F.; Gerwert, K. *Anal Chem* **2017**, *89*, 6893-6899.
10. Piredda, P.; Berning, M.; Boukamp, P.; Volkmer, A. *Anal Chem* **2015**, *87*, 6778-6785.
11. Muro, C. K.; Doty, K. C.; Bueno, J.; Halamkova, L.; Lednev, I. K. *Anal Chem* **2015**, *87*, 306-327.
12. Doty, K. C.; Muro, C. K.; Bueno, J.; Halamkova, L.; Lednev, I. K. *J Raman Spectrosc* **2016**, *47*, 39-50.
13. Starbuck, C.; Spartalis, A.; Wai, L.; Wang, J.; Fernandez, P.; Lindemann, C. M.; Zhou, G. X.; Ge, Z. *Crystal Growth & Design* **2002**, *2*, 515-522.
14. Chieng, N.; Rades, T.; Aaltonen, J. *J Pharmaceut Biomed* **2011**, *55*, 618-644.
15. Gordon, K. C.; McGoverin, C. M. *Int J Pharmaceut* **2011**, *417*, 151-162.
16. Li, C.; Zhang, D. L.; Slipchenko, M. N.; Cheng, J. X. *Anal Chem* **2017**, *89*, 4863-4867.
17. Zhang, C.; Li, J. J.; Lan, L.; Cheng, J. X. *Anal Chem* **2017**, *89*, 4502-4507.
18. Imitola, J.; Cote, D.; Rasmussen, S.; Xie, X. S.; Liu, Y. R.; Chitnis, T.; Sidman, R. L.; Lin, C. P.; Khoury, S. J. *J Biomed Opt* **2011**, *16*, 021109-021101 - 021109-021110.
19. Schlucker, S.; Schaeberle, M. D.; Huffman, S. W.; Levin, I. W. *Anal Chem* **2003**, *75*, 4312-4318.
20. Oshima, Y.; Sato, H.; Kajiura-Kobayashi, H.; Kimura, T.; Naruse, K.; Nonaka, S. *Opt Express* **2012**, *20*, 16195-16204.
21. Watanabe, K.; Palonpon, A. F.; Smith, N. I.; Chiu, L. D.; Kasai, A.; Hashimoto, H.; Kawata, S.; Fujita, K. *Nat Commun* **2015**, *6*, 10095.
22. Kong, K.; Rowlands, C. J.; Elsheikha, H.; Notingher, I. *Analyst* **2012**, *137*, 4119-4122.

23. Rowlands, C. J.; Varma, S.; Perkins, W.; Leach, I.; Williams, H.; Notingher, I. *J Biophotonics* **2012**, *5*, 220-229.
24. Chowdhury, A. U.; Ye, D. H.; Song, Z. T.; Zhang, S. J.; Hedderich, H. G.; Mallick, B.; Thirunahari, S.; Ramakrishnan, S.; Sengupta, A.; Gualtieri, E. J.; Bouman, C. A.; Simpson, G. J. *Anal Chem* **2017**, *89*, 5959-5966.
25. Kong, K.; Rowlands, C. J.; Varma, S.; Perkins, W.; Leach, I. H.; Koloydenko, A. A.; Williams, H. C.; Notingher, I. *P Natl Acad Sci USA* **2013**, *110*, 15189-15194.
26. Godaliyadda, G. M. D. P.; Ye, D. H.; Uchic, M. D.; Groeber, M. A.; Buzzard, G. T.; Bouman, C. A. *IEEE Transactions on Computational Imaging* **2018**, *4*, 1-16.
27. Bishop, C. M. *Pattern recognition and machine learning*; springer: New York, NY 10013, USA, 2006.
28. Godaliyadda, G.; Ye, D. H.; Uchic, M. D.; Groeber, M. A.; Buzzard, G. T.; Bouman, C. A. *Electronic Imaging* **2016**, *2016*, 1-8.
29. Godaliyadda, G.; Ye, D. H.; Uchic, M. D.; Groeber, M. A.; Buzzard, G. T.; Bouman, C. A. *arXiv preprint arXiv:1703.04653* **2017**.
30. Ehrentreich, F.; Summchen, L. *Anal Chem* **2001**, *73*, 4364-4373.
31. Liland, K. H.; Almoy, T.; Mevik, B. H. *Appl Spectrosc* **2010**, *64*, 1007-1016.
32. Zaluzec, N. J.; Burke, M. G.; Haigh, S. J.; Kulzick, M. A. *Microsc Microanal* **2014**, *20*, 323-329.
33. Hu, S.; Maslov, K. I.; Tsytsarev, V.; Wang, L. V.; SPIE, 2009, p 3.
34. Jeon, M.; Kim, J.; Kim, C. *Medical & biological engineering & computing* **2016**, *54*, 283-294.
35. Kelley, D. B.; Goyal, A. K.; Zhu, N.; Wood, D. A.; Myers, T. R.; Kotidis, P.; Murphy, C.; Georgan, C.; Raz, G.; Maulini, R.; Müller, A. In *SPIE Defense + Security*; SPIE, 2017, p 10.
36. Scarborough, N. M.; Godaliyadda, G. M. D. P.; Ye, D. H.; Kissick, D. J.; Zhang, S. J.; Newman, J. A.; Sheedlo, M. J.; Chowdhury, A. U.; Fischetti, R. F.; Das, C.; Buzzard, G. T.; Bouman, C. A.; Simpson, G. J. *J Synchrotron Radiat* **2017**, *24*, 188-195.
37. Notingher, I.; Verrier, S.; Romanska, H.; Bishop, A. E.; Polak, J. M.; Hench, L. L. *Spectrosc-Int J* **2002**, *16*, 43-51.
38. Kuzmin, A. N.; Pliss, A.; Lim, C. K.; Heo, J.; Kim, S.; Rzhetskii, A.; Gu, B.; Yong, K. T.; Wen, S. C.; Prasad, P. N. *Sci Rep-Uk* **2016**, *6*, 28483.
39. Sobocinski, R. L.; Pemberton, J. E. *Langmuir* **1988**, *4*, 836-845.

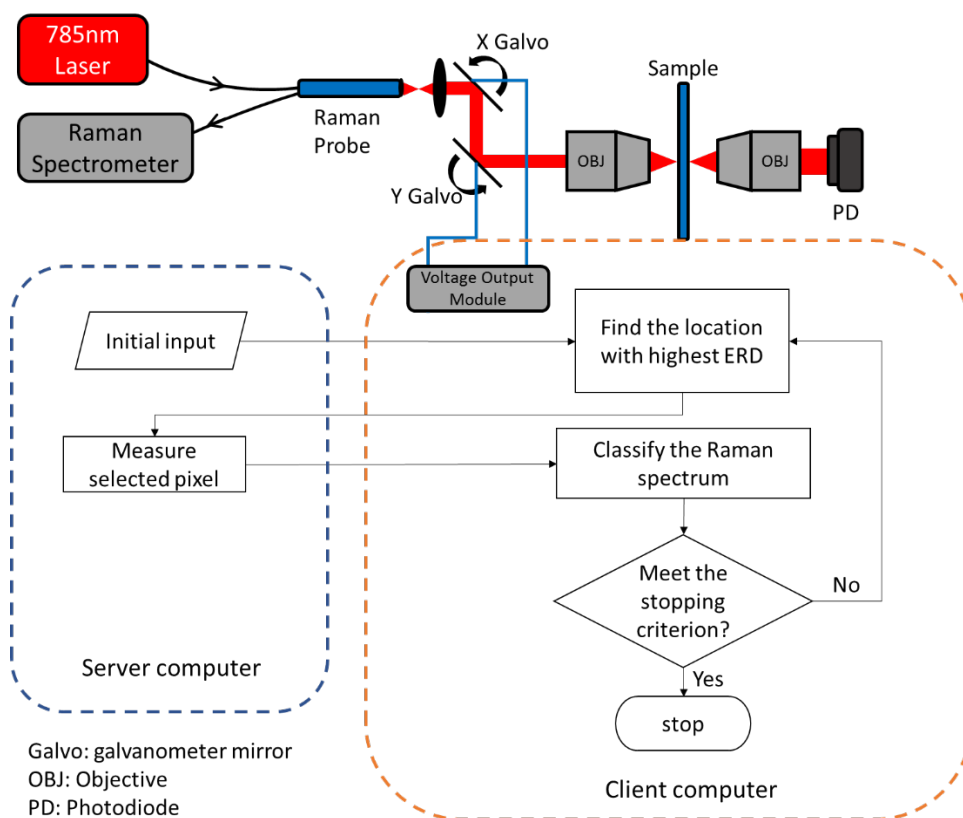


Figure 4-1 Schematic of the random access confocal Raman microscope with the dynamic sampling Raman imaging workflow described in the flowchart. The server computer (outlined in blue to the left) controlled the Raman spectrometer, and the client computer (outlined in orange to the right) controlled the laser beam location, operated the SLADS algorithm, and performed Raman spectral classification.

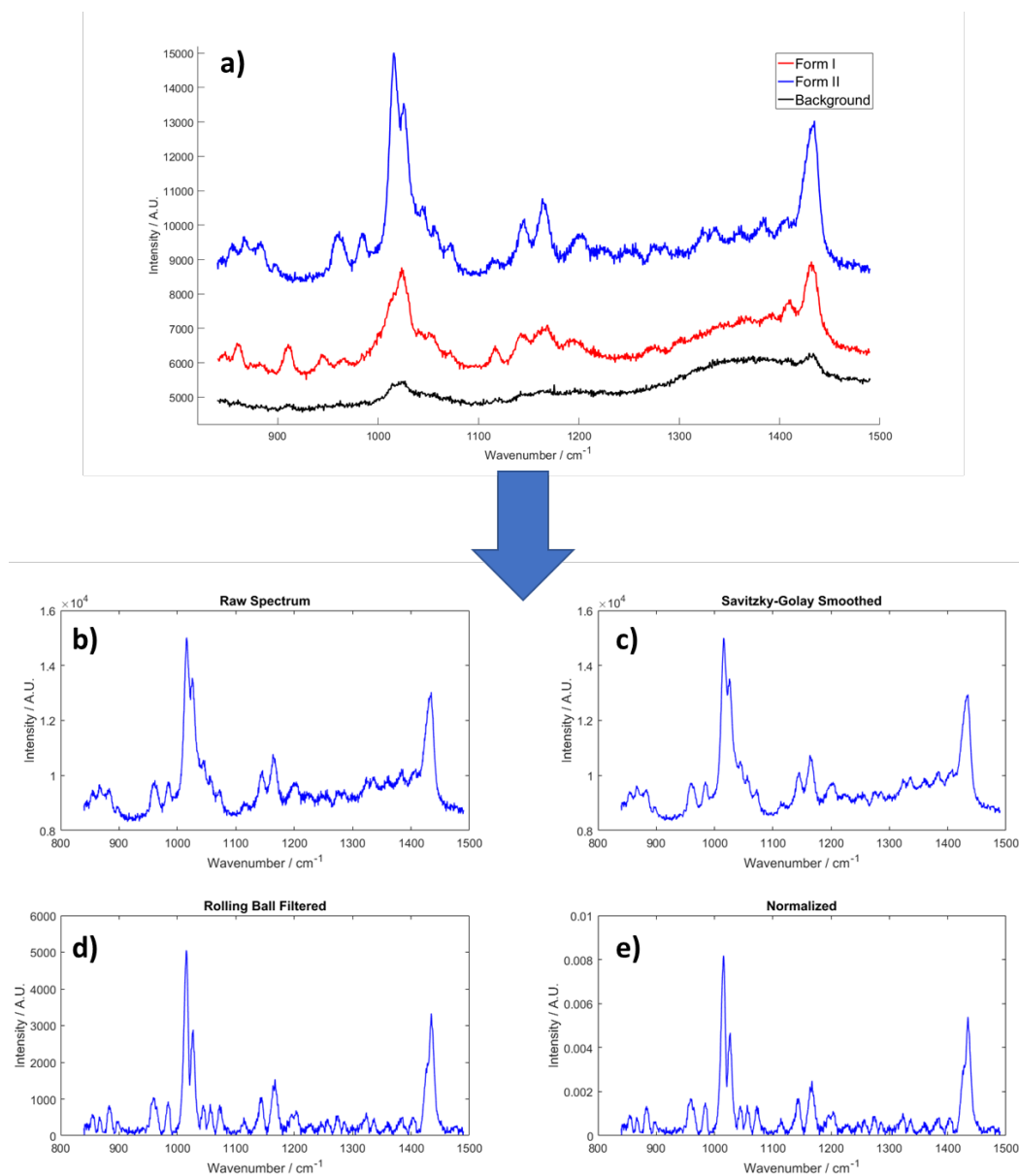


Figure 4-2 Preprocessing of Raman spectrum to improve SNR

(a) Sample raw Raman spectra of Form I, Form II clopidogrel bisulfate polymorphs, and background, and (b)-(e) illustrated the spectral processing procedure by using a spectrum of Form II clopidogrel bisulfate measurement, including Savitzky-Golay filtering, rolling ball filtering, and normalization to the area under the curve.

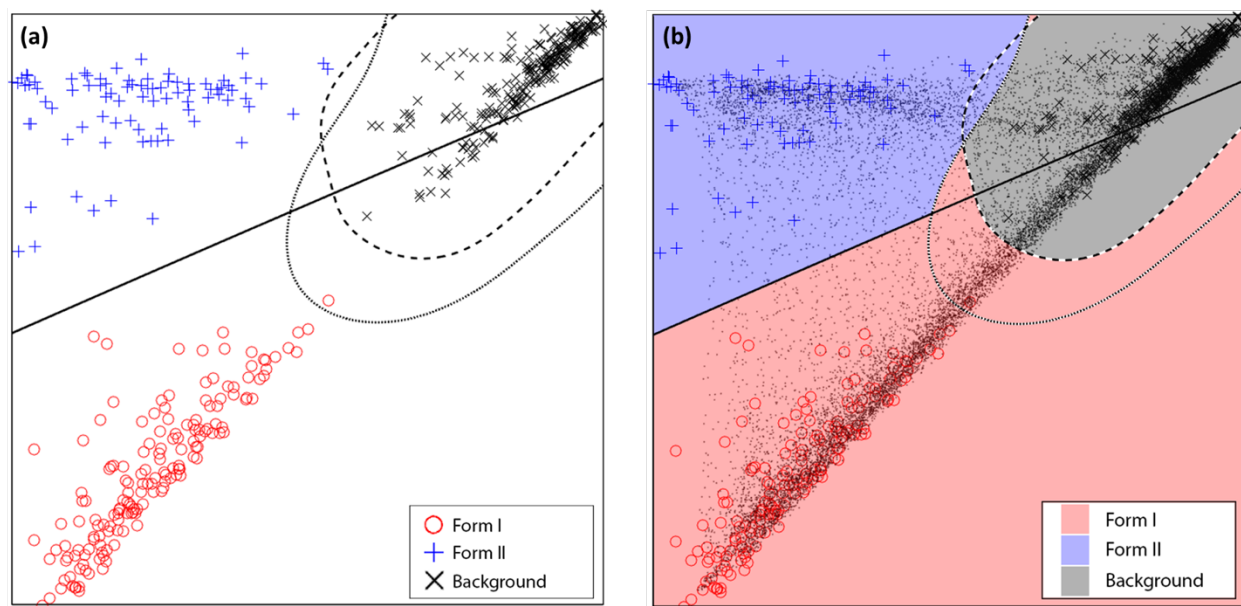


Figure 4-3 Classification of Raman spectra into three classes

(a) Training spectra projected onto the two-dimensional space generated from the two principal eigenvectors produced by LDA, and three decision boundaries constructed using 1-vs-1 SVM, in which the solid curve separates Form I and Form II clopidogrel data points, the dashed line curve separates Form II and background data points, and the dotted curve separates Form I and background data points. (b) Visual representation of Raman spectral classification decision making. All 16,384 spectra collected by the ground truth Raman imaging experiment are projected to the same LDA space as gray dots. Shaded areas that these dots fall into indicate corresponding classification results.

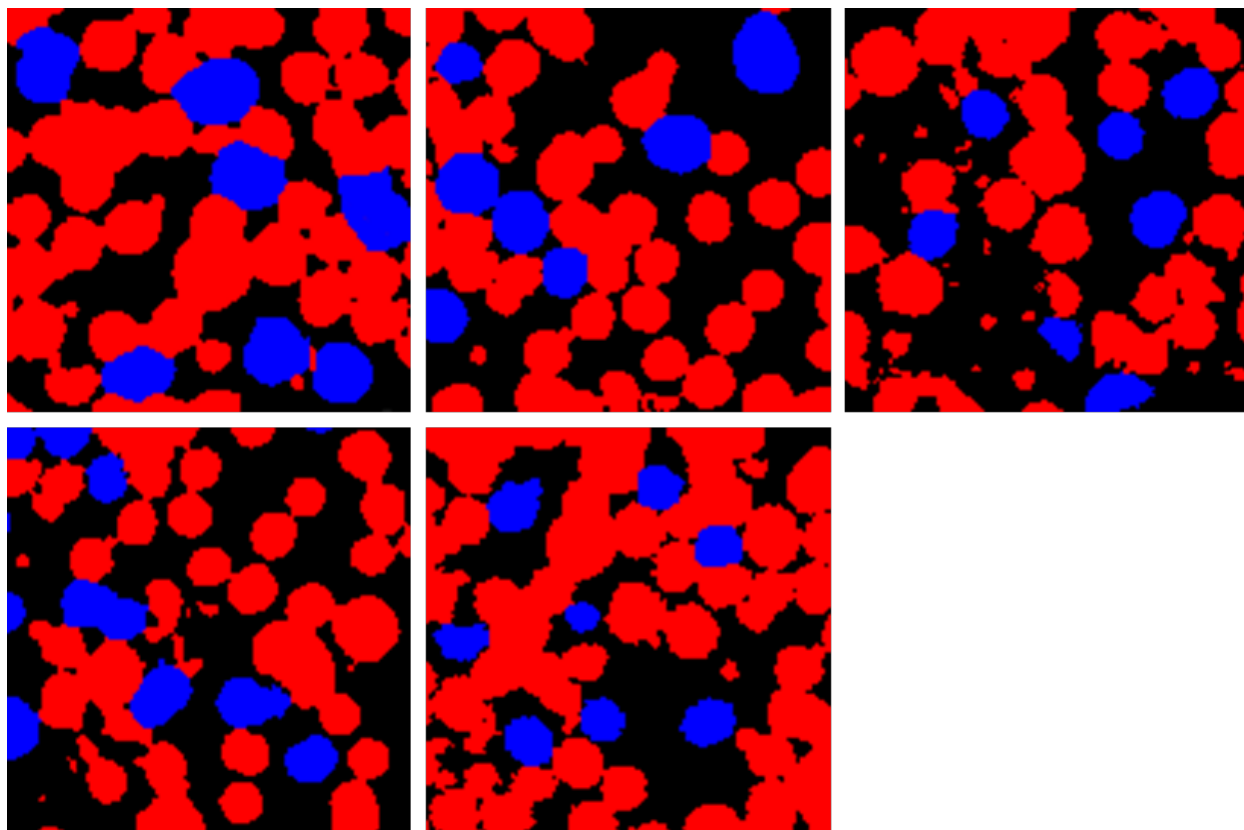


Figure 4-4 Training images for sampling Raman imaging stopping conditions. The five discrete valued images (128 pixels x 128 pixels) cropped and processed from the bright field image of the clopidogrel bisulfate Form I/Form II mixture; and then labeled based on the SHG image

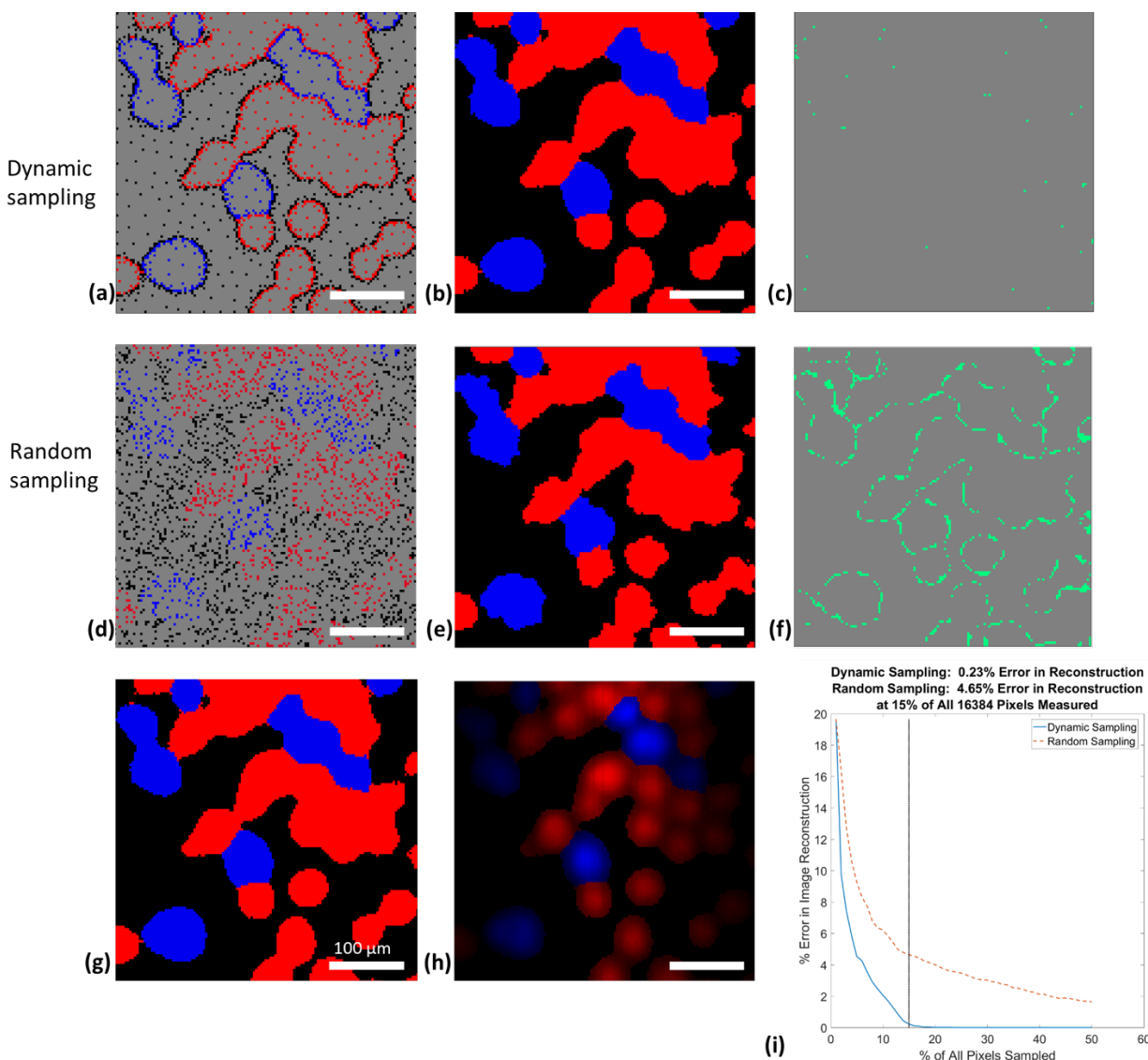


Figure 4-5 Simulated dynamic sampling and random sampling image reconstruction with a ground truth image

Results shown in the figure are both at 15% sampling percentage (2,458 out of 16,384 pixels are measured). (a) Measured locations of simulated dynamic sampling. (b) Reconstructed image of dynamic sampling. (c) Dynamic sampling image reconstruction error map. (d) Measured locations of simulated random sampling. (e) Reconstructed image of random sampling. (f) Random sampling image reconstruction error map. (g) The ground truth image in which all 16,384 pixels are sampled. (h) Grayscale image with classification information by rescaling every pixel in the discrete valued image by the integrated intensity of the Raman spectrum measured at the pixel (i) Comparison of image reconstruction error using dynamic sampling (blue solid line) and random sampling (orange dotted line) as a function of sampling percentage. In (a) (b) (d) (e) (g) and (h) red pixels correspond to Form I polymorph, blue pixels correspond to Form II polymorph, black pixels correspond to background, and gray pixels correspond to unmeasured locations. In (c) and (f) gray pixels correspond to locations where the reconstructed image is the same as the ground

truth image, and cyan pixels correspond to locations where reconstructed image differs from the ground truth image.

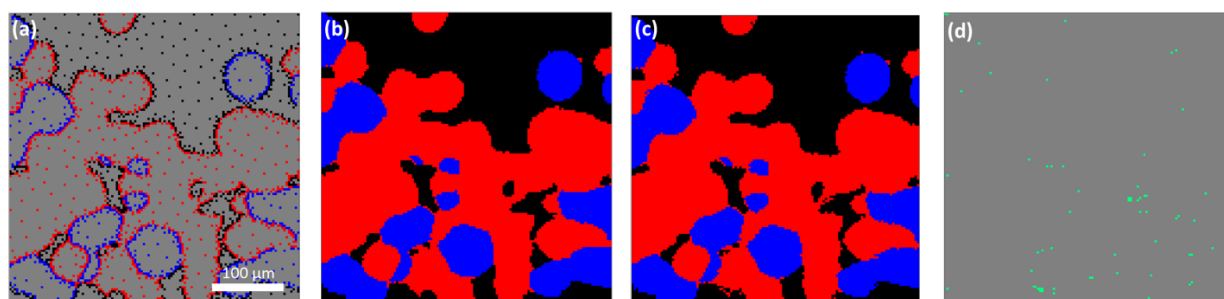


Figure 4-6 Experimental results of confocal Raman imaging with implementation of SLADS. (a) Measurement locations correspond to the stopping criterion (15.8% sampling percentage). (b) Reconstructed Raman image. (c) Reference image reconstructed after 35% of all pixels locations are measured. (d) Difference between reconstructed image at 15.8% sampling percentage and the reference image. 67 pixels are different, corresponding to 0.41% difference. In (a) (b) and (c), red pixels correspond to Form I polymorph, blue pixels correspond to Form II polymorph, black pixels correspond to background, and gray pixels correspond to unmeasured locations. In (d) gray pixels correspond to locations where reconstructed image is the same as the ground truth image, and cyan pixels correspond to locations where reconstructed image is different from the ground truth image.

CHAPTER 5. IN SITU ACCELERATED STABILITY TESTING

5.1 Introduction

Production of amorphous solid dispersions (ASDs) offers a broadly applicable approach for kinetically circumventing solubility limitations of poorly soluble active pharmaceutical ingredients (APIs). In an ASD, the API is cast in a glassy polymer matrix with relatively high aqueous solubility, such that the API is forced into solution upon dissolution of the matrix.¹⁻⁴ When optimizing a polymer/excipient/API cocktail for preparing final dosage forms, one critical consideration is the long-term stability of the API within the ASD. Concentrating the API in the ASD to minimize the total mass load of the final dosage form is balanced by a desire to also reduce the chances of API nucleation and crystallization during storage of the ASD. For poorly soluble APIs, the crystalline form often exhibits negligible bioavailability, passing through the digestive tract for oral final dosage forms. In intravital formulations, residual insoluble API particulates can pose additional risks from inducing foreign body embolism.⁵⁻⁸ For these reasons, stability testing is widely used to inform the optimization of final dosage forms. High throughput testing requires a host of different test materials, multiple replicates of which at multiple time points are required for stability assessment over long timeframes (up to year-long timeframes). The high throughput, high sampling rate, and long incubation times (weeks to months) can significantly complicate sample preparation and storage capacities even when using accelerated conditions.

The duration of stability testing is ultimately dictated by the sensitivity with which crystal formation can be quantified for informing kinetic modeling, with a suite of methods currently brought to bear to address this measurement challenge. Numerous methods can be brought to bear on stability assessments. These include polarized light microscopy (PLM)⁹⁻¹⁰, X-ray powder diffraction (PXRD)¹¹⁻¹², differential scanning calorimetry (DSC)^{10, 13-14}, Raman spectroscopy¹⁵⁻¹⁶, Fourier transform infrared spectroscopy (FTIR)^{15, 17-18}, and solid state nuclear magnetic resonance (sNMR)^{15, 19}. PLM is one of the most common methods used for determining the presence of crystalline content in stability testing. Despite its widespread use, PLM can only provide qualitative information on optically transparent samples and is commonly complicated by interference from occlusions, contaminants, and crystalline excipients.⁹ As a consequence, PLM is challenging to integrate into fully automated quantitative analyses of crystallinity. PXRD is

arguably the current “gold standard” for detecting trace crystallinity within the pharmaceutical industry but generally does not enable quantification at low crystallinity, takes several minutes for sample preparation/analysis, and requires several mg of material for analysis. A large dynamic range with correspondingly low limits of detection has multiple benefits in accelerated stability testing, including: i) improved statistical confidence in kinetics parameters, ii) simplified kinetic modeling without the requirements to account for depletion effects, iii) compatibility with low API-load ASDs, iv) reduced volumes for sample storage during testing, and v) reduction in the timeframe necessary for decision-making in stability assessments. For the majority of the methods routinely used for API analysis, limits of detection are on the order of a fraction of a percent, providing a relatively narrow dynamic range in crystalline API detection; in some cases, the total drug loading may only be on the order of a few percent.

In addition to the limited dynamic range, the majority of these common analysis tools probe only ensemble-average behaviors, masking possible intrinsic heterogeneity in crystal nucleation and growth kinetics. For example, it is well established that the nucleation and growth kinetics can differ substantially for crystals generated on the surfaces of ASD particles relative to the bulk.^{18,}
²⁰ Even in homogeneous media, subtle differences in local environment can produce variance in crystal growth rates.²¹ The impact of this variance in growth kinetics on subsequent performance remains unresolved, due in part to the dearth of methods currently available to quantitatively inform the inherent variation in single-particle growth kinetics.

Nonlinear optical imaging has the potential to provide the limits of detection required for investigating single-particle growth kinetics and fill this knowledge gap. Nonlinear optics has recently gained traction in the pharmaceutical industry for sensitive detection and quantification of trace crystalline content within amorphous formulations.^{11, 22-26} Second harmonic generation (SHG) describes the coherent conversion of light to twice the frequency, which is symmetry-forbidden in centrosymmetric media but allowed in assemblies of lower symmetry, including the large majority of noncentrosymmetric crystals. SHG provides a near background free measurement of the crystalline fraction of an ASD since the disordered, amorphous material will not produce coherent SHG. Due to the sensitivity and selectivity of SHG, routine measurements can be made with a limit of detection in the ppm regime.²⁷ Utilizing the sensitivity of SHG to crystalline content for identification of regions of interest, the detection limits for Raman^{5, 28} and XRD²⁹ have been lowered into the ppm regime as well. The low limits of detection of SHG

microscopy enabled quantification of crystallization kinetics in ASDs spanning a 4 order of magnitude range in crystallinity.^{27, 30}

In this work, the quantitative capabilities of SHG analysis are substantially improved further while simultaneously dramatically reducing the total sample volume and storage burden through *in situ* analysis. A controlled environment for *in situ* stability testing (CEiST) was developed to leverage the sensitive, non-destructive analysis capabilities of SHG for continuous monitoring of individual crystallites during nucleogenesis and growth. The CEiST platform allowed for single particle tracking over hours to days under accelerated stability conditions typical for ASD analysis. Monitoring the same fields of view over time lowers noise in determinations of the nucleation rates and crystal growth rates obtained from accelerated stability tests while simultaneously lowering the amount of sample required.

5.2 Experimental Methods

ASD samples of ritonavir (15%), sorbitan monolaurate (10%), copovidone (74%), and colloidal silicon dioxide (1%) were prepared by AbbVie Inc., prepared as spray dried dispersions (SDDd) and hot melt extrudates (HMEs). Samples without the sorbitan monolaurate were also made where the copovidone weight percent was increased to 84%. HME samples were milled to prior to use. All powder samples were placed into the CEiST chamber or into a standard stability chamber as thin layers (~300 μm).

The CEiST's design is shown in Figure 5-1. The CEiST has two sections separated by greased o-rings that can be kept at different RHs depending on the saturated salt solution put into the reservoirs. Both compartments of the device were kept at an elevated RH of 75% through all experiments by using a saturated NaCl solution. The RH in each compartment of the CEiST was validated using reversible Moisture Indicator strips (Indigo Instruments, 33813-2080). The temperature was controlled by using two Tempco low density cartridge heaters (LDC00003) placed at different locations on the CEiST and a thermocouple in the center for feedback control by a custom controller built by the Johnathan Amy Facility at Purdue, depicted in Figure 5-1(A). An IR thermal image of the CEiST in Figure 5-1(C) confirms uniform temperature within $\pm 2^\circ\text{C}$ of the set point temperature. Samples were placed onto cover slips and then onto one of the ten wells within the CEiST. For comparative purpose, a standard stability chamber was made by

placing saturated sodium chloride solution into the bottom of a desiccator wrapped in heat tape. The temperature of the entire chamber was monitored by thermocouple feedback.

Accelerated stability tests were performed using a SONICC microscope from Formulatrix (Bedford, MA) for SHG imaging that was modified in house for epi detection. For the *in situ* stability testing, samples in the CEiST chamber were maintained an elevated temperature and humidity during SHG imaging. For samples maintained in the standard stability chamber, aliquots were sampled at select time points, analyzed by SHG under ambient conditions, and then discarded. The time from stability chamber removal through testing was about 10 minutes. Experiments were performed using 350 mW excitation laser power and 894 ms exposure time, repeated every hour (duty cycle of 2.8×10^{-4}). SHG was measured in the transmission direction due to the high transparency of samples in the CEiST through deliquescence of the ASD. SHG was collected in the epi direction for powdered samples before being subjected to elevated temperature and humidity. For samples within the standard chamber, three fields of view were used for each time point. For samples within the CEiST, several fields of view were selected from each of 3 wells prepared for each ASDs.

5.3 Results and Discussions

The performance of CEiST was evaluated relative to a conventional temperature and humidity controlled chamber through side-by-side comparisons of accelerated stability testing of 15% DL (w/w) ritonavir ASDs with HME at 50°C/75%RH, the results of which are summarized in Figure 5-2. The amorphous excipients present in the HME ASDs did not produce significant coherent SHG signal. In contrast, ritonavir crystals adopt an SHG-active non-centrosymmetric lattice upon crystallization, enabling selective detection of crystalline ritonavir in HME ASDs using a particle counting algorithm.³¹ SHG images at four representative time points are shown in Figure 5-2(A) for ASDs stored in a standard chamber at elevated temperature and humidity, and Figure 5-2(B) for ASDs stored in the CEiST under identical target conditions. For quantitative comparison of ritonavir crystallization between the two platforms, the average crystal area at each time point was recovered by particle counting, shown in Figure 5-2(C). The error bars in Figure 5-2(C) represent the standard deviations of three fields of view for each time point. The SHG micrographs and the average crystal areas observed for both the standard chamber and the CEiST platform were in excellent agreement, suggesting that the conditions produced in the CEiST

platform are representative of those experienced in conventional temperature and humidity controlled chambers.

Using the CEiST platform, 10 trials of *in situ* accelerated stability testing were run in parallel for ritonavir crystallization in different ASDs at 50°C and 75% RH. The ASDs were prepared with different components and different manufacturing techniques (see Experimental Methods). The ASD powder samples were examined by SHG microscopy and initially showed no detectable epi-SHG signal (i.e., no continuous regions of interest with at least 3 contiguous pixels of at least 3 counts). From previous studies using SHG to interrogate ASDs, this criterion corresponds to a lower limit of detection of 10 ppm crystallinity³⁰, indicating that the initial crystallinity in all cases was less than this lower limit of detection.

The SHG images and corresponding bright field images were automatically collected every hour starting from 0 to 48 hours. Four sets of representative SHG images at five different time points are shown in Figure 5-3. All of the images are shown with the same brightness scale for comparison. Based on the time-dependent SHG images, the incorporation of surfactant (span 20) increased the ritonavir nucleation rate and crystal growth rate in ASDs. In this case, the addition of span 20 resulted in more crystals and larger crystal size in accelerated stability testing, consistent with the presence of span 20 significantly reducing the stability of ritonavir against crystal formation in both hot melt extruded and spray dried ASDs. Compared with spray dried ASDs, HME samples showed a greater number of crystals and lower induction times in the accelerated stability testing.

When accelerated stability testing was performed by using the standard temperature and humidity control chamber, the sample was taken out of the controlled environment to enable SHG imaging under ambient conditions. Since temperature and humidity cycling can significantly change the crystallization kinetics (shown in Figure 5-4), all the samples using the standard chamber were discarded following SHG imaging. The perturbations associated with temperature cycling are attributed to a two-step process: i) increase in supersaturation upon cooling to room temperature, resulting in increased nucleation rate, followed by ii) increased diffusion upon return to elevated temperature and humidity, resulting in increased crystal growth rates. Multiple aliquots of sample were therefore required to collect images at different time points using conventional stability chambers to avoid kinetic artifacts from temperature cycling. This practice

was in stark contrast to measurements performed using the CEiST system, which supported continuous monitoring of the same fields of view within a sample under controlled conditions.

For each sample, single-particle tracking was performed to monitor the growth rates of individual particles, representative results of which are shown in Figure 5-5, selected from 4-6 different fields of view. The long axes of the needle-like ritonavir crystals (Form II) were used to quantify crystal size. The dispersion in crystal growth rates is shown in the inset plots of Figure 5-5. For individual crystals, error bars in the growth rates were assessed from the standard error of the slope of crystal size versus time. From inspection of the histograms of single crystal growth rates and the standard errors, it is clear that the dispersion in growth rates exceeds experimental uncertainties, and therefore reflects an intrinsic diversity in single crystal growth kinetics within the samples.

Single-particle tracking enabled by the CEiST platform provided substantial signal to noise benefits in nucleation kinetics as well. The average nucleation rates were found from the linear growth regime shown in Figure 5-6, by linear fitting of nucleation events from four different fields of view. The uncertainties reported in each plot arise from the variabilities of the fields of view. The linear region for fitting was marked by the dashed line. The nucleation rate in HME ASDs in Figure 5-6(A) is one order of magnitude higher than in SDD shown in Figure 5-6(B), in presence of 10% span 20 in the ASDs. The residual nuclei present in HME ASDs might be responsible for producing this higher nucleation rate. However, without the presence of span 20, the ritonavir nucleation rates are similar in both HME and SDD.

The substantial improvement in signal to noise for nucleation rate determination in CEiST can be understood considering the Poisson statistics associated with crystal genesis in combination with the sensitivity of SHG imaging to support single particle tracking. Nucleation rates using a standard stability chamber were calculated from the differences in the number of crystals between multiple independent samples analyzed at different time-points. Because each sample is statistically independent, the number of crystals in any given field of view is given by a Poisson-distribution. As a result, the nucleation rate is generated from the difference between two Poisson-distributed numbers acquired at different time-points. In the linear kinetics regime, the number of previously nucleated crystals contributes to the uncertainty in the number of new particles, rapidly degrading the precision to which the number of new particles can be determined based on Poisson statistics. In contrast, the nucleation rates in the CEiST chamber were calculated from the

differences in the numbers of new crystals *within the same single FoV*, removing all statistical uncertainties regarding the number of pre-existing crystals. As such, uncertainty in the nucleation rate is defined only by the Poisson statistics for the number of new particles within a given FoV. The signal to noise advantage associated with nucleation rates determined from analysis of single samples versus stochastic sampling is shown in Figure 5-7. Following the initial onset of nucleation, Poisson-distributed uncertainties in the differences in particle numbers between independent samples rapidly degrade the precision to which nucleation rates can be determined. However, no such statistical loss in SNR is expected from repeated analysis of a single FoV.

Interestingly, the SNR improvement afforded by single particle tracking pairing SHG microscopy with the CEiST platform provides a simultaneous advantage in reducing sample volume requirements. Stability testing of pharmaceutical formulations can extend over several weeks, or months, or even years, for each of potentially many different formulation candidates.³²⁻³³ The temperature cycling complication coupled with the Poisson statistics limitations associated with crystal analysis pose cost challenges associated with archiving large volumes of identical replicate samples in controlled environments for testing times spanning multiple months or years. Continuous *in situ* monitoring of a single field of view over the entire time-course of a stability assessment (e.g., by SHG microscopy) provides reduction in sample volume requirements proportional to the number of time-points used for kinetics assessments. For example, in the present study with up to 48 time-points recorded for a given sample, the total assay volume is correspondingly reduced up to 48-fold.

The collective results of the single-particle tracking experiments provide insights into the molecular connections between stability, method of preparation, and composition of ASDs. The higher observed crystal growth rate in SDD relative to HME ASDs suggests a fundamental difference in the molecular diffusion constant within the matrices, as the ritonavir growth rate is diffusion limited in this regime. The origin of this disparity in diffusion constants may potentially be attributed to the desolvation step in SDD generation, which may potentially produce a higher density of microscopic voids in the final products and higher molecular diffusion. Presence of Span 20 in ASD formulations of ritonavir contributes to processability, but dramatically increases molecular diffusion, with corresponding increases in single crystal growth rates. Specifically, the surfactant, span 20 increased the crystal growth rate by ~5 times for HME and ~3 times for SDD.

The surfactant, span 20 induced ~50-fold and ~20-fold change in nucleation rates for HME and SDD, respectively. The nucleation kinetics are also distinctly different between SDD and HME ASDs in the presence of span 20, with nucleation rates were about an order of magnitude higher in HME. This difference in nucleation rate may potentially arise from the presence of residual nuclei within the melt in the HME materials from incomplete melting. Optimization of conditions for HME preparation strikes a balance between the competing desires for higher temperatures to remove residual nuclei and lower temperatures to minimize pyrolysis. As such, the presence of trace residual nuclei within the HME is arguably more likely than in the SDD materials, consistent with the observations made by single particle tracking by SHG microscopy.

Recovery of the crystal growth rate distribution from single particle tracking suggests the presence of subtle but significant heterogeneity within the samples at microscopic scales. In all of the cases, the differences between the crystal growth rates of single crystals within individual fields of view are beyond the errors from fitting. This intrinsic variability in growth rates for nominally identical crystal forms suggests subtle differences in local diffusion rates, which in turn indicates heterogeneity in local structure within the surrounding matrix. The growth rate dispersion might result from subtle variation in local density, hydrophobicity, chemical composition, etc. The diversity in growth rates, and correspondingly diversity in local environments is similar between different formulations.

5.4 Conclusion

The CEiST platform developed in this work enabled single particle tracking during accelerated stability testing of ritonavir ASDs by SHG microscopy. The high selectivity of SHG to crystalline content provides high-contrast images over a large dynamic range of crystallinity for kinetics analysis. The advantage of monitoring the same field of view over time facilitated substantial signal to noise improvements for nucleation and growth rate assessments, supported single-particle tracking, and reduced the sample volume requirements by ~50 fold. From the single-particle tracking measurements by SHG microscopy, the heterogeneity in crystal growth rates within the ASDs suggests subtle but non-negligible local diversity in physical and/or chemical characteristics of the sample.

5.5 References

1. Kennedy, M.; Hu, J.; Gao, P.; Li, L.; Ali-Reynolds, A.; Chal, B.; Gupta, V.; Ma, C.; Mahajan, N.; Akrami, A.; Surapaneni, S., Enhanced Bioavailability of a Poorly Soluble VR1 Antagonist Using an Amorphous Solid Dispersion Approach: A Case Study. *Mol Pharmaceut* **2008**, *5* (6), 981-993.
2. Lalkshman, J. P.; Cao, Y.; Kowalski, J.; Serajuddin, A. T. M., Application of Melt Extrusion in the Development of a Physically and Chemically Stable High-Energy Amorphous Solid Dispersion of a Poorly Water-Soluble Drug. *Mol Pharmaceut* **2008**, *5* (6), 994-1002.
3. Serajuddin, A. T. M., Solid dispersion of poorly water-soluble drugs: Early promises, subsequent problems, and recent breakthroughs. *J Pharm Sci-Us* **1999**, *88* (10), 1058-1066.
4. Williams, R. O.; Watts, A. B.; Miller, D. A., Formulating Poorly Water Soluble Drugs Second Edition Preface. *Aaps Adv Pharm Sci* **2016**, *22*, Vii-Ix.
5. Schmitt, P. D.; Trasi, N. S.; Taylor, L. S.; Simpson, G. J., Finding the Needle in the Haystack: Characterization of Trace Crystallinity in a Commercial Formulation of Paclitaxel Protein-Bound Particles by Raman Spectroscopy Enabled by Second Harmonic Generation Microscopy. *Mol Pharmaceut* **2015**, *12* (7), 2378-2383.
6. Fang, C.; Bhattarai, N.; Sun, C.; Zhang, M. Q., Functionalized Nanoparticles with Long-Term Stability in Biological Media. *Small* **2009**, *5* (14), 1637-1641.
7. Neuberger, T.; Schopf, B.; Hofmann, H.; Hofmann, M.; von Rechenberg, B., Superparamagnetic nanoparticles for biomedical applications: Possibilities and limitations of a new drug delivery system. *J Magn Magn Mater* **2005**, *293* (1), 483-496.
8. Wang, S. H.; Xu, T.; Yang, Y. H.; Shao, Z. Z., Colloidal Stability of Silk Fibroin Nanoparticles Coated with Cationic Polymer for Effective Drug Delivery. *Acs Appl Mater Inter* **2015**, *7* (38), 21254-21262.
9. Carlton, R. A., Polarized Light Microscopy. *Pharmaceutical Microscopy* **2011**, 7-64.
10. Gupta, P.; Kakumanu, V. K.; Bansal, A. K., Stability and solubility of celecoxib-PVP amorphous dispersions: A molecular perspective. *Pharm Res* **2004**, *21* (10), 1762-1769.
11. Ghebremeskel, A. N.; Vemavarapu, C.; Lodaya, M., Use of surfactants as plasticizers in preparing solid dispersions of poorly soluble API: Stability testing of selected solid dispersions. *Pharm Res* **2006**, *23* (8), 1928-1936.
12. Newman, A. W.; Byrn, S. R., Solid-state analysis of the active pharmaceutical ingredient in drug products. *Drug Discov Today* **2003**, *8* (19), 898-905.

13. Baird, J. A.; Taylor, L. S., Evaluation of amorphous solid dispersion properties using thermal analysis techniques. *Adv Drug Deliver Rev* **2012**, *64* (5), 396-421.
14. Yoshihashi, Y.; Iijima, H.; Yonemochi, E.; Terada, K., Estimation of physical stability of amorphous solid dispersion using differential scanning calorimetry. *J Therm Anal Calorim* **2006**, *85* (3), 689-692.
15. Bugay, D. E., Characterization of the solid-state: spectroscopic techniques. *Adv Drug Deliver Rev* **2001**, *48* (1), 43-65.
16. Taylor, L. S.; Zografis, G., The quantitative analysis of crystallinity using FT-Raman spectroscopy. *Pharm Res* **1998**, *15* (5), 755-761.
17. Ng, Y. C.; Yang, Z. Y.; McAuley, W. J.; Qi, S., Stabilisation of amorphous drugs under high humidity using pharmaceutical thin films. *Eur J Pharm Biopharm* **2013**, *84* (3), 555-565.
18. Yang, Z. Y.; Nollenberger, K.; Albers, J.; Moffat, J.; Craig, D.; Qi, S., The effect of processing on the surface physical stability of amorphous solid dispersions. *Eur J Pharm Biopharm* **2014**, *88* (3), 897-908.
19. Harris, R. K., NMR studies of organic polymorphs & solvates. *Analyst* **2006**, *131* (3), 351-373.
20. Sun, Y.; Zhu, L.; Wu, T.; Cai, T.; Gunn, E. M.; Yu, L., Stability of Amorphous Pharmaceutical Solids: Crystal Growth Mechanisms and Effect of Polymer Additives. *Aaps J* **2012**, *14* (3), 380-388.
21. Li, L.; Fijneman, A. J.; Kaandorp, J. A.; Aizenberg, J.; Noorduyn, W. L., Directed nucleation and growth by balancing local supersaturation and substrate/nucleus lattice mismatch. *P Natl Acad Sci USA* **2018**, *115* (14), 3575-3580.
22. Chowdhury, A. U.; Zhang, S. J.; Simpson, G. J., Powders Analysis by Second Harmonic Generation Microscopy. *Anal Chem* **2016**, *88* (7), 3853-3863.
23. Kissick, D. J.; Wanapun, D.; Simpson, G. J., Second-Order Nonlinear Optical Imaging of Chiral Crystals. *Annu Rev Anal Chem* **2011**, *4*, 419-437.
24. Schmitt, P. D.; DeWalt, E. L.; Dow, X. Y.; Simpson, G. J., Rapid Discrimination of Polymorphic Crystal Forms by Nonlinear Optical Stokes Ellipsometric Microscopy. *Anal Chem* **2016**, *88* (11), 5760-5768.
25. Toth, S. J.; Madden, J. T.; Taylor, L. S.; Marsac, P.; Simpson, G. J., Selective Imaging of Active Pharmaceutical Ingredients in Powdered Blends with Common Excipients Utilizing Two-Photon Excited Ultraviolet-Fluorescence and Ultraviolet-Second Order Nonlinear Optical Imaging of Chiral Crystals. *Anal Chem* **2012**, *84* (14), 5869-5875.

26. Toth, S. J.; Schmitt, P. D.; Snyder, G. R.; Trasi, N. S.; Sullivan, S. Z.; George, I. A.; Taylor, L. S.; Simpson, G. J., Ab Initio Prediction of the Diversity of Second Harmonic Generation from Pharmaceutically Relevant Materials. *Cryst Growth Des* **2015**, *15* (2), 581-586.
27. Wanapun, D.; Kestur, U. S.; Taylor, L. S.; Simpson, G. J., Quantification of trace crystallinity in an organic powder by nonlinear optical imaging: Investigating the effects of mechanical grinding on crystallinity loss. *Abstr Pap Am Chem S* **2011**, 241.
28. Chowdhury, A. U.; Ye, D. H.; Song, Z. T.; Zhang, S. J.; Hedderich, H. G.; Mallick, B.; Thirunahari, S.; Ramakrishnan, S.; Sengupta, A.; Gualtieri, E. J.; Bouman, C. A.; Simpson, G. J., Second Harmonic Generation Guided Raman Spectroscopy for Sensitive Detection of Polymorph Transitions. *Anal Chem* **2017**, *89* (11), 5959-5966.
29. Newman, J. A.; Schmitt, P. D.; Toth, S. J.; Deng, F. Y.; Zhang, S. J.; Simpson, G. J., Parts per Million Powder X-ray Diffraction. *Anal Chem* **2015**, *87* (21), 10950-10955.
30. Song, Z. T.; Sarkar, S.; Vogt, A. D.; Danzer, G. D.; Smith, C. J.; Gualtieri, E. J.; Simpson, G. J., Kinetic Modeling of Accelerated Stability Testing Enabled by Second Harmonic Generation Microscopy (vol 90, pg 4406, 2018). *Anal Chem* **2018**, *90* (21), 13130-13130.
31. Smith, C. J.; Dinh, J.; Schmitt, P. D.; Stroud, P. A.; Hinds, J.; Johnson, M. J.; Simpson, G. J., Calibration-Free Second Harmonic Generation (SHG) Image Analysis for Quantification of Trace Crystallinity Within Final Dosage Forms of Amorphous Solid Dispersions. *Appl Spectrosc* **2018**, *72* (11), 1594-1605.
32. Mistry, P.; Amponsah-Efah, K. K.; Suryanarayanan, R., Rapid Assessment of the Physical Stability of Amorphous Solid Dispersions. *Cryst Growth Des* **2017**, *17* (5), 2478-2485.
33. Kommanaboyina, B.; Rhodes, C. T., Trends in stability testing, with emphasis on stability during distribution and storage. *Drug Dev Ind Pharm* **1999**, *25* (7), 857-868.

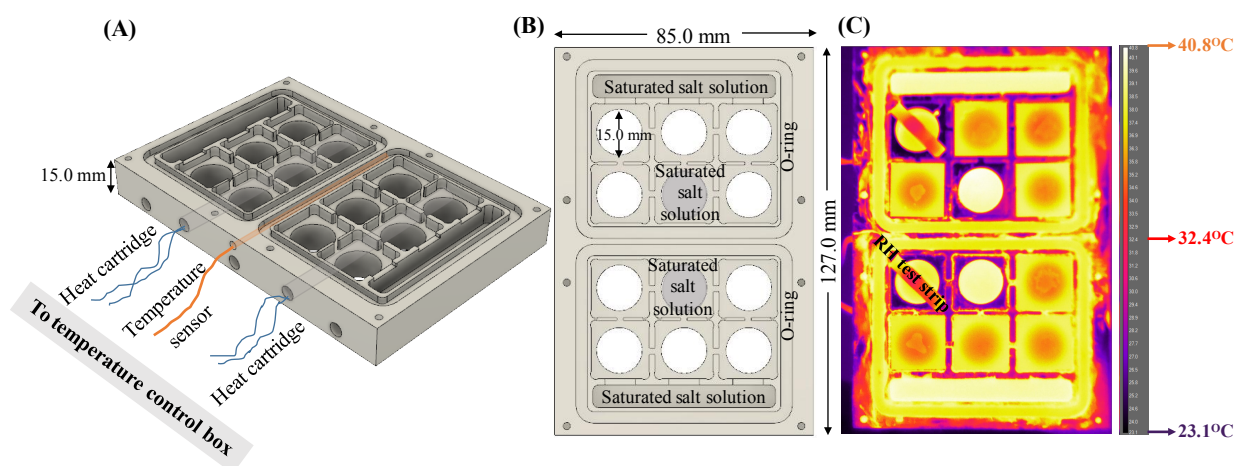


Figure 5-1 CEiST design and temperature validation

(A) (B) schematic of CEiST design; (C) IR thermal image of CEiST with the set temperature at 40 °C

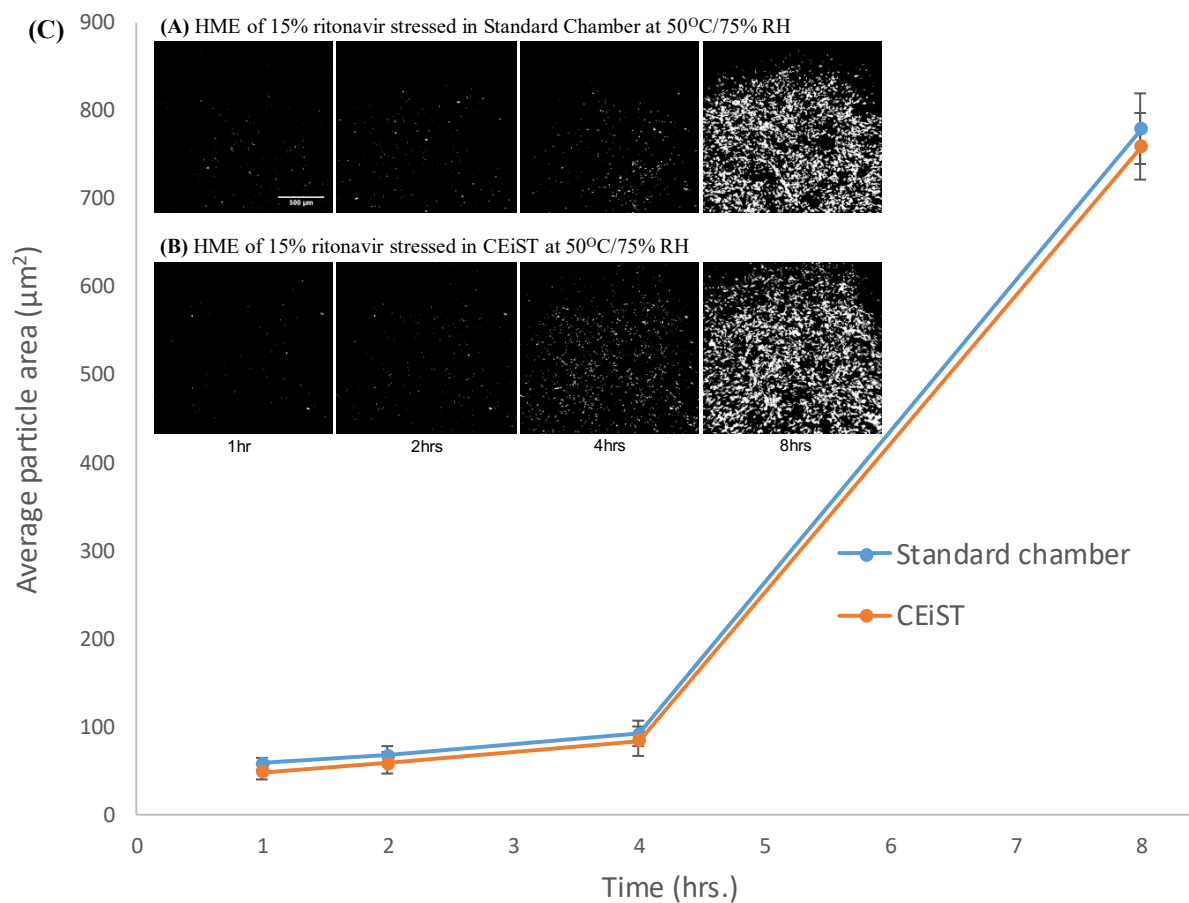


Figure 5-2 Validation of CEiST by comparison with standard chamber SHG images for time-dependent crystal growth of 15% HME ritonavir stressed in (A) standard chamber at 50°C/75%RH, and in (B) CEiST at 50°C/75%RH. (C) time-dependent average particle areas, which shows consistency between the two different methods.

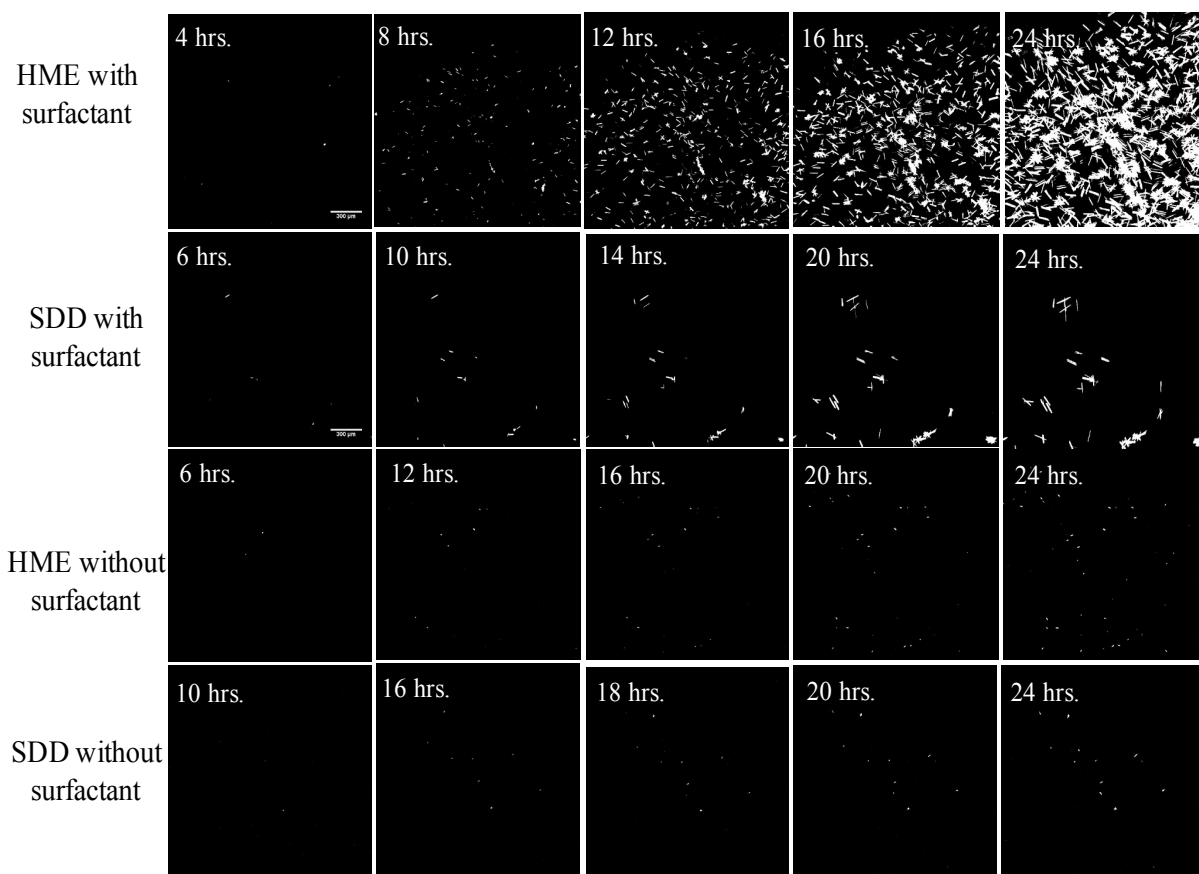


Figure 5-3 Time-dependent SHG images of 15% ritonavir ASDs stressed in CEiST.

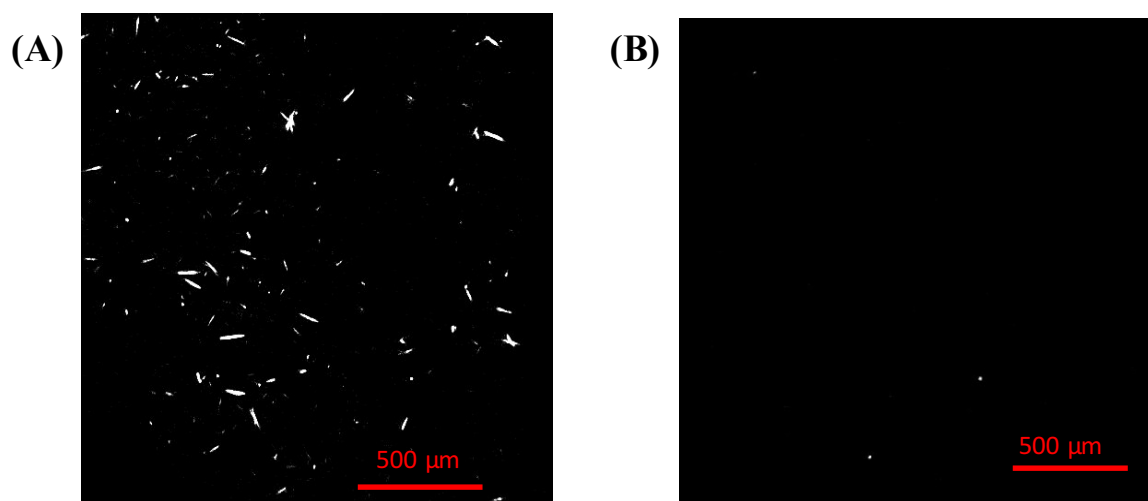


Figure 5-4 Temperature and humidity cycling effect on crystallization

A) 15% DL ritonavir ASDs stay in 50°C/75% RH chamber for 1 hour and then stay in room temperature for 15 min for 5 cycles;

B) 15% DL ritonavir ASDs stay in 50°C/75% RH chamber for 5 hours

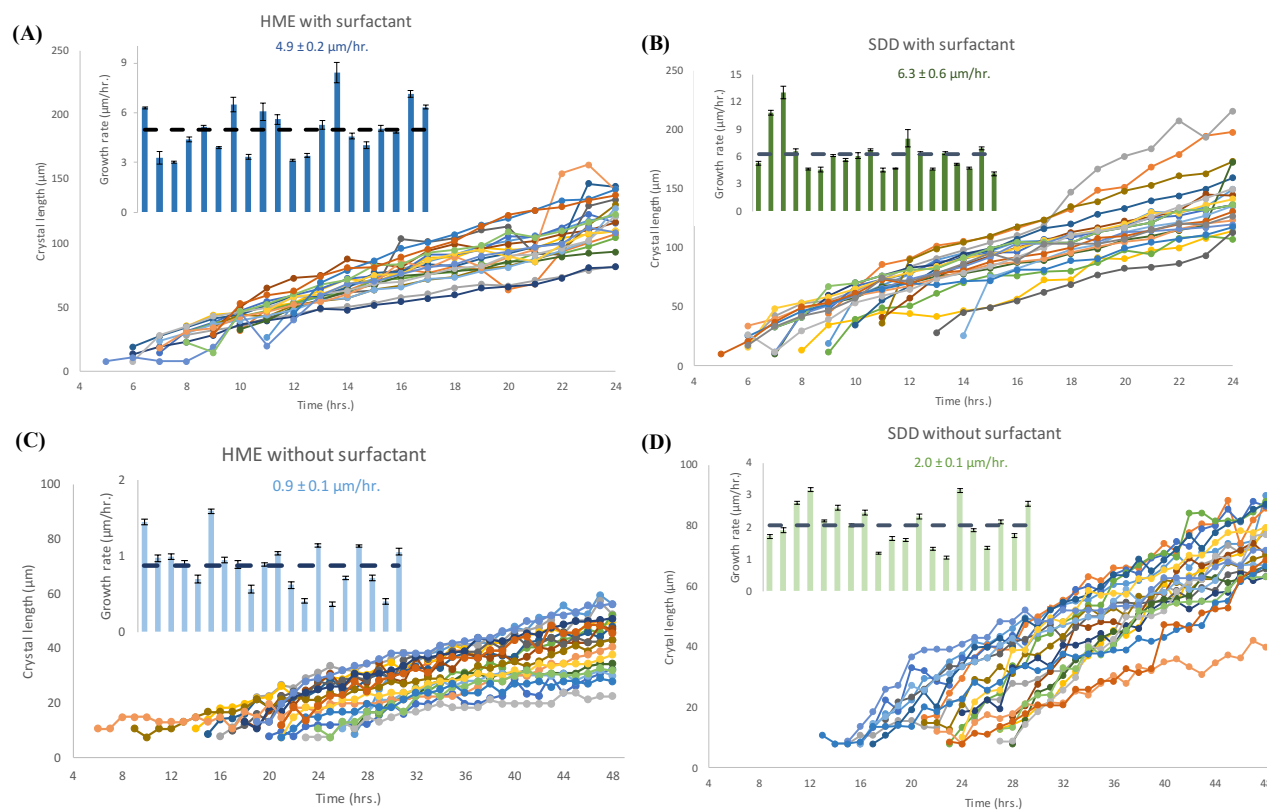


Figure 5-5 Individual crystal growth distribution in ASDs
 ASDs: (A) HME with surfactant, (B) SDD with surfactant, (C) HME without surfactant, and (D) SDD without surfactant. Each plot has 20 different crystals tracked along the entire time trace and selected from different FOVs. The inset in each plot shows the dispersion in growth rates with the average growth rates shown in each plot as dashed line.

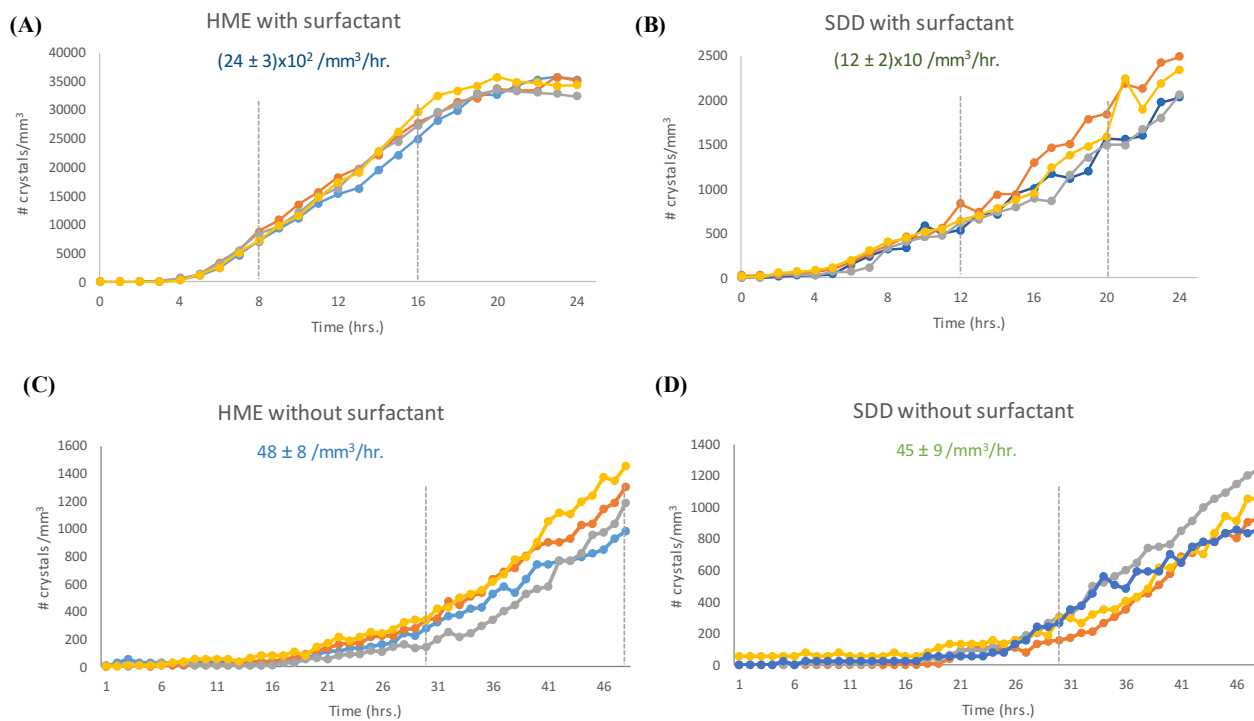


Figure 5-6 Nucleation rates for ASDs from individual FOVs
 ASDs: (A) HME with surfactant, (B) SDD with surfactant, (C) HME without surfactant, and (D) SDD without surfactant.

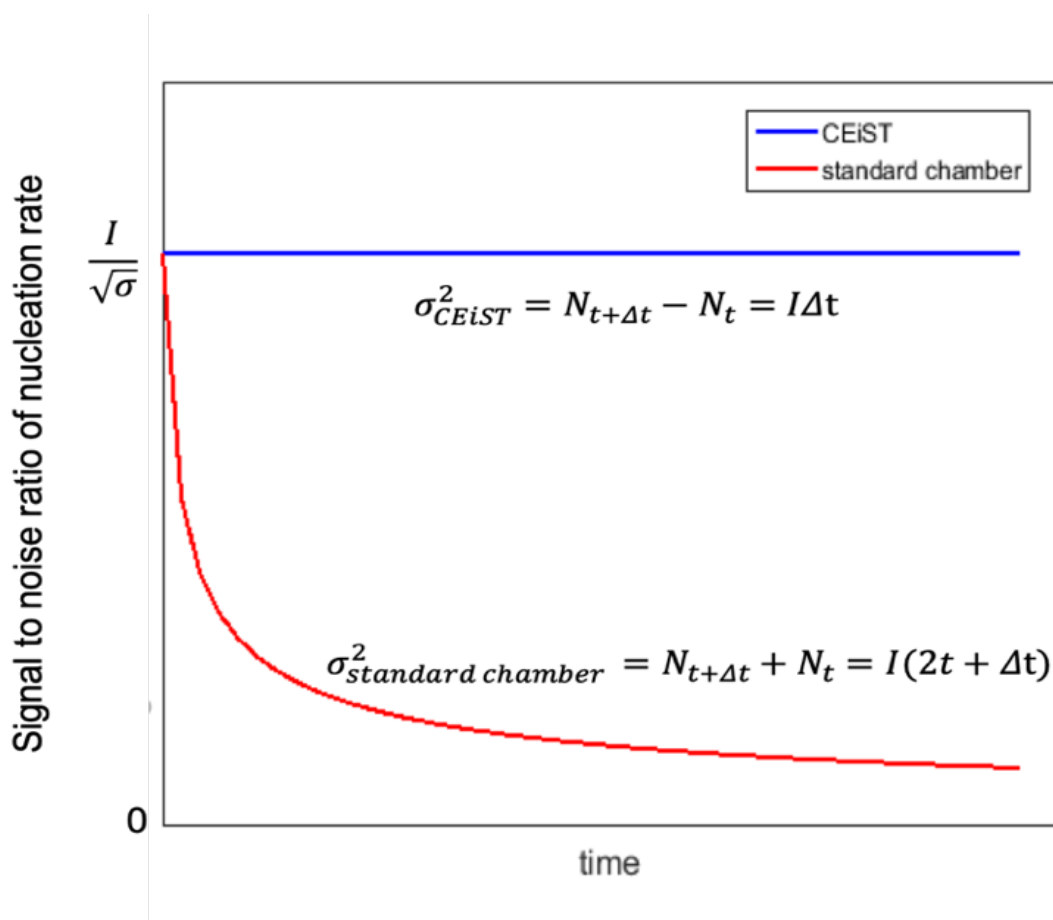


Figure 5-7 Comparison of signal to noise ratio of nucleation rate
 Theoretical signal to noise ratio of nucleation rate for *in situ* (blue line) vs conventional (red line) stability testing based on the Poisson statistics of crystal counting. I : nucleation rate, σ : uncertainty of nucleation rate based on Poisson statistics, N_t : number of crystals at time t

CHAPTER 6. CRYSTALLIZATION ON SURFACE VERSUS IN BURIED WITHIN AMORPHOUS SOLID DISPERSIONS

6.1 Introduction

Amorphous solid dispersions (ASDs), in which an active pharmaceutical ingredient (API) is maintained in an amorphous state within a polymer matrix, effectively improve the bioavailability of poorly water-soluble APIs. ASDs merely reduce the potential for API crystallization, but do not completely eliminate the possibility of API crystallization.¹ The shelf-lives of final dosage forms containing ASDs are often dictated by the rates of API crystallization, due to its impact on solubility and dissolution rate. Therefore, it is necessary to study the crystallization kinetics of the API within ASDs.

Accelerated stability testing is broadly used to investigate the crystallization processes of APIs in ASDs and then assess the stability of amorphous formulations. However, most accelerated stability tests were performed by using powdered pharmaceutical samples,² which only provided average information of the entire sample and cannot reveal API crystallization at different locations. Furthermore, API crystallization kinetics in bulk could be different from that on the surface. For example, Zhu, et al. demonstrated that crystal growth rate at the surface of amorphous griseofulvin is 10- to 100-fold faster than that in the bulk.³ It is worthwhile to study the spatial heterogeneity of stability of ASDs.

Several analytical techniques are commonly used for accelerated stability testing, including polarized light microscopy (PLM), powder X-ray diffraction (PXRD), Raman spectroscopy, IR spectroscopy, solid-state NMR spectroscopy, etc. However, PLM requires high transparency of samples, which limits its applications for turbid pharmaceutical materials.⁴ PXRD, as “powder” is included in its name, is only capable of dealing with powder materials and providing average information. Spectroscopic methods, like IR⁵, Raman⁶, and ssNMR⁷, are more conducive to investigate crystallinity on the surface, depending on the depth of radiation penetration. For example, Henson *et al.* used Raman microscopic mapping to characterize API polymorphs in tablets, where most of the spectral information was obtained from the tablet surface due to its low penetration.⁸ Most benchtop methods do not have great penetration or high enough sensitivity to measure trace crystallinity within bulk sample. Thakral *et al.* used synchrotron X-ray diffractometry to quantify crystallization from surface to core of a tablet, which enabled

investigation of heterogeneous crystallization in a tablet.⁹ However, X-ray diffraction patterns cannot provide the information to assess nucleation and crystal growth kinetics. Furthermore, access to a synchrotron X-ray light source is not commonly available for pharmaceutical formulation development.

In this study, SHG microscopy coupled with Controlled Environment for in situ Stability Testing (CEiST), which enabled single crystal growth tracking in accelerated stability testing (described in Chapter 5), were performed to investigate the crystallization kinetics in bulk and on surface of ASDs from hours to days. Since quantitative assessment of these growth rates is complicated by challenges associated with isolation of a particular contribution in complex ASD assemblies, we designed and built “sandwich” and “toast” structures, which exhibited seeded crystals between two ASD films and on the surface of ASD films, respectively. Single particle tracking was used to quantify the crystal size evolution overtime.

6.2 Experimental Methods

6.2.1 Sample Preparation

In order to investigate the ritonavir crystallization in bulk of ASDs, ritonavir crystals (Form II) were put in between two thin films made from an ASD, which built a “sandwich” structure (ASD film + crystals + ASD film). The instruments for ASD film making are shown in Figure 6-1, which contains a press (Atlas Manual 15 Ton Hydraulic Press, Specac), two heated platens (Atlas Series, Specac) with temperature controller (4000 Series High Stability Temperature Controller, Specac), and a cooling chamber (Atlas Constant Thickness Film Maker Accessory, Specac). To make a film with constant thickness, powder materials (50 - 60 mg) were put in between two round aluminum foil disks with 2 inches diameter and then into the Film Maker. The Film Maker is capable of conducting both the pressure and temperature, which is shown in Figure 6-1(B). The press is able to provides constant and uniform pressure from 0 to 15 Tons on the Film Maker. Meanwhile, the two heated platens can provide constant temperature for melting the powder sample with heat conductive materials. Last but not least, the cooling chamber is connected to a water-tap to cool the film down to room temperature by using water cooling.

The materials for making ASD films were milled ritonavir hot melt extrudates (manufactured by AbbVie in house), which consists of 15% amorphous ritonavir, 74% copovidone

(PVPVA), 10% Span 20 (sorbitan monolaurate), and 1% colloidal silicon dioxide (w/w). For each ASD film, it required 50 – 60 mg ritonavir ASDs with surfactant (Span 20). The procedure of making an ASD thin film is described below. First, put the film maker with the sample inside in between the two heated platens and heat it up to 115 °C for 5 minutes. After the sample is warmed up, apply 4 tons of pressure for 10 minutes while monitoring to keep the pressure at 4 tons. Then, decrease the temperature by setting 65 °C on the temperature controller. With the decreasing of temperature, monitor and keep the pressure at 4 tons for 10 minutes. After that, release the pressure and place it into the cooling chamber until the temperature of the sample reaches room temperature. The selective conditions (e.g., pressure, temperature, and time) were conducted to reduce the crystallization induced by compression and heat and keep the ASD film completely amorphous.

To investigate crystallization kinetics of crystal on the surface, individual ritonavir Form II crystals were placed onto the ASD film as seeded crystals manually by using a needle under an optical microscope, which built the “toast” structure. The seeded crystals were distributed sparsely, which would benefit the image analysis. There were less than 10 crystals in a 2 mm x 2mm field of view (FOV). On the other hand, the “sandwich” structure was constructed by pressing 2 films together with seeded crystals in between. The procedure for making a “sandwich” focused on pressing 2 films with seeded crystals together without breaking the crystals, shown below. First, it took 5 minutes to warm the sample to 98°C. Then, apply 1 ton of pressure for 10 minutes while monitoring to keep the pressure. Afterwards, decrease the temperature to 65 °C and monitor the pressure at 1 ton for another 10 minutes. The last step is releasing the pressure and place the sample into the cooling chamber until it cools down to room temperature. With the “sandwich” structure, all of the seeded crystals are within the bulk of the ASD. Both the “sandwich” and “toast” samples are transparent, which enabled transmitted SHG image acquisition during *in situ* accelerated stability testing.

6.2.2 Accelerated Stability Testing Experiments

The CEiST was used to provide the stressed environment for accelerated stability testing of our sample. The detailed description of the CEiST is in Chapter 5.2 and the design is shown in Figure 5-1. There are two sections and ten available sample wells within the CEiST, which are capable of acquiring results from 10 different samples. Samples were placed on cover slips in the sample wells, which enabled transmitted SHG image acquisition. The temperature was controlled

by two Tempco low density cartridge heaters (LDC00003) and a thermocouple for temperature feedback. The reliability of temperature control has been validated by IR thermal image collected by an IR camera (FLIR, A600-Series), which is within $\pm 2^{\circ}\text{C}$ of the set point temperature. In this study, all of the accelerated stability tests were conducted under 50°C . The CEiST consists of two sealed sections by greased o-rings, which can provide two different relative humidity (RH) by utilizing different saturated salt solutions. Moisture indicator strips (Indigo Instruments, 33813-2080) were employed to validate The RH in CEiST. In this study, saturated NaCl aqueous solution was used to keep the 75% RH in CEiST.

A commercial SONICC microscope (Formulatrix, Bedford, MA) was used to perform SHG image acquisition during accelerated stability testing. The instrumental details of SONICC microscope was demonstrated in Chapter 2.2. In this study, the excitation laser power at the sample position was 150 mW and the exposure time for collecting a single SHG image was 894 ms. All of the SHG images were collected in the transmission direction. CEiST was compatible with the sample stage inside SONICC microscope and maintained elevated temperature and humidity (50°C /75%RH) during the entire experimental process. Scheduled SHG image acquisitions for accelerated stability testing from hours to days were allowed by using the vendor software RockMaker, which can set up the locations of images and select measurement times. Since this study focuses on investigating ritonavir crystallization at an early stage, the SHG image collections repeated every hour for 48 hours.

6.3 Results and Discussions

To validate the reproducibility of “sandwich” and “toast” structures, 10 batches of each were made by following the procedure demonstrated in Section 6.2.1. All of the ritonavir ASD films were made to be $\sim 100\ \mu\text{m}$ thickness (single layer) and high transparency, which was highly reproducible. There were no detectable crystals found in the ASD films based on the examination conducted by SHG microscope (limit of detection: 10 ppm). No detectable crystals validated that the film making process with high pressure and temperature did not result in crystallization. The complete amorphous ASD films show advantages to avoid the impact from compression-induced nuclei. Other than ritonavir ASDs manufactured by hot melt extrusion, ASDs manufactured by rotary evaporator (rotovap) with the same components were also used to make ASD films. The rotovap ASD films were made by following the same procedure. However, the rotovap ASD films

contained a lot of air bubbles, which do harm to the homogeneity of the ASD films. The bubbles may result from the different density of sample materials due to the rotovap manufacturing.

The ASD “sandwich” samples were also examined by SHG microscopy to analyze the seeded crystals in bulk of ASDs. Since ritonavir Form II exhibits high SHG activity, SHG microscopy with 150 mW excitation laser power at sample position was employed to avoid the saturation of the detector (PMT). The lengths of seeded ritonavir crystals are about 10 – 300 μm . Unfortunately, there were several broken seeded crystals shown in SHG images due to the high pressure used for pressing two films together. Experiments under different pressure were conducted to optimize the “sandwich” construction procedure. However, with pressure less than 1 ton, the two films cannot be pressed together. In contrast, with pressure more than 1 ton, there were more broken crystals showing in SHG images. Thus, 1 ton was adopted as optimal pressure for the “sandwich” construction procedure.

Figure 6-2 showed eight representative images of time-dependent SHG images from time zero to 48 hours. The morphology of ritonavir crystals in bulk is significantly different from crystals on the surface. Although all of the seeded crystals are needle-shaped, the crystals in bulk grow while keeping their needle shape, while they exhibit “starburst” patterns on the ASD film surface. Crystal growth rates in bulk were calculated by tracking single crystal length evolution from time zero to 48 hours. The average crystal growth rate in bulk from five selected ones is $2.0 \pm 0.3 \mu\text{m/hr}$. It is difficult to track single crystal length on the surface resulted from too much particle overlapping. Thus, the diameter of the “starburst” pattern was treated as the crystal length of crystals on the ASD film surface. The average crystal growth rate on the ASD surface is $3.7 \pm 2.4 \mu\text{m/hr}$, which shows significant variance between five selected crystals.

Based on the comparison of crystal growth rate in bulk and on surface, there is no significant difference, which is not consistent with previous studies about surface-enhancement of crystal growth rate. However, on the other hand, the nucleation rate on the surface is extremely higher than in bulk of ASDs. The competition from nucleation might be one of the reasons, which reduce the crystal growth rate.

Different from crystal growth in bulk, there are many arguments about the mechanism of crystal growth on the surface in recent studies.¹⁰ One is the tension-release model: Since the density of crystals are higher than amorphous glass, it results in stress and strain effects in bulk that are much stronger than surface, which causes faster crystal nucleation and growth on the surface.¹¹

But Tanaka argues that the stress around the crystal “provides the free volume to the particles surrounding the crystal, increase their mobility, and help further crystallization”.¹² Based on his theory, crystal growth on surface will be slower than in bulk. Another well-known model is the surface mobility model: The higher crystal growth rate on the surface is due to higher mobility of surface molecules.^{13, 14} In addition, the higher mobility of surface molecules also results in a faster nucleation rate. The third model is based on different molecular packing on the surface versus in bulk.¹⁵ More experiments and studies are required to fully understand the crystal growth mechanism on surface versus in bulk.

6.4 Summary

In this study, growth rates for ritonavir crystals seeded in buried and exposed on supersaturated ASD film were quantitatively evaluated by SHG microscopy. In order to assess bulk crystallization kinetics, “sandwich” materials were produced, with sparse seeds of ritonavir single crystals pressed between two identical ASD films. In contrast, “toast” samples were prepared without the capping film to investigate crystallization on the surface. The morphology of crystals on the surface is like a “starburst”, while the crystals in bulk keep a needle-shape. However, based on single particle analysis by SHG microscopy time-series during *in situ* crystallization, the average growth rates for crystals in bulk and on surface do not show significant disparities, which differs from previous studies. The reason for this unusual phenomenon needs further study.

6.5 Future Work

First, more experiments and image analysis with seeded film in bulk versus on surface should be performed to check the reproducibility of current results. Second, assessment of the nucleation kinetics on the surface versus in bulk of ASDs. Meanwhile, do more literature studies about the mechanism of nucleation and crystal growth on the surface and in bulk. Moreover, crystallization within other ASDs (e.g., different API, excipients, manufacturing processes) is also worthy to study.

6.6 Reference

1. Newman, A.; Knipp, G.; Zografi, G., Assessing the performance of amorphous solid dispersions. *J Pharm Sci-Us* **2012**, *101* (4), 1355-1377.
2. Ivanisevic, I., Physical stability studies of miscible amorphous solid dispersions. *J Pharm Sci-Us* **2010**, *99* (9), 4005-4012.
3. Zhu, L.; Jona, J.; Nagapudi, K.; Wu, T., Fast surface crystallization of amorphous griseofulvin below T_g. *Pharmaceut Res* **2010**, *27* (8), 1558-1567.
4. Carlton, R. A., Polarized Light Microscopy. *Pharmaceutical Microscopy* **2011**, 7-64.
5. Chauhan, H.; Hui-Gu, C.; Atef, E., Correlating the behavior of polymers in solution as precipitation inhibitor to its amorphous stabilization ability in solid dispersions. *J Pharm Sci-Us* **2013**, *102* (6), 1924-1935.
6. Sinclair, W.; Leane, M.; Clarke, G.; Dennis, A.; Tobyn, M.; Timmins, P., Physical stability and recrystallization kinetics of amorphous ibipinabant drug product by Fourier transform Raman spectroscopy. *J Pharm Sci-Us* **2011**, *100* (11), 4687-4699.
7. Berendt, R. T.; Sperger, D. M.; Isbester, P. K.; Munson, E. J., Solid-state NMR spectroscopy in pharmaceutical research and analysis. *Trac-Trend Anal Chem* **2006**, *25* (10), 977-984.
8. Henson, M. J.; Zhang, L., Drug characterization in low dosage pharmaceutical tablets using Raman microscopic mapping. *Applied spectroscopy* **2006**, *60* (11), 1247-1255.
9. Thakral, N. K.; Mohapatra, S.; Stephenson, G. A.; Suryanarayanan, R., Compression-induced crystallization of amorphous indomethacin in tablets: characterization of spatial heterogeneity by two-dimensional X-ray diffractometry. *Mol Pharmaceut* **2014**, *12* (1), 253-263.
10. Sun, Y.; Zhu, L.; Kearns, K. L.; Ediger, M. D.; Yu, L., Glasses crystallize rapidly at free surfaces by growing crystals upward. *Proceedings of the National Academy of Sciences* **2011**, *108* (15), 5990-5995.
11. Schmelzer, J.; Pascova, R.; Möller, J.; Gutzow, I., Surface-induced devitrification of glasses: the influence of elastic strains. *Journal of Non-Crystalline Solids* **1993**, *162* (1-2), 26-39.
12. Tanaka, H., Possible resolution of the Kauzmann paradox in supercooled liquids. *Physical Review E* **2003**, *68* (1), 011505.
13. Wu, T.; Yu, L., Surface crystallization of indomethacin below T_g. *Pharmaceut Res* **2006**, *23* (10), 2350-2355.

14. Wu, T.; Sun, Y.; Li, N.; de Villiers, M. M.; Yu, L., Inhibiting surface crystallization of amorphous indomethacin by nanocoating. *Langmuir* **2007**, *23* (9), 5148-5153.
15. Farrance, O.; Jones, R.; Hobbs, J., The observation of rapid surface growth during the crystallization of polyhydroxybutyrate. *Polymer* **2009**, *50* (te15), 3730-3738.

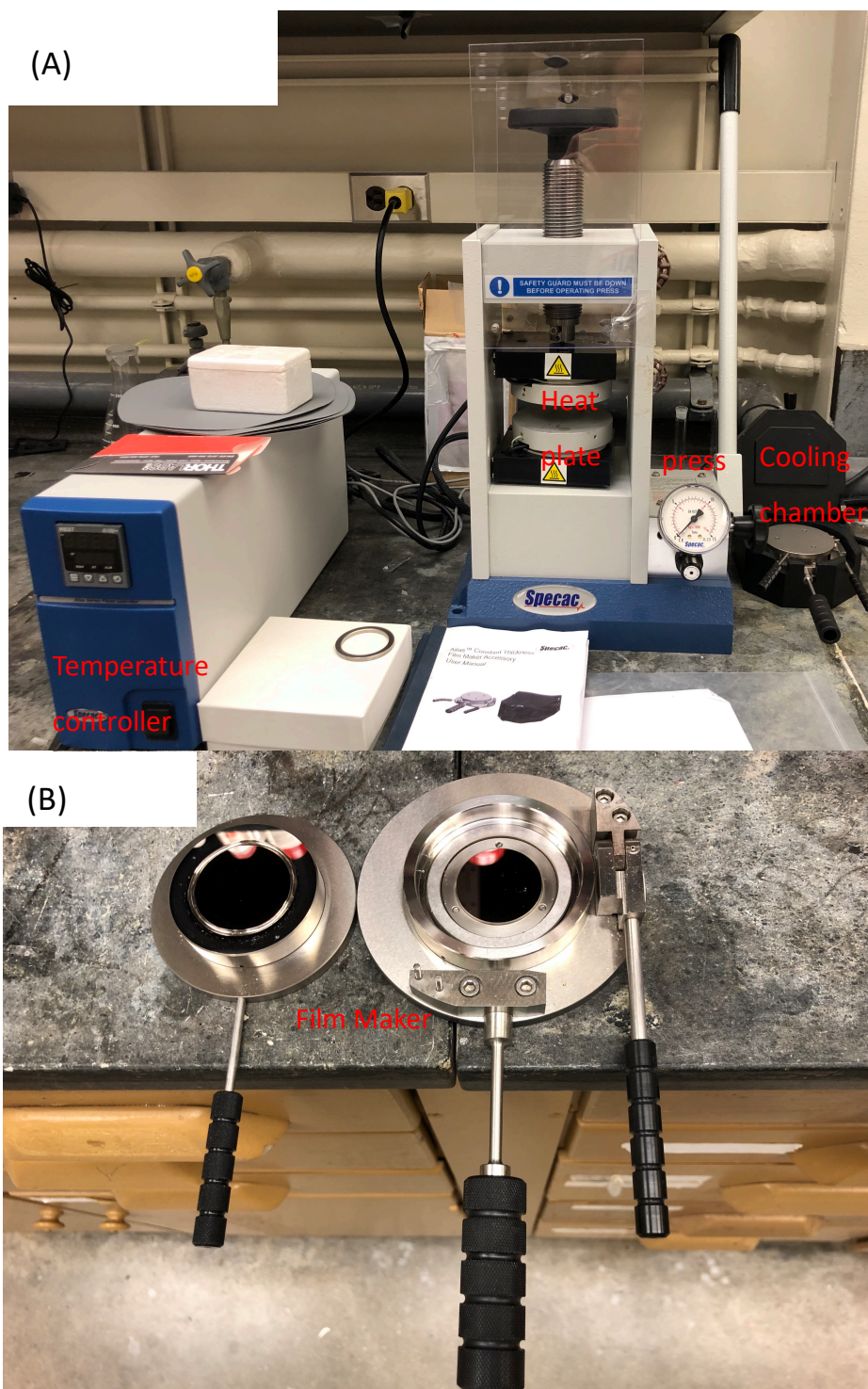


Figure 6-1 Sample preparation device
(A) A press, two heated platen, a temperature controller, and a cooling chamber; (B) Film maker.

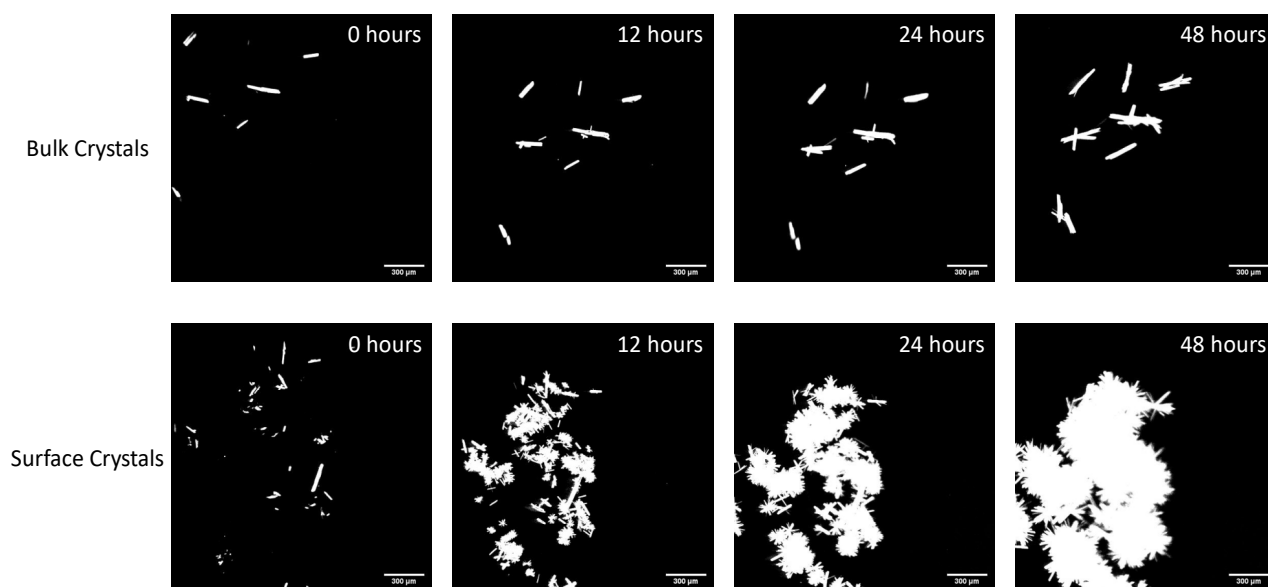


Figure 6-2 Time-dependent SHG images of seeded crystals in bulk and on surface of ASD films

VITA

Zhengtian Song is the daughter of Lifeng Song and Kaiwen Lu. She was born in Maanshan, Anhui, China in 1993. She got Bachelor of Science degree in Peking University in China in 2014, majoring in chemistry. Then she joined Professor Garth Simpson research group in Purdue University. Her research interests include instrumentation of nonlinear optical microscope, analytical method development for pharmaceutical materials, and working with synchrotron X-ray diffraction at Argonne national lab.

PUBLICATION

analytical
chemistryCite This: *Anal. Chem.* 2018, 90, 4406–4413

Article

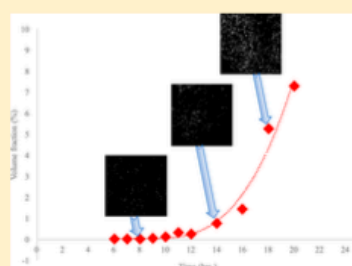
pubs.acs.org/ac

Kinetic Modeling of Accelerated Stability Testing Enabled by Second Harmonic Generation Microscopy

Zhengtian Song,^{†,‡,||} Sreya Sarkar,^{†,‡,||} Andrew D. Vogt,[‡] Gerald D. Danzer,[‡] Casey J. Smith,[†] Ellen J. Gualtieri,[§] and Garth J. Simpson^{*,†,||}[†]Department of Chemistry, Purdue University, 560 Oval Drive, West Lafayette, Indiana 47906, United States[‡]AbbVie Inc., 1 North Waukegan Road, North Chicago, Illinois 60064, United States[§]Formulatrix, Inc., 10 DeAngelo Drive, Bedford, Massachusetts 01730, United States

Supporting Information

ABSTRACT: The low limits of detection afforded by second harmonic generation (SHG) microscopy coupled with image analysis algorithms enabled quantitative modeling of the temperature-dependent crystallization of active pharmaceutical ingredients (APIs) within amorphous solid dispersions (ASDs). ASDs, in which an API is maintained in an amorphous state within a polymer matrix, are finding increasing use to address solubility limitations of small-molecule APIs. Extensive stability testing is typically performed for ASD characterization, the time frame for which is often dictated by the earliest detectable onset of crystal formation. Here a study of accelerated stability testing on ritonavir, a human immunodeficiency virus (HIV) protease inhibitor, has been conducted. Under the condition for accelerated stability testing at 50 °C/75%RH and 40 °C/75%RH, ritonavir crystallization kinetics from amorphous solid dispersions were monitored by SHG microscopy. SHG microscopy coupled by image analysis yielded limits of detection for ritonavir crystals as low as 10 ppm, which is about 2 orders of magnitude lower than other methods currently available for crystallinity detection in ASDs. The four decade dynamic range of SHG microscopy enabled quantitative modeling with an established (JMAK) kinetic model. From the SHG images, nucleation and crystal growth rates were independently determined.



Many emerging drug candidates exhibit low aqueous solubility, which can directly impact bioavailability and ultimately efficacy. In such cases, the bioavailability of an active pharmaceutical ingredient (API) is routinely improved by rendering the API amorphous within a polymer matrix to form an amorphous solid dispersion (ASD).^{1,2} However, ASDs are generally metastable systems; spontaneous crystallization of the API during storage at elevated relative humidity, for example, or processing can negatively impact the bioavailability of the API. The effective dose of a formulation may be lower than the intended dose. Furthermore, residual crystals present upon dissolution may serve as nuclei for recrystallization following dissolution under conditions of supersaturation.³ To mitigate these complications, extensive accelerated stability testing methods are currently performed to quantify trace crystallinity present in ASDs under stressed conditions, as stability testing under ambient conditions is prohibitively time-consuming.^{4,5}

In principle, kinetic modeling at elevated temperatures and humidity can be used to predict stability under ambient conditions, which is ultimately the defining property of interest.^{6,7} Two key kinetic processes are most directly relevant: molecular diffusion and crystal nucleation/growth. Parameterized models for nucleation and growth allow prediction of time-dependent crystallization under ambient conditions.⁸

Given the exponential dependence of the crystallinity on many of the recovered parameters, experimental uncertainties can have large impacts on the predicted behaviors. Confident determination of reliable kinetic parameters is most directly obtained through acquisition over a large range of concentrations, suggesting the need for sensitive methods capable of quantification at the early stages of crystallization. Kinetic modeling is arguably the simplest to interpret from measurements acquired in the low crystallinity regime, in which local depletion and concentration gradients are negligible. The relatively low drug loading present in many ASDs further exacerbates the challenges in acquisition of kinetic data over a large dynamic range.

The most common benchmark methods for characterizing crystallinity in situ for kinetic modeling routinely exhibit limits of detection within 1 order of magnitude of the total drug loading, greatly reducing the accessible dynamic range for quantifying crystallinity. A suite of methods is typically brought to bear to inform stability assessments of ASDs, including

Received: October 16, 2017

Accepted: March 5, 2018

Published: March 5, 2018

polarized light microscopy (PLM),⁹ differential scanning calorimetry (DSC),^{10,11} X-ray powder diffraction (XRPD),¹² and solid-state NMR spectroscopy (ssNMR).^{13,14} PLM is arguably the most common method currently used to detect crystallinity in ASDs during stability testing. However, it only provides qualitative information on optically transparent samples for Boolean assessments and routinely exhibits interferences by occlusions, contaminants, and other crystalline excipients.⁹ DSC can provide information about thermal processes such as solid–solid transition but lacks the sensitivity to allow trace detection.¹⁵ XRPD, the current gold-standard method for crystallinity, detection also suffers from a relatively high detection limit.¹⁶ Detection of crystallinity below 1% is challenging for the above analytical techniques.¹⁵ Solid-state NMR has been used to quantitatively determine all components in ASDs¹³ with detection limits as low as 0.4% for carbon.¹⁴ However, ssNMR is costly and requires a relatively long sample analysis times.

Nonlinear optical imaging has recently emerged as a successful method in the pharmaceutical field for the sensitive detection of trace crystallization in amorphous systems.^{17–19} Second harmonic generation (SHG), in particular, is a scattering process, in which the incoming light is converted to light of twice the frequency.²⁰ The particular symmetry properties of SHG only permit this second-order process in noncentrosymmetric systems such as chiral crystals, whereas amorphous systems do not generate a coherent SHG signal and negligible background.^{21–23} SHG microscopy has been demonstrated as a powerful method for the detection of noncentrosymmetric crystals with low detection limits, which shows high potential for accelerated stability testing of ASDs.¹⁷

Ritonavir is an active ingredient in many successful anti-HIV formulations with extensively studied crystallization kinetics.^{24,25} Given the rich phase behavior of ritonavir, a substantial body of literature has accumulated for modeling crystallization of amorphous ritonavir, both as a pure compound and as an amorphous formulation. In a recent study centered on crystallization of ritonavir and formulations containing amorphous ritonavir, Zhu et al.²⁶ performed a series of stability experiments to develop predictive models for ritonavir crystallization behaviors, as a case study. The kinetic modeling was performed based on determination of the induction time, corresponding to the minimum time required to detect onset of crystallization.

In this work, we seek to significantly expand upon the results of the preceding studies with ritonavir to interrogate the early stage ($\ll 1\%$) crystalline regime by SHG microscopy. Accelerated stability testing has been carried out on a model ritonavir-ASD to determine the detection of limit of SHG microscopy and assess the utility of the approach for informing kinetic modeling of crystal nucleation and growth. Specifically, the primary objective of the present work is the development of parametrized models for early stage crystal nucleation and growth kinetics that can be used for quantitatively assessing the anticipated stability under ambient conditions.

METHODS

Amorphous ritonavir extrudate with 15% (w/w) ritonavir (manufactured by AbbVie), copovidone (BASF), plasticizer/surfactant, and silicon dioxide was prepared by hot melt extrusion, as previously described^{27,28} and then milled to a powder. The dry glass transition temperature of the milled extrudate was 56 °C, as measured by DSC. For the studies

described herein, samples were prepared by placing powdered extrudates on the glass slides as a thin layer ($\sim 300 \mu\text{m}$) over a sample area of $\sim 1 \text{ cm}^2$. For accelerated stability testing, samples were stressed at 50 °C/75% relative humidity (RH) or 40 °C/75% RH. SHG microscopy was used to observe the crystallization of stressed amorphous ritonavir at early times (0 to 24 h). At this RH, the extrudates exhibited low turbidity, suggestive of temperatures above the glass transition temperature. High RH is known to suppress the glass transition temperature of copovidone.²⁹

SHG images were acquired by using a commercial SONICCC (second-order nonlinear optical imaging of chiral crystals) microscope (Formulatrix, Inc), modified in-house for compatibility with powder analysis. Specifically, the instrument was redesigned to allow epi-detection of SHG (details shown in the Supporting Information). The system was powered by a Fianium FemtoPower laser (1060 nm, 170 fs, 50 MHz). A resonant mirror (8 kHz) and a galvanometer mirror are used for beam scanning to generate SHG images. In this study, all of the SHG images were acquired with 350 mW excitation laser power at the sample, and each field of view was $\sim 2.0 \text{ mm} \times 2.0 \text{ mm}$. This power level is significantly higher than typically used in NLO microscopy measurements of tissue samples. However, the power density at the sample was relatively low, as all measurements were acquired with a low numerical aperture objective (NA = 0.3) over a large field of view ($>4 \text{ mm}^2$). Furthermore, the use of a fast-scan (8 kHz) resonant mirror with the beam blocked at the tuning points reduced the single-pass exposure for each pixel to $\sim 50 \text{ ns}$ (or approximately 2–3 laser pulses) per scan and then allowed for 1/30 s of thermal relaxation prior to subsequent sampling. For unstressed samples, the SHG signal was collected in the epi direction (i.e., back through the same objective used to deliver the infrared beam), as powders typically generate little signal in transmission due to optical scattering. For the ritonavir milled extrudate samples stressed at either 50 or 40 °C with 75%RH, the SHG signal was collected in transmission. Two replicates of each sample were prepared, and three different positions of each sample were observed for a total of six fields of view obtained for each time-point. ImageJ was used to analyze the SHG images based on particle counting analysis as described previously.¹⁹

THEORY

Crystal growth rates can be independently and self-consistently modeled in terms of nucleation and diffusion-limited growth. Parameterized models for nucleation and fundamental models for growth allow prediction of time-dependent crystallization. The overall crystallization kinetics under isothermal conditions can be described by JMAK (Johnson, Mehl, Avrami, and Kolmogorov) theory in terms of volume fraction of the new phase under the assumption that nucleation and growth rates are constant throughout the transformation.^{30,31} In this theory, the volume fraction of the new phase, α , is proposed by eq 1, in which t is time, t_0 is the induction time and is defined as the earliest detection of an SHG signal, I is the nucleation rate, and U is the crystal growth rate.

$$\alpha(t - t_0) = 1 - \exp\left\{-g \int_{t_0}^t I(t') \left[\int_{t'}^t U(t'') dt'' \right]^3 dt'\right\} \quad (1)$$

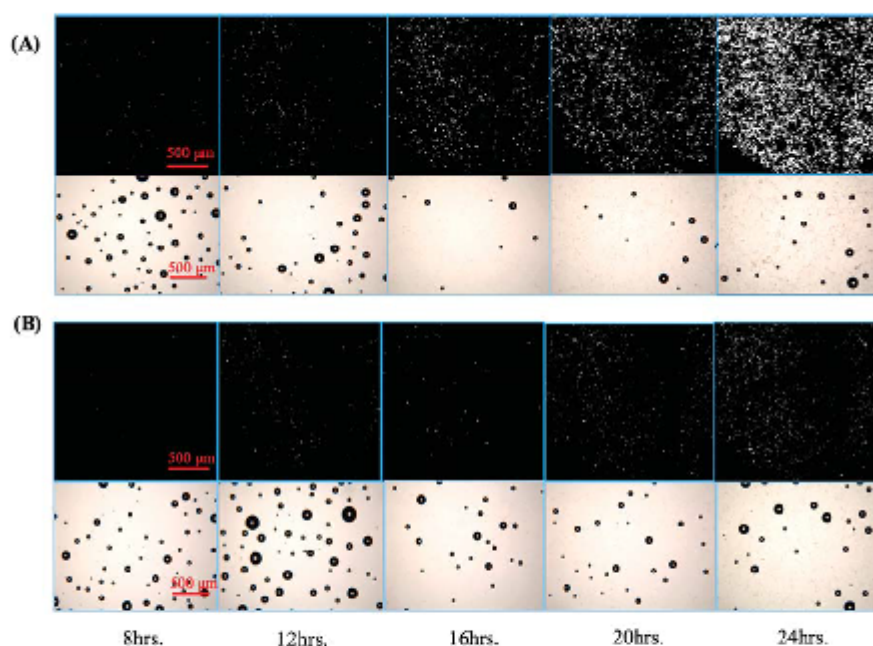


Figure 1. SHG and bright field images for time-dependent crystal growth in 15% itronavir milled extrudate stressed in (A) 50 °C/75% RH and (B) 40 °C/75% RH chambers. The spherical occlusions in the bright field images correspond to air pockets within the partially melted copovidone matrix. After ~16 h, crystals can be observed by bright field imaging with low contrast.

For spherical crystals, the shape-factor g is $4\pi/3$. For steady-state homogeneous nucleation, nucleation and growth rates are considered to be constant; therefore, eq 1 can be rewritten as eq 2.

$$\alpha(t - t_0) = 1 - \exp\left[-\frac{gIU^3(t - t_0)^4}{4}\right] \quad (2)$$

The assumption of constant nucleation and growth rates are only expected to rigorously hold at the early stages of crystallization ($\ll 1\%$), for which the concentration of amorphous API is not significantly affected by the crystalline fraction. The assumption of approximately spherical particles may initially appear to be questionable given that pristine single crystals exhibit diverse habits. For high aspect ratio needle-like crystals, this assumption will no longer be valid. However, the ritonavir particles studied in the present case exhibit aspect ratios of less than 3, which is common in many pharmaceutically desirable materials given the challenges of manufacturing associated with needle-like crystals. In this range, the error introduced by assumption of approximately spheroidal particles is insignificant relative to the Poisson uncertainty introduced by the finite number of discrete crystals sampled.

The volume fraction of the transformed material can be recovered by simplification of the more general form of the JMAK equation as shown in eq 3 by grouping constants and generalizing the exponential to an adjustable parameter.³⁰

$$\alpha(t - t_0) = 1 - \exp(-K(t - t_0)^n) \quad (3)$$

The parameter n is the Avrami coefficient and depends on both nucleation and crystal growth rates and thus from the formulas $N \propto (t - t_0)^2$ and $r \propto (t - t_0)^m$, which describe the variation in crystal number (N) and crystal size (r) with time.³⁰ The Avrami coefficient can be given by the following eq 4.

$$n = k + 3m \quad (4)$$

The preceding expressions hold at a particular temperature, but stability testing is most commonly performed at as a function of temperature in order to induce phase transformations in practical time scales. Connecting these accelerated stability test results back to room temperature behavior can be performed by considering the temperature dependence of diffusion and crystal growth. The growth rate of an individual crystal U (described by m in eq 4) can be parametrized and related back to diffusion and the Gibbs free energy of crystallization through eq 5.³⁰ In that equation, ΔG_v is the thermodynamic Gibbs free energy per unit volume of crystal, a is an average (effective) size parameter of the molecules building the crystalline phase, k_B is Boltzman's constant, and f is a dimensionless parameter describing the different growth modes. For the continuous growth mechanism, which is assumed that the interface between the growing crystal and the surrounding medium displays a sufficiently high concentration of growth sites, $f = 1$.³¹ U is the crystal growth rate, which is the slope from a plot of the mean crystal radius with time.

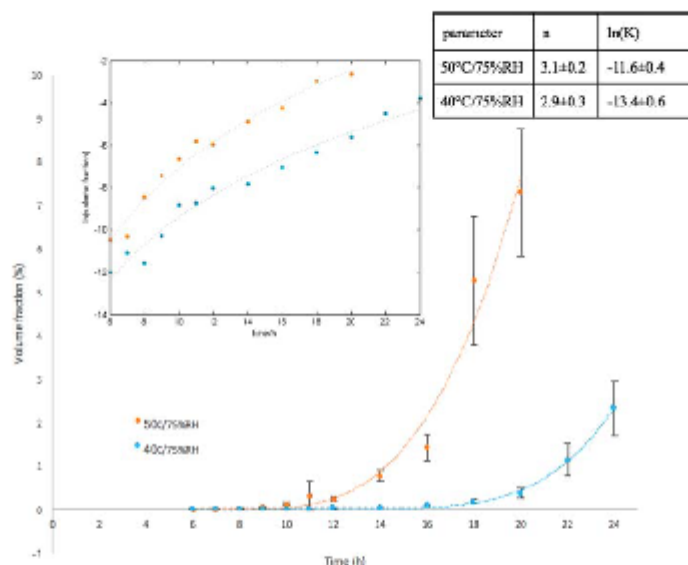


Figure 2. Percent volume fraction of crystallinity from 15% amorphous ritonavir milled extrudate at different stress conditions showing the formation and evolution of crystals with time and detection limits as low as 10 ppm (0.001%) of the total drug load.

$$U = f \frac{D}{4a} \left[1 - \exp\left(-\frac{1}{2} \frac{\Delta G_V a^3}{k_B T}\right) \right] \quad (5)$$

In practice, the expression in eq 5 can often be simplified if either diffusion limits the growth rate (in which case D dictates the overall kinetics) or if the Gibbs free energy term in the exponential represented by ΔG_V dictates the crystallization rate. Since the supersaturation decreases with increasing temperature, growth rates would be expected to decrease at elevated temperatures for crystallization under thermodynamic control. Under diffusion-limited growth conditions, the kinetics obey standard Arrhenius behaviors for diffusion $D = D_0 e^{-E_a/k_B T}$ at intermediate and lower temperatures.

The expression in eq 5 allows prediction of the growth rates at temperatures other than those measured. Extrapolation from elevated temperature behavior to ambient conditions can provide a means for evaluating potential stability of ASDs, provided that no additional phase transformations arise over temperatures not interrogated experimentally.

RESULTS AND DISCUSSIONS

Under the condition for accelerated stability testing at both 50 °C/75% RH and 40 °C/75% RH, crystal growth kinetics from the 15% w/w amorphous ritonavir milled extrudate was recorded by collecting SHG images on a scheduled basis. Ten representative SHG images and corresponding bright field images are shown in Figure 1. All of the images are shown with the same brightness scale for comparative purposes. The SHG micrographs even at the earliest stages shown in the figure yield signals well above the noise floor of the instrument (i.e., particles with >3 contiguous pixels exhibiting counts >3 counts). The time-zero samples showed no detectable SHG,

with the onset of detectable SHG at 5 h for samples stressed at 50 °C/75% RH and 40 °C/75% RH. Compared with SHG-active particles shown in Figure 1B, the number and the average size of SHG-active particles are larger as shown in Figure 1A, which form the basis of more detailed kinetic analysis (vide infra).

The 15% drug loading (DL) ritonavir milled extrudate samples contained only amorphous ritonavir and copovidone. Neither of the components is SHG-active. Ritonavir crystals are noncentrosymmetric and SHG active.^{22,32} For SHG images in Figure 1, the SHG-active areas represent ritonavir crystals. Based on the comparison of Figure 1A,B, after the same stressed time, the milled extrudate stressed at 50 °C/75% RH developed more ritonavir crystals with larger size than did the sample stressed at 40 °C/75% RH.

A particle counting approach was used to quantify crystallinity at levels from ppm regime to 10%, which corrected particle–particle overlap. In brief, the volume of each individual crystallite was estimated based on the cross-sectional area of the particle. This approach removes noise associated with variance in the SHG intensity from differences in crystal orientation. Bias introduced from particle overlap for crystallinities >1% was removed using a size-distribution dependent correction algorithm detailed elsewhere.³² Although the algorithm as described is formally derived assuming spherical particles, the aspect ratio of the ritonavir particles (~3:1) is sufficiently low to allow reliable application of the method in the present study. A minimum crystal cross-sectional area of 45 μm^2 (corresponding to three contiguous pixels) was implemented in the algorithm to ensure statistical confidence in crystal identification by image analysis. Based on the volume sampled as set by the depth of field and the field of view, this algorithm places a practical lower limit of ~0.5 ppm for detection of crystallinity.

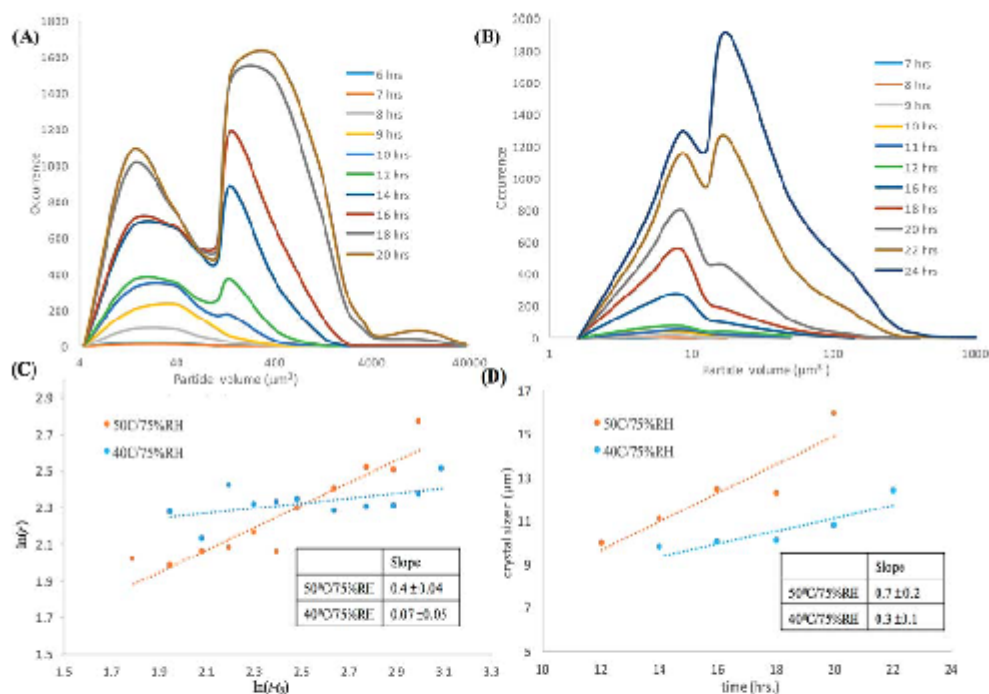


Figure 3. Crystal growth rate: Time-dependent ritonavir crystal particle size distribution at (A) 50 °C/75%RH and (B) 40 °C/75%RH; (C) crystal growth rate depicted by $\ln(r)$ vs $\ln(t - t_0)$ plot; (D) crystal growth rate for latest five time points.

This limit is substantially higher than has been reported previously based on the minimum detectable radius of 100 nm. However, Poisson statistics associated with the stochastic nature of crystallization were found to be the dominant noise source in the analysis, which were minimized by maximizing both the depth of field and field of view. Despite the high limit of detection (LoD) imposed by the particle-counting algorithm relative to previous work, SHG still produced an LoD several orders of magnitude lower than practically achievable by alternative routine benchtop methods.

Figure 2 shows the volume fraction of crystallinity from 1.5% amorphous ritonavir milled extrudate stressed at 50 °C/75% RH (orange) or 40 °C/75% RH (blue) and corresponding fits to eq 3. The crystallization rates were clearly not linear with each condition, exhibiting a significant induction time, which is tentatively attributed to the stochastic nature of nucleation coupled with the need to generate particles large enough to generate significant SHG (~ 100 nm) for detection.¹⁵ In this study, the induction time t_0 was approximately 5 h for both samples stressed at 50 °C/75% RH and 40 °C/75% RH, which was the earliest time point at which the SHG was detected with statistical confidence (i.e., with a signal greater than 3-fold higher than the standard deviation of the blank).

The limits of detection based on SHG microscopy are defined to be the concentration corresponding to a signal 3-fold higher than the standard deviation of the initially prepared samples. In Figure 2, the lower-limit for the SHG response is

also shown on a log-scale in the inset figure, consistent with the form in eq 3, calculated with the measured induction times. Both sets of fits (linear and log scaling) are shown with identical parameters in each case, given in the inset table. From the 40 °C fits, SHG microscopy exhibited a lower detection limit of 10 ppm (v/v) for crystalline ritonavir in a milled extrudate powder, which is approximately 2 to 3 orders of magnitude lower than commonly used methods (DSC, XRPD, near IR). Given the similarities in the densities of capivodone and ritonavir, the volume ratio and the mass fraction are essentially identical.

With knowledge of the induction time, additional insights into the crystallization behavior can be recovered from particle-counting analysis of the SHG images, shown in Figure 3. The top part of the figure contains the histogram of particle sizes, indicating an increase in both the number of crystals and the distribution of crystal sizes with time. To assess the crystal growth rate, the mean crystal radii were calculated by using the mean crystal size from the distribution. The time-dependent evolutions of the mean crystal radius were given by the bottom two plots. A log-log plot of mean crystal radius versus time in Figure 3C was used to extract the exponential scaling parameter m , assuming that the particle size scales as $r \propto (t - t_0)^m$. This scaling is consistent with expectations for the derivation of eq 4. An estimate of the steady-state growth rate was generated from the latest five time points under each of the two stressed conditions as shown in Figure 3D.

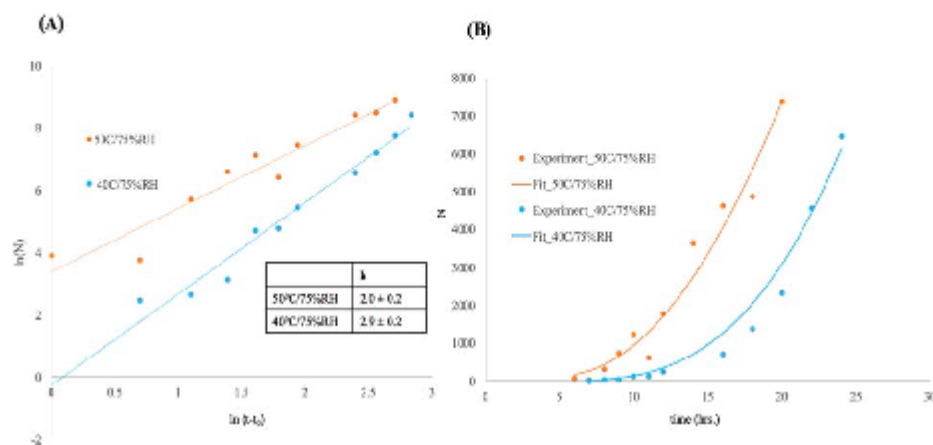


Figure 4. Kinetics of nucleation, plotted logarithmically (A) and linearly (B) to determine the exponential order parameter k in eq 4.

Particle counting approaches also allow determination of both the number of particles and the rate of new particle production (i.e., nucleation rate). The total crystalline volume fraction is a function of the combined rates of nucleation and growth through eqs 3 and 4. In Figure 4A, log–log plots of the nucleation rate recover the exponential parameter k in eq 4 from the slope, based on the relationship $N \propto (t - t_0)^k$. In contrast to the crystal growth rate, the nucleation rates (N versus t) were similar for both temperatures tested as shown in Figure 4B. It is worth noting that the nucleation rate was evaluated from data points appearing after the induction time, corresponding to the steady-state rate at which particles have both nucleated and subsequently grown to a size commensurate with reliable detection by SHG. As such, the nucleation rate is unbiased by the presence of a finite induction time.

Independent determination of the crystal nucleation and growth kinetics from particle counting of the SHG-active domains allows evaluation of the exponential parameters describing the overall crystallinity in eq 4. For crystallization reliably described by the JMAK model, the relationship $n \cong k + 3m$ is expected together with the total crystallinity scaling linearly with the average nucleation rate and cubically with the growth rate in the average particle radius. The slope results shown in Table 1 were fit via eq 4 and show good internal consistency with these expectations, suggesting general validity for use of the JMAK model.

Table 1. Parameter in JMAK Model

	k	m	k + 3m	n
50 °C/75%RH	2.0 ± 0.2	0.40 ± 0.04	3.2 ± 0.3	3.1 ± 0.2
40 °C/75%RH	2.9 ± 0.2	0.07 ± 0.05	3.1 ± 0.4	2.9 ± 0.3

While the nucleation kinetics were largely insensitive to the difference in temperature over the regime investigated as shown in Figure 4, the crystal growth kinetics in Figure 3 exhibited a steep temperature-dependence. A temperature-insensitive nucleation rate is consistent with a system in which both thermodynamics and kinetics play significant roles in driving nucleation. As the temperature is decreased, thermodynamics

suggests a higher supersaturation and a corresponding increase in nucleation rate (according to classical nucleation theory³⁰). In contrast, diffusion models suggest higher nucleation rates with increasing temperature for mass-transport limited processes. These two effects are described by ΔG_v and D in eq 5. A weak temperature dependence for nucleation, as observed for the current study, suggests that both effects are significant, such that the decrease in nucleation rates from thermodynamics as supersaturation decreases is largely offset by an increase in nucleation rates from diffusion at elevated temperature.

The increase in crystal growth rates with increased temperature is consistent with diffusion-limited kinetics over the temperatures investigated. In this case, simplification of eq 5 to the diffusion-only expression enables Arrhenius descriptions of diffusion. In order to extract the Arrhenius parameters for predicting the temperature-dependence of diffusion (and in turn, crystal growth rate), an estimate of the steady-state growth rate was generated from the latest five time points under each of the two stressed conditions explored, shown in Figure 3D. These points contained the least number of crystallites smaller than the lower limits of detection of the instrument. In this regime, the growth rates based on crystal size changes was most confidently recorded with minimal bias from nucleation. In this temperature range, the crystal growth rate was mainly dominated by diffusion. Based on the temperature-dependent crystal growth rate, the calculated activation energy of diffusion is 68.8 ± 4.3 kJ/mol, which is generally consistent with previously reported values for polymers.^{33,34}

It is worth comparing the results of the kinetic modeling of the SHG data to analogous modeling performed using conventional methods for crystallinity determination. The low limits of detection by SHG significantly reduce the induction time required to first observe the onset of detectable crystallinity for integration into kinetic modeling. In the case of API crystallization in amorphous solid dispersion, limits of detection on the order of 0.5% crystallinity are enabled by XRPD with a synchrotron source.¹⁶ From inspection of Figure 2, this limit of detection would correspond to four data points

in the 50 °C/75%RH crystallization trial and two data points in the 40 °C/75%RH trial over the same time frame of the experiment. With so few data points available, it would be challenging at best to assess the validity of any particular model for predicting crystallization kinetics by XRPD alone. In principle, longer times could be devoted to monitoring crystallization (e.g., several days or longer). However, the modeling becomes more challenging as the concentration of solubilized drug and the corresponding degree of supersaturation changes significantly at higher crystallinity. In addition, the present study was performed under conditions leading to relatively rapid crystal formation. For stability testing performed approximating ambient conditions, the timeframes required for observation of crystallinity to inform modeling by conventional benchtop methods can become prohibitive for routine optimization of formulations.

The importance of quantitative modeling for predictive behavior is particularly relevant to pharmaceutical analysis given the regulatory shifts toward QbD concepts for pharmaceutical characterization. QbD approaches rely on a quantitative understanding of key aspects of the formulation for predicting performance and bioavailability. For ASDs, stability is arguably one of the most critical factors to evaluate. The results summarized in Figure 2 demonstrate a dynamic range of detection by SHG spanning more than four decades (100 ppm to several %), the collective results of which can be integrated into a single unified kinetic model capable of predicting both the overall number and size distribution of API crystals under diverse storage conditions. In contrast, the dynamic range of many alternative benchtop methods routinely span 1 order of magnitude or less and provide little direct information on the size distribution. Consequently, the predictive capability of SHG microscopy measurements for QbD assessments is significantly improved relative to alternative established methods for samples amenable to SHG analyses. By using parametrized models, the measurements also allow prediction of anticipated trends under alternative conditions (e.g., ambient). This predictive ability can benefit long-term stability assessments for which the direct measurements are prohibitively time-consuming during formulation optimization.

While the use of SHG for analysis of amorphous solid dispersions has been demonstrated previously,¹⁵ the present study is unique in the use of image analysis for determination of not only the percent crystallinity, but recovery of the particle size distribution at each time-point. This additional information enabled independent determination of the nucleation and crystal growth rates, both of which combine to provide a complete description of crystallization kinetics in amorphous solid dispersions. Dissolution kinetics and correspondingly bioavailability is profoundly impacted by the particle size distribution, with dissolution arising more rapidly from a large number of small crystals as opposed to a small number of large crystals.²⁵

The SHG image analysis approach demonstrated in this work also has distinct practical advantages over established methods such as PLM. PLM can exhibit limits of detection well below 1% under favorable conditions. However, the image contrast for crystals is reduced by the presence of false-positive contributions from surface/edge effects in the sample, occlusions, scattering, etc. (representative SHG and PLM images are provided in Figure S1, in the Supporting Information). The high background and false-positives within the PLM images effectively render most automated particle counting image

analysis approaches inapplicable, such that images are often interpreted manually. In contrast, SHG exhibits little detectable background from occlusions and the polymer matrix, such that the resulting images are directly compatible with well-established and relatively simple automated image analysis algorithms. Compatibility with automated operation is clearly an attractive property for widespread adoption within the pharmaceutical community.

The particle counting approach described herein has the distinct advantage of being applicable irrespective of the crystal form of the SHG-active moiety or the need for calibration with a pure substance. Crystallinity is assessed entirely based on the calculated volume from individual particles. This capability is particularly advantageous in studies of pharmaceutical materials, as APIs often exhibit rich phase behavior with several crystal forms and/or polymorphs potentially accessible for crystal formation. Ritonavir is a particularly well-studied example of crystal polymorphism, in which the Form II polymorph exhibits significantly lower bioavailability in oral formulations relative to the metastable Form I. Confocal Raman and near-infrared spectra acquired from later stages in the crystallization were consistent with the more stable Form II produced in the present study, which are shown in Figure S2. Such combined measurements highlight the advantages of coupling quantitative analysis approaches such as SHG with qualitatively rich spectroscopic characterization methods.

While the focus of the present study is centered on characterization of extruded feedstock materials, it is worthwhile to consider the challenges associated with accelerated stability assessments in final dosage forms. For oral dosage forms comprised of compressed powders, additional crystalline excipients may be present in addition to the ASDs. Several strategies have been pursued for enabling quantitative analysis by SHG in these more complex matrices. UV-SHG has been shown to exhibit enhanced selectivity for aromatic APIs, enabling selective detection of crystalline API in the presence of crystalline sugars (e.g., lactose and mannitol).¹⁸ In addition, SHG-active particles can be targeted for subsequent Raman microscopy measurements for definitive determination of composition on a per-particle basis.²¹ Alternatively, synchrotron XRD can inform structural composition of individual microscopic particles identified for analysis by SHG.²² These strategies are generally compatible with the kinetic modeling approach described herein, although with the caveat that the lower limits of detection and temporal resolution may be compromised in complex multicomponent mixtures containing additional SHG-active excipients. Final dosage forms with amorphous excipients can generally be expected to be directly compatible with SHG analysis for quantification of crystallinity.¹⁹

CONCLUSION

In this study, SHG microscopy was used to develop analytical models for predicting the crystallization behavior of ritonavir in a model ASD formulation. The low (10 ppm v/v) limit of detection of SHG microscopy extended the range of data to incorporate into the model by ~2 orders of magnitude lower compared to other routine benchtop methods (e.g., DSC, XRPD) for ritonavir crystallinity detection in ASDs. Most significantly, SHG extends the measurement into the low crystallinity regime, in which the analytical modeling is simplified by the assumption of a constant average concentration in the polymer. Image analysis of the SHG micrographs

allowed separate evaluation of contributions from both nucleation and growth in dictating the overall net kinetics of crystallization. The values of crystallinity were demonstrated to be consistent with the JMAK kinetic model. This information allows prediction of both the anticipated crystalline fraction as well as the crystalline number density and size distribution. The temperature-dependent changes in the SHG microscopy images allowed for determination of a diffusional activation energy, which in turn allowed for modeling to predict the anticipated kinetics under unique experimental conditions. Since these results build off measurements acquired primarily for crystalline fractions much lower than 0.5%, the overall time frame for optimization of a particular ASD formulation has the potential to be substantially reduced through integration of SHG imaging. Consequently, full kinetic modeling with predictive capability can be performed with a collective set of measurements obtained at crystallinities below those typically required for simple pass/fail Boolean assessments in formulation optimization. Finally, mathematical understanding of the kinetics of crystallization facilitates quality by design (QbD) approaches in the development of formulations.

■ ASSOCIATED CONTENT

Supporting Information

The Supporting Information is available free of charge on the ACS Publications website at DOI: 10.1021/acs.analchem.7b04260.

Modification of instruments, the comparison of PLM and SHG for crystallinity detection, and the identification of ritonavir crystal form. (PDF)

■ AUTHOR INFORMATION

Corresponding Author

*E-mail: gjsimpson@purdue.edu.

ORCID

Sreya Sarkar: 0000-0002-1614-3730

Garth J. Simpson: 0000-0002-3932-848X

Author Contributions

[†]Z.S. and S.S. contributed equally to this work.

Notes

The authors declare no competing financial interest.

■ ACKNOWLEDGMENTS

The authors gratefully acknowledge funding for the present work from the National Science Foundation through an NSF-GOALI award (No. CHE-1643745). In addition, Z.S. and S.S. acknowledge financial support for this work from AbbVie. The authors would also like to acknowledge Jayanth Doddi for assistance in sample preparation and Geoff G. Zhang for helpful feedback on the kinetic modeling. We would also like to acknowledge Formulatrix for the use of SONICC instrumentation.

■ REFERENCES

- Serajuddin, A. T. M. *J. Pharm. Sci.* **1999**, *88* (10), 1058–1066.
- Kennedy, M.; Hu, J.; Gao, P.; Li, L.; Ali-Reynolds, A.; Chal, B.; Gupta, V.; Ma, C.; Mahajan, N.; Akrami, A.; Surapaneni, S. *Med. Pharmaceutics* **2008**, *5* (6), 981–993.
- Gao, Y. S.; Shalae, E.; Smith, S. *TrAC, Trends Anal. Chem.* **2013**, *49*, 137–144.
- Kommanaboyina, B.; Rhodes, C. T. *Drug Dev. Ind. Pharm.* **1999**, *25* (7), 857–868.

- Waterman, K. C.; Adami, R. C. *Int. J. Pharm.* **2005**, *293* (1–2), 101–125.
- Yang, J.; Grey, K.; Doney, J. *Int. J. Pharm.* **2010**, *384* (1–2), 24–31.
- Sindait, W.; Leane, M.; Clarke, G.; Dennis, A.; Tobyn, M.; Timmins, P. *J. Pharm. Sci.* **2011**, *100* (11), 4687–4699.
- Schmëtzler, J. W. P.; Boltachev, G. S.; Baidakov, V. G. *J. Chem. Phys.* **2006**, *124* (19), 194503.
- Carlton, R. A. *Polarized Light Microscopy. In Pharmaceutical Microscopy*; Springer: New York, 2011; pp 7–64.
- Yoshitani, Y.; Iijima, H.; Yonemochi, E.; Tenda, K. *J. Therm. Anal. Calorim.* **2006**, *85* (3), 689–692.
- Baird, J. A.; Taylor, L. S. *Adv. Drug Delivery Rev.* **2012**, *64* (5), 396–421.
- Ghebremeskel, A. N.; Vemavarapu, C.; Lodaya, M. *Pharm. Res.* **2006**, *23* (8), 1928–1936.
- Berendt, R. T.; Speger, D. M.; Ibbester, P. K.; Munson, E. J. *TrAC, Trends Anal. Chem.* **2006**, *25* (10), 977–984.
- Labach, J. W.; Padden, B. E.; Winslow, S. L.; Salisbury, J. S.; Masters, D. B.; Topp, E. M.; Munson, E. J. *Anal. Bioanal. Chem.* **2004**, *378* (6), 1504–1510.
- Wanapun, D.; Kestur, U. S.; Kissick, D. J.; Simpson, G. J.; Taylor, L. S. *Anal. Chem.* **2010**, *82* (13), 5425–5432.
- Thakral, S.; Terban, M. W.; Thakral, N. K.; Suryanarayanan, R. *Adv. Drug Delivery Rev.* **2016**, *100*, 183–193.
- Kissick, D. J.; Wanapun, D.; Simpson, G. J. *Annu. Rev. Anal. Chem.* **2011**, *4*, 419–437.
- Toth, S. J.; Madden, J. T.; Taylor, L. S.; Marsac, P.; Simpson, G. J. *Anal. Chem.* **2012**, *84* (14), 5869–5875.
- Schmitt, P. D.; Trasi, N. S.; Taylor, L. S.; Simpson, G. J. *Mol. Pharmaceutics* **2015**, *12* (7), 2378–2383.
- Chowdhury, A. U.; Zhang, S. J.; Simpson, G. J. *Anal. Chem.* **2016**, *88* (7), 3853–3863.
- Chowdhury, A. U.; Ye, D. H.; Song, Z. T.; Zhang, S. J.; Hedderich, H. G.; Mallick, B.; Thinnahari, S.; Ramakrishnan, S.; Sengupta, A.; Gualtieri, E. J.; Bouman, C. A.; Simpson, G. J. *Anal. Chem.* **2017**, *89* (11), 5958–5965.
- Toth, S. J.; Schmitt, P. D.; Snyder, G. R.; Trasi, N. S.; Sullivan, S. Z.; George, I. A.; Taylor, L. S.; Simpson, G. J. *Cryst. Growth Des.* **2015**, *15* (2), 581–586.
- Schmitt, P. D.; DeWalt, E. L.; Dow, X. Y.; Simpson, G. J. *Anal. Chem.* **2016**, *88* (11), 5760–5768.
- Danner, S. A.; Carr, A.; Leonard, J. M.; Lehman, L. M.; Gudiol, F.; Gonzalez, J.; Raventos, A.; Rubio, R.; Bouza, E.; Pintado, V.; Aguado, A. G.; Delomas, J. G.; Delgado, R.; Borleffi, J. C. C.; Hsu, A.; Valdes, J. M.; Boucher, C. A. B.; Cooper, D. A.; Gimeno, C.; Clotet, B.; Tor, J.; Ferrer, E.; Martinez, P. L.; Moreno, S.; Zanacada, G.; Alcamí, J.; Nostega, A. R.; Pulido, F.; Glassman, H. N. *N. Engl. J. Med.* **1995**, *333* (23), 1528–1533.
- Bauer, J.; Spanton, S.; Henry, R.; Quick, J.; Driki, W.; Porter, W.; Morris, J. *Pharm. Res.* **2001**, *18* (6), 859–866.
- Zhu, D. H.; Zograff, G.; Gao, P.; Gong, Y. C.; Zhang, G. G. Z. *J. Pharm. Sci.* **2016**, *105* (9), 2932–2939.
- Breitenbach, J. *Eur. J. Pharm. Biopharm.* **2002**, *54* (2), 107–117.
- Tho, I.; Leopold, B.; Rosenberg, J.; Maerlein, M.; Bandl, M.; Fäcker, G. *Eur. J. Pharm. Sci.* **2010**, *40* (1), 25–32.
- Oksanen, C. A.; Zograff, G. *Pharm. Res.* **1990**, *7* (6), 654–657.
- Schmëtzler, J. W. *Nucleation theory and applications*; Wiley-VCH: Weinheim, Germany, 2005.
- Gutzow, I.; Schmëtzler, J. *The vitreous state: thermodynamics, structure, rheology and crystallization*; Springer: Berlin, 1995.
- Newman, J. A.; Schmitt, P. D.; Toth, S. J.; Deng, F. Y.; Zhang, S. J.; Simpson, G. J. *Anal. Chem.* **2015**, *87* (21), 10950–10955.
- Schmitt, E. A.; Law, D.; Zhang, G. G. Z. *J. Pharm. Sci.* **1999**, *88* (3), 291–296.
- Vrentas, J. S.; Vrentas, C. M. *J. Polym. Sci., Part B: Polym. Phys.* **2003**, *41* (8), 785–788.
- Amidon, G. L.; Lennevas, H.; Shah, V. P.; Crison, J. R. *Pharm. Res.* **1995**, *12* (3), 413–420.